VNIVERSITAT DE VALÈNCIA

PROGRAMA DE DOCTORAT EN FÍSICA

TESIS DOCTORAL

Estudio unificado del espectro y propiedades de mesones pesados para energías por debajo y por encima de umbrales mesón-mesón

Roberto Bruschini

Director:
Prof. PEDRO GONZÁLEZ MARHUENDA

Junio 2022

VNIVERSITAT DE VALÈNCIA

PROGRAMA DE DOCTORAT EN FÍSICA

PH.D. THESIS

Unified Study of Spectrum and Properties of Heavy Mesons at Energies below and above Meson-Meson Thresholds

Roberto Bruschini

supervised by
Prof. PEDRO GONZÁLEZ MARHUENDA

June 2022

Unified Study of Spectrum and Properties of Heavy Mesons at Energies below and above Meson-Meson Thresholds

Roberto Bruschini

A mia figlia Beatrice.

Contents

List of Figures

List of Tables

Ringraziamenti

Voglio innanzitutto ringraziare Pedro per il suo appoggio e la sua guida costante. Più che un relatore, un amico e un mentore nel lavoro e nella vita. Grazie anche a Lilly per l'indimenticabile calore e gentilezza nei confronti miei e di mia moglie fin dal nostro primo arrivo. Un ringraziamento sentito va anche al Colegio Mayor San Juan de Ribera: Santiago, Amparo, Pilar, Oleg e tutti i brillanti studenti e studentesse che ho avuto la fortuna di conoscere. Mi avete fatto sentire sempre a casa in tutti questi anni. Voglio ringraziare anche Eric per avermi ospitato alla Ohio State University e avermi insegnato così tanto nel poco tempo in cui sono rimasto. A mia moglie, alla mia famiglia e ai miei amici dico solo che la mia vita non sarebbe vita senza di voi.

Introduction

Asymptotic freedom and color confinement are undoubtedly the most remarkable aspects of quantum chromodynamics (QCD) . Indeed, it is because of these features that QCD is universally accepted as the quantum field theory of strong interactions [1–3]. On the one hand, asymptotic freedom, meaning that the theory approaches a noninteracting one in the high energy limit, allows for a perturbative treatment, so that the QCD Lagrangian can be used to derive analytical expressions describing high-energy processes. On the other hand, color confinement, implying that all observable states are color-neutral, is a purely nonperturbative phenomenon, which prevents an analytical calculation of the low-energy interactions such as the ones binding quarks into hadrons. Hence, a description of the hadron spectrum from QCD has been pursued by means of various approximate nonperturbative techniques. In particular, the study of heavy mesons provides an ideal benchmark for such techniques, since the high mass of the heavy quarks (i.e., bottom, charm) allows to simplify their treatment [4].

Lattice QCD is probably the best founded method to investigate nonperturbative QCD. In this approach, nonperturbative QCD is simulated by discretizing its continuum action (including quark and gluon fields) in a gauge invariant way [5–12]. Approximations, e.g., no sea quarks, unphysically heavy pions, have been necessary in practical calculations for many years. Nowadays, the technical advances and steadfast increase of computing power in the last few years have allowed to gradually remove some of them [13–25].

Alternatively, effective field theory (EFT) is a widely popular tool for the systematic modeling of QCD at low energies [26]. For instance, some nonrelativistic QCD EFTs [27–36] treat bound states in terms of heavy quarks, while others [37–42] use hadron degrees of freedom instead. Although the systematic improvement of EFT calculations often involves increasing the number of parameters, predictive power can be maintained as long as there is enough abundance of data and lattice QCD calculations to fix their value.

QCD sum rules [43] have also been used to perform nonperturbative calculations of the hadron spectrum and properties (see, for example, the

reviews [44, 45] and references therein). This method uses identities between correlation functions to connect measurable quantities, such as hadron masses, widths, and form factors, with the fundamental ones of QCD, such as the strong coupling constant and the quark masses. Though it must be noted that, while sum rules are in principle exact, several approximations and truncations are usually needed in order to derive practical results.

The quark binding interaction may also be studied using the Bethe-Salpeter (BS) equation [46]. The BS approach to the bound state problem has the virtue of being formally exact and completely relativistic, but its solution presents formidable difficulties (see [47], for example). As an alternative, one may let himself be guided by the incredible success of potential quark models [48, 49] to try to reduce the BS formulation to a more transparent one. This reduction can be done systematically under the static approximation and the nonrelativistic limit [50]. These two conditions, which may be met by states of a heavy quark-antiquark pair, allow to reduce the BS equation to a Schrödinger equation for the equal-time wave function. The quark binding interaction is then described by an effective potential, which can be determined in a gauge invariant way through the Wilson loop formalism [51, 52]. Concretely, this potential has been calculated *ab initio* in lattice QCD using the Born-Oppenheimer (BO) approximation for heavy-quark mesons [53, 54]. In this approximation, based on the mass of the heavy quarks being much larger than the QCD intrinsic energy scale, the quark-antiquark potential is calculated from the energy levels of stationary gluon and light quark fields in presence of static color sources (the heavy quarks).

Historically, the BO potentials have been first calculated in quenched lattice QCD, this is, neglecting light (sea) quarks. The resulting ground state potential has a Cornell-like (funnel) form, and is therefore associated to the familiar quarkonium system studied in quark models [22]. Excited state potentials are instead associated with quarkonium hybrid configurations [53, 54]. These potentials can be used to obtain a physical picture of conventional quarkonium and quarkonium hybrid mesons, whose investigation is the purpose of Part I of this thesis [55–58]. Calculations of the static energy levels in unquenched lattice QCD, this is, including light quarks, on the other hand, are fairly more recent [15, 17]. The observation of string breaking in such calculations provides the foundation for the study presented in Part II of this thesis [59–62]. These contents are organized as follows:

- In Chapter 1, we illustrate the quenched lattice QCD potentials and detail the spectrum of conventional quarkonium and quarkonium hybrid states.

- In Chapter 2, we study electromagnetic (EM) transitions between

quarkonium states in tree-level quantum electrodynamics (QED).

- In Chapter 3, we implement quark pair creation (QPC) models in an "extended" BO framework, for investigating the strong decays of quarkonium and quarkonium hybrid states to an open-flavor meson-meson pair.

- In Chapter 4, we examine string breaking in the unquenched lattice QCD potentials and discuss the difficulties it poses to the usual BO formulation. To avoid these difficulties, we adapt the diabatic framework, first introduced in molecular physics, to the study of heavy-quark mesons in terms of quark-antiquark and open-flavor meson-meson components.

- In Chapter 5, we calculate a spectrum of quark-antiquark/meson-meson bound states using the diabatic framework. We also calculate mass corrections and strong decay widths to open-flavor meson-meson pairs due to the coupling of the bound states with the open thresholds.

- In Chapter 6, we complete the development of the diabatic framework by solving the coupled-channel meson-meson scattering problem. This allows us to overcome the intrinsic limitations of the bound-state analysis, and thus obtain a completely unified description of heavy-quark mesons below and above meson-meson thresholds.

Part I

The Born-Oppenheimer Approximation

Chapter 1

Spectroscopy from Quenched Lattice QCD

In the last decades, the BO approximation, first developed in 1927 for the description of atomic molecules [63], has become a valuable tool for the study of heavy-quark systems from quenched lattice QCD [53, 54, 64]. In this chapter, we review the main steps in its construction and the resulting description of quarkonium and quarkonium hybrid mesons from quenched lattice QCD potentials. Specifically, Section 1.1 introduces the BO approximation, Section 1.2 discusses the quenched lattice QCD potentials and the corresponding spectrum, and Section 1.3 gives a brief overview of spin-dependent corrections.

1.1 BO Approximation for Heavy-Quark Systems

The fundamental assumption of the BO approximation is that the components of a physical system may be classified distinctively as "heavy" and "light" on the basis of some energy scale, and that the dynamics of the light fields can be solved by neglecting the motion of the heavy degrees of freedom. The physical idea behind this approximation is that the time-scale for the evolution of the light fields is so short that, in comparison, the heavy degrees of freedom can be treated as being still. Then, once the light fields have been integrated in this *static limit*, the motion of the heavy degrees of freedom is determined from a nonrelativistic Schrödinger equation with effective potentials enclosing all the information on the light field dynamics.

In atomic molecules, where the nuclei weigh several thousands times more than the electrons, the nuclei are treated as heavy degrees of freedom, while electrons and photons constitute the light fields. In heavy-quark systems, the

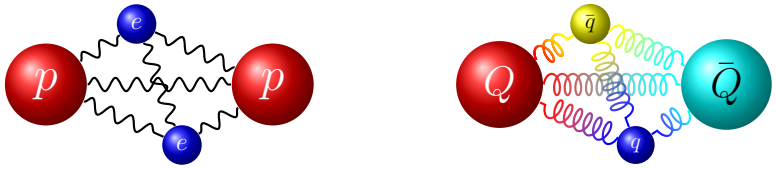

Figure 1.1: Pictorial representation of an atomic molecule (left) and a heavy-quark meson (right) as systems of heavy and light degrees of freedom. The black snakes and the colored coils represent the exchange of photons and gluons, respectively.

distinction between "heavy" and "light" is provided by the QCD energy scale Λ_{QCD}, which is the energy scale associated to the gluon field. So, heavy quark flavors, charm (c) and bottom (b), whose mass m_Q is much bigger than Λ_{QCD}, can be considered as heavy degrees of freedom. On the other hand, gluons (g) and light quark flavors, up (u), down (d), and strange (s), can be treated as light fields. This situation is pictured in Figure 1.1.

Let us now consider a heavy-quark meson composed of a heavy quark-antiquark ($Q\bar{Q}$) pair in presence of light quark and gluon fields. Following the treatment outlined in Reference [65] for atomic molecules, a heavy-quark meson state $|\psi\rangle$ in the BO approximation is the solution of

$$H\,|\psi\rangle = E\,|\psi\rangle\,, \tag{1.1}$$

where E is the energy of the state. The Hamiltonian H is separated as

$$H = K_{Q\bar{Q}} + H_{\mathrm{light}}^{(Q\bar{Q})}$$

with $K_{Q\bar{Q}}$ the kinetic energy of the heavy quarks and $H_{\mathrm{light}}^{(Q\bar{Q})}$ the residual Hamiltonian, which contains the dynamics of the light fields and their interaction with $Q\bar{Q}$. In the $Q\bar{Q}$ center-of-mass reference frame, E coincides with the mass M of the meson state, and the $Q\bar{Q}$ pair can be described by either their relative position $\boldsymbol{r}$ or relative momentum $\boldsymbol{p}$, given respectively by

$$\boldsymbol{r} = \boldsymbol{r}_Q - \boldsymbol{r}_{\bar{Q}}, \quad \text{and} \quad \boldsymbol{p} = \frac{\boldsymbol{p}_Q - \boldsymbol{p}_{\bar{Q}}}{2}.$$

Then the $Q\bar{Q}$ kinetic energy operator becomes

$$K_{Q\bar{Q}} = \frac{p^2}{2\mu},$$

with p^2 the square relative momentum operator and $\mu = m_Q/2$ the $Q\bar{Q}$ reduced mass. As for the residual Hamiltonian, it is assumed that it depends on the $Q\bar{Q}$ relative position $\boldsymbol{r}$ but not on $\boldsymbol{p}$.

In the static limit, which corresponds to neglecting the $Q\bar{Q}$ kinetic energy, $\boldsymbol{r}$ ceases being a dynamical variable. Instead, it becomes a constant parameter for the residual Hamiltonian. Following this correspondence, we relabel $H_{\rm light}^{(Q\bar{Q})}$ as $H_{\rm light}^{\rm static}(\boldsymbol{r})$, as to make clear that it corresponds to a Hamiltonian for the light fields in presence of static $Q\bar{Q}$ placed at relative position $\boldsymbol{r}$. In this limit, the light-field dynamics is completely determined from the solution of the secular equation

$$H_{\rm light}^{\rm static}(\boldsymbol{r})\,|\zeta_i(\boldsymbol{r})\rangle = V_i(\boldsymbol{r})\,|\zeta_i(\boldsymbol{r})\rangle$$

with i labeling the ground ($i=0$) and excited ($i=1,2,\dots$) states, respectively. Notice that eigenvectors $|\zeta_i(\boldsymbol{r})\rangle$, corresponding to the stationary light-field states, form a complete orthonormal set for the Hilbert space of light-field configurations for any value of $\boldsymbol{r}$,

$$\langle\zeta_i(\boldsymbol{r})|\zeta_j(\boldsymbol{r})\rangle = \delta_{ij}, \qquad \sum_i |\zeta_i(\boldsymbol{r})\rangle\,\langle\zeta_i(\boldsymbol{r})| = I_{\rm light} \tag{1.2}$$

where $I_{\rm light}$ is the identity operator acting on the light fields. Notice also that the eigenvalues $V_i(\boldsymbol{r})$, corresponding to the static energy levels of the light fields, can be determined *ab initio* in lattice QCD [53].

The $Q\bar{Q}$ motion, neglected in the static limit, can be determined by reintroducing the kinetic energy operator and expanding the heavy-quark meson state $|\psi\rangle$ on a basis of light field states. A possible way to do this is to use the so-called *adiabatic expansion*

$$|\psi\rangle = \sum_j \int \mathrm{d}\boldsymbol{r}'\psi_j(\boldsymbol{r}')\,|\boldsymbol{r}'\rangle\,|\zeta_j(\boldsymbol{r}')\rangle \tag{1.3}$$

where $|\boldsymbol{r}'\rangle$ is the (improper) eigenstate of the $Q\bar{Q}$ position with eigenvalue $\boldsymbol{r}'$. Notice that we have omitted spin degrees of freedom, both in the heavy quarks and in the light-field states, for simplicity. In BO with quenched potentials, neglecting the heavy-quark spin is justified by heavy-quark spin symmetry. As for the treatment of spin-orbit quantum numbers for the light fields, see, for example, [54] and references therein. For the sake of completeness, a brief review of the BO quantum numbers is provided in Appendix A.

Notice that the light-field basis for the adiabatic expansion, $\{|\zeta_j(\boldsymbol{r}')\rangle\}_j$, is calculated at the same position of the heavy quarks, $\boldsymbol{r}'$. This makes it the most obvious expansion in the adiabatic approximation, i.e., the idealized situation (corresponding to the limit $m_Q\to\infty$) where the light fields adjust instantaneously to the $Q\bar{Q}$ motion, hence the name. However, *the adiabatic expansion is not equivalent to an adiabatic approximation.* To see this clearly,

let us plug the adiabatic expansion (1.3) into Equation (1.1) and multiply it on the left by $\langle\zeta_i(\boldsymbol{r})|\,\langle\boldsymbol{r}|$, which gives

$$-\frac{1}{2\mu}\sum_j \langle\zeta_i(\boldsymbol{r})|\nabla^2\psi_j(\boldsymbol{r})|\zeta_j(\boldsymbol{r})\rangle + (V_i(\boldsymbol{r})-E)\psi_i(\boldsymbol{r}) = 0. \tag{1.4}$$

Now, the Laplacian ∇^2 is taken with respect to the $Q\bar{Q}$ relative position, and therefore it acts also on the light field states $|\zeta_j(\boldsymbol{r})\rangle$, as they depend on $\boldsymbol{r}$. Therefore we have

$$\langle\zeta_i(\boldsymbol{r})|\nabla^2\psi_j(\boldsymbol{r})|\zeta_j(\boldsymbol{r})\rangle = \delta_{ij}\nabla^2\psi_j(\boldsymbol{r}) + 2\boldsymbol{\tau}_{ij}(\boldsymbol{r})\cdot\boldsymbol{\nabla}\psi_j(\boldsymbol{r}) + \tau^{(2)}_{ij}(\boldsymbol{r})\psi_j(\boldsymbol{r}) \tag{1.5}$$

where the dot stands for scalar product between three-vectors, and we have introduced the so-called first and second order *non-adiabatic coupling terms (NACTs)*

$$\boldsymbol{\tau}_{ij}(\boldsymbol{r}) = \langle\zeta_i(\boldsymbol{r})|\boldsymbol{\nabla}\zeta_j(\boldsymbol{r})\rangle \quad \text{and} \quad \tau^{(2)}_{ij}(\boldsymbol{r}) = \langle\zeta_i(\boldsymbol{r})|\nabla^2\zeta_j(\boldsymbol{r})\rangle\,,$$

respectively. As one can see from their definition, the NACTs incorporate the nontrivial interaction between the light-field states and the $Q\bar{Q}$ motion, which in general mixes different light-field states with each other. Thus, albeit the possibly confusing nomenclature, the adiabatic expansion may as well contain nonadiabatic effects.

Equation (1.5) can be simplified as follows. First, using orthogonality of the light-field states (1.2), it is easy to show that the NACTs form an anti-Hermitian matrix,

$$\boldsymbol{\tau}_{ij}(\boldsymbol{r}) = \langle\zeta_i(\boldsymbol{r})|\boldsymbol{\nabla}\zeta_j(\boldsymbol{r})\rangle = \boldsymbol{\nabla}\,\langle\zeta_i(\boldsymbol{r})|\zeta_j(\boldsymbol{r})\rangle - \langle\boldsymbol{\nabla}\zeta_i(\boldsymbol{r})|\zeta_j(\boldsymbol{r})\rangle = -\boldsymbol{\tau}^*_{ji}(\boldsymbol{r}).$$

Following matrix notation, we shall use $\boldsymbol{\tau}(\boldsymbol{r})$ to indicate this matrix as a whole, and $\boldsymbol{\tau}_{ij}(\boldsymbol{r})$ to refer to its elements (the NACTs). Then, from completeness of the light-field states (1.2), we have

$$\begin{aligned}
\langle\boldsymbol{\nabla}\zeta_i(\boldsymbol{r})|\cdot|\boldsymbol{\nabla}\zeta_j(\boldsymbol{r})\rangle &= \sum_k \langle\boldsymbol{\nabla}\zeta_i(\boldsymbol{r})|\zeta_k(\boldsymbol{r})\rangle\cdot\langle\zeta_k(\boldsymbol{r})|\boldsymbol{\nabla}\zeta_j(\boldsymbol{r})\rangle \\
&= \sum_k \boldsymbol{\tau}^*_{ki}(\boldsymbol{r})\cdot\boldsymbol{\tau}_{kj}(\boldsymbol{r}) \\
&= -\sum_k \boldsymbol{\tau}_{ik}(\boldsymbol{r})\cdot\boldsymbol{\tau}_{kj}(\boldsymbol{r}) \\
&= -[\tau^2(\boldsymbol{r})]_{ij}
\end{aligned}$$

where the square $\tau^2(\boldsymbol{r}) = \boldsymbol{\tau}(\boldsymbol{r})\cdot\boldsymbol{\tau}(\boldsymbol{r})$ is intended as the combination of scalar product and matrix multiplication, and square brackets with subscripts enclosing a matrix operation indicate an element of the result. It follows that

$$[\boldsymbol{\nabla}\cdot\boldsymbol{\tau}(\boldsymbol{r})]_{ij} = \langle\zeta_i(\boldsymbol{r})|\nabla^2\zeta_j(\boldsymbol{r})\rangle + \langle\boldsymbol{\nabla}\zeta_i(\boldsymbol{r})|\cdot|\boldsymbol{\nabla}\zeta_j(\boldsymbol{r})\rangle = \tau^{(2)}_{ij}(\boldsymbol{r}) - [\tau^2(\boldsymbol{r})]_{ij},$$

so that one can rewrite Equation (1.5) as

$$\begin{aligned}\langle\zeta_i(\boldsymbol{r})|\nabla^2\psi_j(\boldsymbol{r})|\zeta_j(\boldsymbol{r})\rangle &= [I\nabla^2 + 2\boldsymbol{\tau}(\boldsymbol{r})\cdot I\boldsymbol{\nabla} + \boldsymbol{\nabla}\cdot\boldsymbol{\tau}(\boldsymbol{r}) + \tau^2(\boldsymbol{r})]_{ij}\psi_j(\boldsymbol{r}) \\ &= [(I\boldsymbol{\nabla} + \boldsymbol{\tau}(\boldsymbol{r}))^2]_{ij}\psi_j(\boldsymbol{r}) \end{aligned} \tag{1.6}$$

where we have introduced the identity matrix $I_{ij} = \delta_{ij}$, and $(I\boldsymbol{\nabla} + \boldsymbol{\tau}(\boldsymbol{r}))^2$ indicates the operator $(I\boldsymbol{\nabla} + \boldsymbol{\tau}(\boldsymbol{r}))\cdot(I\boldsymbol{\nabla} + \boldsymbol{\tau}(\boldsymbol{r}))$, intended as a scalar product and matrix multiplication in the same sense as before.

Finally, inserting (1.6) in (1.4), we see that the coefficients $\psi_j(\boldsymbol{r})$ of the adiabatic expansion obey the Schrödinger-like equation

$$\sum_j \left(-\frac{1}{2\mu}[(I\boldsymbol{\nabla} + \boldsymbol{\tau}(\boldsymbol{r}))^2]_{ij} + \delta_{ij}(V_i(\boldsymbol{r}) - E) \right)\psi_j(\boldsymbol{r}) = 0, \tag{1.7}$$

and therefore they can be interpreted as a multi-channel *adiabatic wave function* for the heavy-quark meson state. Then, from Equation (1.7) we also see that the static energy levels $V_i(\boldsymbol{r})$ play the role of effective potentials for the corresponding channel.

The NACTs, present in the kinetic energy term of Equation (1.7), couple different wave function components to each other. These couplings between channels are customarily neglected in the BO approximation for heavy-quark mesons (see, for example, [54]), which results in the *single channel approximation*. In this approximation, one assumes

$$\boldsymbol{\tau}_{ij}(\boldsymbol{r}) \approx 0 \tag{1.8}$$

and thus Equation (1.7) factorizes as

$$-\frac{1}{2\mu}\nabla^2\psi_i(\boldsymbol{r}) + (V_i(\boldsymbol{r}) - E)\psi_i(\boldsymbol{r}) = 0 \tag{1.9}$$

for $i = 0, 1, \ldots$, this is, a Schrödinger equation for each adiabatic wave function component $\psi_i(\boldsymbol{r})$ in its BO potential $V_i(\boldsymbol{r})$.

It is very important to keep in mind that the validity of the single channel approximation (1.8) should not be taken for granted just because $m_Q \gg \Lambda_{\mathrm{QCD}}$, for the NACTs may not be negligible. In that case, the single channel approximation may be deemed reasonable only as long as the wave function has no significant overlap with the NACTs. We shall come back to this crucial issue in Part II. Here in Part I, we shall focus on the ground and first excited state potentials calculated in quenched lattice QCD. More precisely, we will use these potentials and the single channel BO approximation to calculate the quarkonium meson spectrum and the lowest quarkonium hybrid state. Then we will calculate some of their EM and strong transitions with the help of QED and strong decay models, respectively.

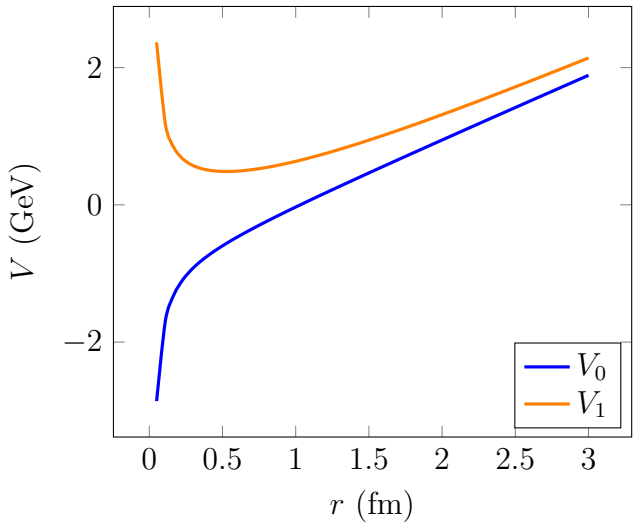

Figure 1.2: Ground and first excited potentials in quenched lattice QCD.

1.2 Quarkonia and Quarkonium Hybrids

1.2.1 The Ground State Quenched Potential

The ground state potential calculated in quenched lattice QCD [22] can be parametrized as a Cornell-like (funnel) radial potential, $V_0(\boldsymbol{r}) = V_0(r) = V_{\rm C}(r)$, with

$$V_{\rm C}(r) = \sigma r - \frac{\chi}{r} + E_0 \tag{1.10}$$

with $r = |\boldsymbol{r}|$ the $Q\bar{Q}$ distance, σ the string tension, χ the color Coulomb strength, and E_0 a constant, which in general may depend on the heavy-quark flavor. This potential, as shown in Figure 1.2, shows an attractive gluon exchange Coulomb interaction at small distances and a linear confining behavior at large distances, which is associated to the conventional quarkonium $Q\bar{Q}$ configuration extensively studied in quark models [48, 49].

In general, in presence of a radial potential, one can expand the wave function in spherical harmonics

$$\psi_i(\boldsymbol{r}) = \sum_{l=0}^{\infty} \sum_{m_l=-l}^{l} R_{i,l}(r) Y_l^{m_l}(\hat{\boldsymbol{r}})$$

with $\hat{\boldsymbol{r}} = \boldsymbol{r}/r$, $Y_l^{m_l}(\hat{\boldsymbol{r}})$ the spherical harmonics, satisfying

$$L^2 Y_l^{m_l}(\hat{\boldsymbol{r}}) = l(l+1) Y_l^{m_l}(\hat{\boldsymbol{r}})$$
$$L^z Y_l^{m_l}(\hat{\boldsymbol{r}}) = m_l Y_l^{m_l}(\hat{\boldsymbol{r}})$$

Table 1.1: Calculated spectrum of bottomonium states with $l = 0, 1, 2, 3$, and masses up to 10.9 GeV.

nL	M (MeV)
$1S$	9401.3
$1P$	9900.7
$2S$	9993.9
$1D$	10150.4
$2P$	10254.5
$3S$	10338.7
$1F$	10341.5
$2D$	10442.1
$3P$	10536.7
$2F$	10601.1
$4S$	10615.1
$3D$	10694.2
$4P$	10782.3
$3F$	10833.9
$5S$	10856.5

with $\boldsymbol{L}$ the orbital angular momentum, and $R_{i,l}(r)$ the radial wave functions. Then the Schrödinger equation (1.9) can be reduced to its radial form

$$-\frac{1}{2\mu}u''_{i,l}(r) + \left(\frac{l(l+1)}{2\mu r^2} + V_i(r) - E\right)u_{i,l}(r) = 0 \tag{1.11}$$

where $u_{i,l}(r) = rR_{i,l}(r)$ is a reduced radial wave function, and $u''_{i,l}(r)$ its second derivative. Notice that, in general, there is an independent spherical Schrödinger equation for each value of l, so that the complete spectrum is given by the union of the sets of solutions for all l. This is why it is customary to label quarkonium states with the spectroscopic nL notation, where $L = S, P, D, F, \ldots$ denotes orbitals with $l = 0, 1, 2, 3, \ldots$, respectively, and the "principal quantum number" $n = 0, 1, \ldots$ labels the ground and excited states of each orbital.

In single channel BO, the spectrum of quarkonium (charmonium $c\bar{c}$ and bottomonium $b\bar{b}$, in general $Q\bar{Q}$ with $Q \equiv b$ or c) states corresponds to the set of solutions of Equation (1.11) with $i = 0$ and the corresponding potential (1.10). To calculate it, one must specify some values for the parameters in the ground state potential. This could be done *ab initio* by fitting Equation (1.10)

to quenched lattice QCD data on the ground-state static energy level. However, as it will become clear in Part II, a good description of the lowest experimental quarkonium states states plays a pivotal role in building a unified description of quarkoniumlike mesons. For this reason, for the string tension and color Coulomb strength, we take the standard phenomenological values [66]

$$\sigma = 925.6 \text{ MeV/fm}, \tag{1.12a}$$

$$\chi = 102.6 \text{ MeV fm}. \tag{1.12b}$$

As for the flavor-dependent constant E_0, we decompose it as

$$E_0 = 2m_Q - \beta, \tag{1.12c}$$

with β a positive constant that we shall assume to be flavor-independent. The quark mass and β are then determined as follows. First, we fix the charm quark mass to its standard phenomenological value

$$m_c = 1840 \text{ MeV}, \tag{1.12d}$$

then, fitting the experimental center of gravity of the $2S$ charmonium states gives

$$\beta = 855 \text{ MeV}. \tag{1.12e}$$

Finally, using the same value of β in bottomonium, we determine the bottom quark mass by fitting any of the $1S$, $2S$, $1P$, or $2P$ experimental center of gravity of bottomonium states. Concretely, we fit the $1P$ center of gravity, which yields

$$m_b = 5215 \text{ MeV}, \tag{1.12f}$$

while we notice that choosing alternatively to fit another center of gravity would not imply any significant difference in the forthcoming analysis.

The calculated spectrum of bottomonium and charmonium states is listed in Table 1.1 and 1.2, respectively.

1.2.2 The First Excited Quenched Potential

The excited state potentials have been calculated in quenched lattice QCD [53, 67]. They correspond to a $Q\bar{Q}$ pair in presence of an excited stationary state of the gluon field, which is usually associated to quarkonium hybrids, denoted sometimes as $Q\bar{Q}g$. Here we shall concentrate exclusively on the lowest hybrid potential, which, as in the quarkonium case, is a radial potential $V_1(\boldsymbol{r}) = V_1(r)$. In Reference [54] it has been parametrized as

$$V_1(r) = \begin{cases} \frac{0.24}{r_0^3} r^2 + \frac{0.11}{r} + \frac{2.8}{r_0} + E_0, & \text{if } r < r_*, \\ \sigma r \sqrt{1 + \frac{11\pi}{6\sigma r^2}} + E_0, & \text{if } r \geq r_*, \end{cases} \tag{1.13}$$

Table 1.2: Calculated spectrum of charmonium states with $l = 0, 1, 2, 3$ and masses up to 4.1 GeV.

nL	M (MeV)
$1S$	3082.5
$1P$	3510.9
$2S$	3673.2
$1D$	3795.8
$2P$	3953.7
$1F$	4033.8
$3S$	4097.0

where E_0 is the same additive constant that appeared in the ground state potential (1.10), $r_0 \approx 0.5$ fm, and $r_* = 2r_0$ is a matching radius between the short/intermediate distance parametrization (first line) and the long distance one (second line). As shown in Figure 1.2, this hybrid potential shows a repulsive Coulomb interaction at short distances, as expected from a constituent picture where the $Q\bar{Q}$ is in a color-octet state. On the other hand, at large distances it behaves very similarly to a (excited) string potential, as expected from flux tube models [68].

As shown in [54], and reproduced for completeness in Appendix A, the mass and wave function of the lowest quarkonium hybrid state can be calculated by plugging the hybrid potential (1.13) into a radial Schrödinger equation, which is formally the same Equation (1.11) with $i = 1$ and the constraint $l \geq 1$. Here it shall suffice to say that the constraint $l \geq 1$ arises from the fact that the first excited light-field state has quantum numbers different from the vacuum (unlike the ground state), what makes l to become an effective angular momentum incorporating the effect of the excited light fields into the $Q\bar{Q}$ orbital angular momentum.

It is important to realize that, since $l \geq 1$, the "centrifugal" term $l(l+1)/(2\mu r^2)$ dominates the potential at short distances. Consequently, the short-range Coulomb repulsion becomes practically irrelevant to the calculation of the spectrum, and Equation (1.13) can be effectively substituted by lowest vibrational string potential [69]

$$V_1(r) \underset{l\geq 1}{\approx} \sigma r \sqrt{1 + \frac{2\pi}{\sigma r^2}} + E_0.$$

From a phenomenological point of view, the vibrational potential approximation has the great advantage of allowing a calculation of the lowest

hybrid states without the introduction of any additional free parameter. Then, using the same parameters (1.12) of the ground state potential, the lowest bottomonium hybrid has a calculated mass of 10908.6 MeV, while that of the lowest charmonium hybrid is 4327.4 MeV.

Let us notice that experimental identification of these lowest quarkonium hybrids may be not straightforward since they may mix with close-lying conventional quarkonium states with the same quantum numbers. Otherwise said, the NACTs mixing quarkonium and quarkonium hybrids, for which we have not yet any information from lattice QCD, may not be negligible. In fact, in Reference [57] it has been shown (using slightly different values of the parameters in the potentials) that the experimental $\Upsilon(10860)$, a bottomonium-like resonance with an average mass of 1855.2 MeV [70], may be the result of the mixing of the lowest bottomonium hybrid with the $5S$ conventional bottomonium state. As for the lowest charmonium hybrid state, the situation is even more problematic as its mass lies in the proximity of a stack of open-charm meson-meson thresholds, including the very broad $D\bar{D}_1$ threshold, which complicates extraordinarily its theoretical treatment.

1.3 Spin Splittings

In order to make a detailed comparison of the calculated masses with data, one needs to consider corrections to the Hamiltonian coming from spin-dependent forces and other relativistic effects. These corrections, which are beyond the static limit, can also be calculated from the Wilson loop formalism [52]. To include them, we must introduce the spin of the heavy quarks in our formalism.

In single channel BO, the spin of the heavy quarks is completely decoupled from the quantum numbers of the light field configurations. Therefore, building a basis of wave functions including spin simply amounts to taking the external product of the basis of spinless wave functions by the basis of spin vectors (spinors) of the heavy quarks:

$$\underbrace{\left\{R_{i,l}(r)Y_l^{m_l}(\hat{\boldsymbol{r}})\right\}_{l,m_l}}_{\text{no spin}} \longrightarrow \underbrace{\left\{\xi_{s_Q}^{\sigma_Q}\xi_{s_{\bar{Q}}}^{\sigma_{\bar{Q}}}R_{i,l}(r)Y_l^{m_l}(\hat{\boldsymbol{r}})\right\}_{l,m_l,\sigma_Q,\sigma_{\bar{Q}}}}_{\text{with } Q \text{ and } \bar{Q} \text{ spin}}$$

with $\xi_{s_Q}^{\sigma_Q}$ the heavy quark spinor satisfying

$$\begin{aligned} S_Q^2\xi_{s_Q}^{\sigma_Q} &= s_Q(s_Q+1)\xi_{s_Q}^{\sigma_Q} \\ S_Q^z\xi_{s_Q}^{\sigma_Q} &= \sigma_Q\xi_{s_Q}^{\sigma_Q} \end{aligned}$$

where $\boldsymbol{S}_Q$ is the quark spin, and an analogous definition holds for the heavy antiquark spinor $\xi^{\sigma_{\bar{Q}}}_{s_{\bar{Q}}}$.

With the spin of the heavy quarks, before introducing relativistic corrections, one has an additional degeneracy in the spectrum of quarkonium states. Since a solution of Equation (1.11) with angular momentum l is degenerate $2l+1$ times (notice that there is no dependence on m_l in the radial Schrödinger equation), with the introduction of spin, $s_Q = s_{\bar{Q}} = 1/2$, we have that each quarkonium state is degenerate $4(2l+1)$ times. This degeneracy is removed by relativistic corrections, as they couple the spin of the heavy quarks to each other (spin-spin) and to the spatial degrees of freedom (spin-orbit, tensor,...) [52]. For this reason, neither the projections of the heavy quark spins, σ_Q and $\sigma_{\bar{Q}}$, nor that of the orbital angular momentum, m_l, are good quantum numbers to classify quarkonium states with relativistic corrections.

A convenient basis of wave functions for a quarkonium system with relativistic corrections is given by

$$\psi^{J,m_J}_{0,l,s}(\boldsymbol{r}) = R_{0,l}(r)\mathcal{Y}^{m_J}_{l,s,J}(\hat{\boldsymbol{r}}), \tag{1.14}$$

where the spin-orbital wave functions, which can be expressed as

$$\mathcal{Y}^{m_J}_{l,s,J}(\hat{\boldsymbol{r}}) = \sum_{m_l,m_s} C^{m_l,m_s,m_J}_{l,s,J} Y^{m_l}_l(\hat{\boldsymbol{r}}) \sum_{\sigma_Q,\sigma_{\bar{Q}}} C^{\sigma_Q,\sigma_{\bar{Q}},m_s}_{s_Q,s_{\bar{Q}},s} \xi^{\sigma_Q}_{s_Q} \xi^{\sigma_{\bar{Q}}}_{s_{\bar{Q}}}, \tag{1.15}$$

with C for Clebsch-Gordan coefficients, satisfy

$$\begin{aligned}
L^2\mathcal{Y}^{m_J}_{l,s,J}(\hat{\boldsymbol{r}}) &= l(l+1)\mathcal{Y}^{m_J}_{l,s,J}(\hat{\boldsymbol{r}}) \\
S^2\mathcal{Y}^{m_J}_{l,s,J}(\hat{\boldsymbol{r}}) &= s(s+1)\mathcal{Y}^{m_J}_{l,s,J}(\hat{\boldsymbol{r}}) \\
J^2\mathcal{Y}^{m_J}_{l,s,J}(\hat{\boldsymbol{r}}) &= J(J+1)\mathcal{Y}^{m_J}_{l,s,J}(\hat{\boldsymbol{r}}) \\
J^z\mathcal{Y}^{m_J}_{l,s,J}(\hat{\boldsymbol{r}}) &= m_J\mathcal{Y}^{m_J}_{l,s,J}(\hat{\boldsymbol{r}})
\end{aligned}$$

with $\boldsymbol{S} = \boldsymbol{S}_Q + \boldsymbol{S}_{\bar{Q}}$ the total $Q\bar{Q}$ spin and $\boldsymbol{J} = \boldsymbol{L} + \boldsymbol{S}$ the total angular momentum. Notice that the spin-orbital wave functions satisfy the orthogonality condition

$$\int \mathrm{d}\hat{\boldsymbol{r}}\mathcal{Y}^{m_J\dagger}_{l,s,J}(\hat{\boldsymbol{r}})\mathcal{Y}^{m'_J}_{l',s',J'}(\hat{\boldsymbol{r}}) = \delta_{ll'}\delta_{ss'}\delta_{JJ'}\delta_{m_Jm_{J'}}. \tag{1.16}$$

The states given in Equation (1.14) are usually labeled with the spectral notation $n\,^{2s+1}L_J$. Notice that, in general, there is a residual $2J+1$ degeneracy (the number of distinct values of m_J) for each state with $J > 0$, linked to conservation of the total angular momentum $\boldsymbol{J}$. Notice also that these states are eigenvalues of parity and charge-conjugation parity with eigenvalues $P = (-1)^{l+1}$ and $C = (-1)^{l+s}$, respectively.

Table 1.3: Calculated spectrum, $M_{\rm Theor}$, of low-lying bottomonium states, including corrections from Table II of Reference [52]. Central mass values of available experimental candidates from [70], $M_{\rm Expt}$, are listed for comparison. States are grouped by J^{PC} families.

J^{PC}	$n\,^{2s+1}L_J$	$M_{\rm Theor}$ (MeV)	$M_{\rm Expt}$ (MeV)	PDG State
0^{++}	$1\,^3P_0$	9864.9	9859.4	$\chi_{b0}(1P)$
	$2\,^3P_0$	10228.1	10232.5	$\chi_{b0}(2P)$
1^{++}	$1\,^3P_1$	9889.7	9892.8	$\chi_{b1}(1P)$
	$2\,^3P_1$	10246.3	10255.5	$\chi_{b1}(2P)$
2^{++}	$1\,^3P_2$	9914.5	9912.2	$\chi_{b2}(1P)$
	$2\,^3P_2$	10264.7	10268.7	$\chi_{b2}(2P)$
1^{--}	$1\,^3S_1$	9425.0	9460.3	$\Upsilon(1S)$
	$2\,^3S_1$	10004.2	10023.3	$\Upsilon(2S)$
	$1\,^3D_1$	10137.8		
	$3\,^3S_1$	10346.5	10355.2	$\Upsilon(3S)$
	$2\,^3D_1$	10431.1		
2^{--}	$1\,^3D_2$	10147.1	10163.7	$\Upsilon_2(1D)$
	$2\,^3D_2$	10439.3		
3^{--}	$1\,^3D_3$	10158.2		
	$2\,^3D_3$	10448.8		
1^{+-}	$1\,^1P_1$	9900.7	9899.3	$h_b(1P)$
	$2\,^1P_1$	10254.5	10259.8	$h_b(2P)$
0^{-+}	$1\,^1S_0$	9330.1	9398.7	$\eta_b(1S)$
	$2\,^1S_0$	9963.0		
	$3\,^1S_0$	10315.1		
2^{-+}	$1\,^1D_2$	10150.4		
	$2\,^1D_2$	10442.1		

Table 1.4: Calculated spectrum, $M_{\rm Theor}$, of low-lying charmonium states, including corrections from Table I of Reference [52].Central mass values of available experimental candidates from [70], $M_{\rm Expt}$, are listed for comparison. States are grouped by J^{PC} families.

J^{PC}	$n\,^{2s+1}L_J$	$M_{\rm Theor}$ (MeV)	$M_{\rm Expt}$ (MeV)	PDG State
0^{++}	$1\,^3P_0$	3416.8	3414.7	$\chi_{c0}(1P)$
1^{++}	$1\,^3P_1$	3481.5	3510.7	$\chi_{c1}(1P)$
2^{++}	$1\,^3P_2$	3547.4	3556.2	$\chi_{c2}(1P)$
1^{--}	$1\,^3S_0$	3114.9	3096.9	$J/\psi(1S)$
	$2\,^3S_1$	3693.9	3686.1	$\psi(2S)$
	$1\,^3D_1$	3747.3	3773.7	$\psi(3770)$
2^{--}	$1\,^3D_2$	3782.9	3823.7	$\psi_2(3823)$
3^{--}	$1\,^3D_3$	3825.6	3842.7	$\psi_3(3842)$
1^{+-}	$1\,^1P_1$	3510.9	3525.4	$h_c(1P)$
0^{-+}	$1\,^1S_0$	2985.1	2983.9	$\eta_c(1S)$
	$2\,^1S_0$	3611.0	3637.5	$\eta_c(2S)$
2^{-+}	$1\,^1D_2$	3795.8		

In quarkonium, we can take advantage of the spin corrections already calculated in [52] to obtain a spectrum of quarkonium states with spin splittings. The calculated spectra of bottomonium and charmonium states, including spin and relativistic corrections, are listed and compared to experimental candidates from the Particle Data Group (PDG) [70] in Tables 1.3 and 1.4, respectively. As one can see, the quarkonium spectrum can give complete account of the low-lying experimental states. As for the accuracy of the predicted masses, one should take into account that some uncertainty coming from possible additional relativistic effects (presumably more relevant in the lowest-lying states) may have been partly propagated through the effective values of the parameters we have put in the quarkonium potential (1.10).

As for spin splittings of quarkonium hybrid states, we refer the reader to [71, 72] for their calculation in a different BO framework [64] which utilizes an EFT language.

Chapter 2

Radiative Transitions in Quarkonium

In this chapter, we derive from QED a general formula for calculating the EM transition rates using the quarkonium wave functions determined in BO. More precisely, in Section 2.1 we derive the general transition operator from QED. Then, in Section 2.2, we introduce the dipole approximation and reduce the transition operator to the form commonly found in the literature, see, for example, [73] and references therein. Finally, in Section 2.3, we briefly show how the dipole approximation can be overcome.

2.1 The QED Transition Operator

2.1.1 Second-Quantized Form

The transition amplitude for a radiative decay $A \to B\gamma$, where A and B stand for initial and final quarkonium states, respectively, and γ for a photon, can be calculated as the sum of the amplitudes for the individual of Q and $\bar{Q}$ interacting with the EM field while the other acts as spectator, see Figure 2.1.

In QED, the transition probability can be calculated perturbatively from the interaction Hamiltonian

$$H_{\mathrm{QED}}^{\mathrm{int}} = \int \mathrm{d}\boldsymbol{x} A_\mu(\boldsymbol{x}, t) j^\mu(\boldsymbol{x}, t), \tag{2.1}$$

which couples the quark EM current,

$$j^\mu(\boldsymbol{x}, t) = e\bar{q}(\boldsymbol{x}, t)\gamma^\mu q(\boldsymbol{x}, t),$$

with the EM field A_μ, where $\bar{q} = q^\dagger\gamma^0$ and, as customary, a sum over repeated covariant indices is understood. Notice that for the Dirac matrices γ^μ we use

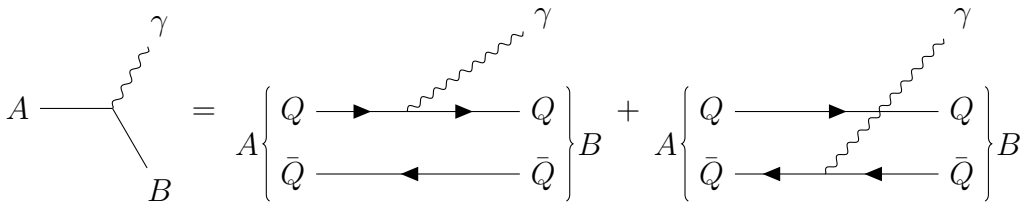

Figure 2.1: Diagrammatic representation of the decay of a $Q\bar{Q}$ system from an initial state A to a final state B plus a photon.

the Dirac convention

$$\gamma^0 = \begin{pmatrix} I & 0 \\ 0 & -I \end{pmatrix}, \qquad \boldsymbol{\gamma} = \begin{pmatrix} 0 & \boldsymbol{\sigma} \\ \boldsymbol{\sigma} & 0 \end{pmatrix},$$

with $\boldsymbol{\sigma} = (\sigma_1, \sigma_2, \sigma_3)$ the Pauli matrices

$$\sigma_1 = \begin{pmatrix} 0 & 1 \\ 1 & 0 \end{pmatrix}, \quad \sigma_2 = \begin{pmatrix} 0 & -i \\ i & 0 \end{pmatrix}, \quad \sigma_3 = \begin{pmatrix} 1 & 0 \\ 0 & -1 \end{pmatrix}.$$

The second-quantized quark field $q(\boldsymbol{x}, t)$ is expressed in terms of solutions to the Dirac equation,

$$(i\gamma^\mu \partial_\mu - m) q(\boldsymbol{x}, t) = 0$$

with m the quark mass, namely

$$q_+^s(\boldsymbol{x}, t) = u^s(\boldsymbol{p}) e^{i(\boldsymbol{p}\cdot\boldsymbol{x} - Et)} \quad \text{and} \quad q_-^s(\boldsymbol{x}, t) = v^s(\boldsymbol{p}) e^{-i(\boldsymbol{p}\cdot\boldsymbol{x} - Et)},$$

where we have introduced the Dirac spinors

$$u^s(\boldsymbol{p}) = \sqrt{m+E} \begin{pmatrix} \chi^s \\ \frac{\boldsymbol{p}\cdot\boldsymbol{\sigma}}{m+E}\chi^s \end{pmatrix}, \qquad v^s(\boldsymbol{p}) = \sqrt{m+E} \begin{pmatrix} \frac{\boldsymbol{p}\cdot\boldsymbol{\sigma}}{m+E}\chi^s \\ \chi^s \end{pmatrix} \tag{2.2}$$

with χ^s the Pauli spinors with normalization $\chi^{s\dagger}\chi^{s'} = \delta_{ss'}$. These solutions are associated to a freely propagating quark (q_+^s), or antiquark (q_-^s), with spin projection s, momentum $\boldsymbol{p}$, and energy $E = \sqrt{m^2 + p^2}$. Note that the Dirac spinors are normalized as

$$\bar{u}^s(\boldsymbol{p}) u^{s'}(\boldsymbol{p}) = 2m\delta_{ss'}, \qquad \bar{v}^s(\boldsymbol{p}) v^{s'}(\boldsymbol{p}) = -2m\delta_{ss'},$$

and

$$u^{s\dagger}(\boldsymbol{p}) u^{s'}(\boldsymbol{p}) = 2E\delta_{ss'}, \qquad v^{s\dagger}(\boldsymbol{p}) v^{s'}(\boldsymbol{p}) = 2E\delta_{ss'},$$

while spinors corresponding to positive and negative frequencies satisfy orthogonality relations

$$\bar{u}^s(\boldsymbol{p})v^{s'}(\boldsymbol{p}) = \bar{v}^s(\boldsymbol{p})u^{s'}(\boldsymbol{p}) = 0,$$

and

$$u^{s\dagger}(\boldsymbol{p})v^{s'}(-\boldsymbol{p}) = v^{s\dagger}(\boldsymbol{p})u^{s'}(-\boldsymbol{p}) = 0.$$

With this notation, we expand the second-quantized, relativistic quark field as

$$q(\boldsymbol{x},t) = \int \frac{\mathrm{d}\boldsymbol{p}}{(2\pi)^3}\frac{1}{\sqrt{2E}}\sum_s (u^s(\boldsymbol{p})b_1^s(\boldsymbol{p})e^{i(\boldsymbol{p}\cdot\boldsymbol{x}-Et)} + v^s(\boldsymbol{p})b_2^{s\dagger}(\boldsymbol{p})e^{-i(\boldsymbol{p}\cdot\boldsymbol{x}-Et)}), \tag{2.3}$$

where $b_1^s(\boldsymbol{p})$ and $b_2^s(\boldsymbol{p})$ are, respectively, the operators that annihilate a quark or antiquark with spin projection s and three-momentum $\boldsymbol{p}$. Their adjoint, $b_1^{s\dagger}(\boldsymbol{p})$ and $b_2^{s\dagger}(\boldsymbol{p})$, respectively, do exactly the opposite, and are thus called creation operators. The creation and annihilation operators obey the anticommutation relations

$$\left\{b_n^s(\boldsymbol{p}), b_{n'}^{s'\dagger}(\boldsymbol{q})\right\} = \delta_{ij}(2\pi)^3\delta_{ss'}\delta(\boldsymbol{p}-\boldsymbol{q})$$

with all the other possible anticommutators being zero, where $n, n' = 1, 2$ label the quark and antiquark operators.

The EM field in the so-called "radiation" gauge ($A^0(\boldsymbol{x},t) = 0$) is expressed as

$$\boldsymbol{A}(\boldsymbol{x},t) = \int \frac{\mathrm{d}\boldsymbol{k}}{(2\pi)^3}\frac{1}{\sqrt{2k_0}}\sum_{\lambda=\pm1}(\boldsymbol{\varepsilon}_{\boldsymbol{k}}^{\lambda}\, a_{\boldsymbol{k}}^{\lambda}e^{i(\boldsymbol{k}\cdot\boldsymbol{x}-k_0t)} + \boldsymbol{\varepsilon}_{\boldsymbol{k}}^{\lambda *}\, a_{\boldsymbol{k}}^{\lambda\dagger}e^{-i(\boldsymbol{k}\cdot\boldsymbol{x}-k_0t)}).$$

We define the polarization vectors in the spherical basis

$$\boldsymbol{\varepsilon}_{k\hat{\boldsymbol{z}}}^{\pm1} = \mp\frac{\hat{\boldsymbol{x}} \pm i\hat{\boldsymbol{y}}}{\sqrt{2}},$$

and accordingly the creation and annihilation operators are defined in terms of the "Cartesian" ones as

$$a_{k\hat{\boldsymbol{z}}}^{\pm1} = \mp\frac{a_{k\hat{\boldsymbol{z}}}^x \mp i a_{k\hat{\boldsymbol{z}}}^y}{\sqrt{2}}$$

satisfying the commutation relations

$$\left[a_{\boldsymbol{k}}^{\lambda}, a_{\boldsymbol{k'}}^{\lambda'\dagger}\right] = (2\pi)^3\delta_{\lambda\lambda'}\delta(\boldsymbol{k}-\boldsymbol{k'}).$$

The reason for choosing the spherical over the Cartesian basis is that in this way the Fock space of the EM sector consists in photons with a definite value of the helicity, λ.

Using (2.3), the components of the EM current j^μ can be written as

$$j^0(\boldsymbol{x},t) = \sum_{n=1}^{2} e_n \Bigg(q_n^\dagger(\boldsymbol{x},t) q_n(\boldsymbol{x},t) + \frac{\boldsymbol{\nabla}}{m+i\partial_t} q_n^\dagger(\boldsymbol{x},t) \cdot \frac{\boldsymbol{\nabla}}{m+i\partial_t} q_n(\boldsymbol{x},t) + i\boldsymbol{\sigma}_{(n)} \cdot \frac{\boldsymbol{\nabla}}{m+i\partial_t} q_n^\dagger(\boldsymbol{x},t) \times \frac{\boldsymbol{\nabla}}{m+i\partial_t} q_n(\boldsymbol{x},t) \Bigg) \quad (2.4)$$

and

$$\begin{aligned} &\boldsymbol{j}(\boldsymbol{x},t) = \\ &\sum_{n=1}^{2} e_n \Bigg\{ -i \Bigg[q_n^\dagger(\boldsymbol{x},t) \left(\frac{\boldsymbol{\nabla}}{m+i\partial_t} q_n(\boldsymbol{x},t) \right) - \left(\frac{\boldsymbol{\nabla}}{m+i\partial_t} q_n^\dagger(\boldsymbol{x},t) \right) q_n(\boldsymbol{x},t) \Bigg] \\ &+ \left(\frac{\boldsymbol{\nabla}}{m+i\partial_t} q_n^\dagger(\boldsymbol{x},t) \right) \times \boldsymbol{\sigma}_{(n)} q_n(\boldsymbol{x},t) - q_n^\dagger(\boldsymbol{x},t) \boldsymbol{\sigma}_{(n)} \times \left(\frac{\boldsymbol{\nabla}}{m+i\partial_t} q_n(\boldsymbol{x},t) \right) \Bigg\}, \end{aligned} \quad (2.5)$$

respectively, where we have introduced the quark ($n = 1$) and antiquark ($n = 2$) fields

$$q_n(\boldsymbol{x},t) = \int \frac{\mathrm{d}\boldsymbol{p}}{(2\pi)^3} \sqrt{\frac{m+E}{2E}} \sum_s \chi_n^s b_n^s(\boldsymbol{p}) e^{i(\boldsymbol{p}\cdot\boldsymbol{x} - Et)}$$

with

$$e_n = (-1)^{n+1} \sqrt{4\pi\alpha}\, \mathcal{Q}$$

the quark electric charge, given in terms of the modulus of the electron charge $\sqrt{4\pi\alpha}$ and the fractional quark charge $\mathcal{Q}$. Notice that the antiquark charge e_2 is opposite to the quark one e_1 by definition. Note that the subscript (n) in the Pauli matrices indicates which spinor the matrix acts on (quark or antiquark), and that in the derivation of Equations (2.4) and (2.5) we used normal ordering and kept only those operators that conserve the number of quarks and antiquarks separately, since they are the only operators contributing in a photon emission/absorption process.

2.1.2 First-Quantized Form

In order to calculate the transition matrix elements with the BO quarkonium wave functions, we have to write, from the former second-quantized expressions, the first-quantized form of the transition operator [74]. So, the current

operator of Equations (2.4) and (2.5) can be translated into a first-quantized form as

$$j^0(\boldsymbol{r}_1,\boldsymbol{r}_2,\boldsymbol{x},t) = \sum_{n=1}^{2} e_n\sqrt{\frac{m+E_n}{2E_n}}\Bigg(\delta(\boldsymbol{x}-\boldsymbol{r}_n)+\frac{\boldsymbol{p}_n}{m+E_n}\cdot\delta(\boldsymbol{x}-\boldsymbol{r}_n)\frac{\boldsymbol{p}_n}{m+E_n} + i\boldsymbol{\sigma}_{(n)}\cdot\frac{\boldsymbol{p}_n}{m+E_n}\times\delta(\boldsymbol{x}-\boldsymbol{r}_n)\frac{\boldsymbol{p}_n}{m+E_n}\Bigg)\sqrt{\frac{m+E_n}{2E_n}}$$

and

$$\boldsymbol{j}(\boldsymbol{r}_1,\boldsymbol{r}_2,\boldsymbol{x},t) = \sum_{n=1}^{2} e_n\sqrt{\frac{m+E_n}{2E_n}}\Bigg[\delta(\boldsymbol{x}-\boldsymbol{r}_n)\frac{\boldsymbol{p}_n}{m+E_n}+\frac{\boldsymbol{p}_n}{m+E_n}\delta(\boldsymbol{x}-\boldsymbol{r}_n) - i\boldsymbol{\sigma}_{(n)}\times\left(\delta(\boldsymbol{x}-\boldsymbol{r}_n)\frac{\boldsymbol{p}_n}{m+E_n}-\frac{\boldsymbol{p}_n}{m+E_n}\delta(\boldsymbol{x}-\boldsymbol{r}_n)\right)\Bigg]\sqrt{\frac{m+E_n}{2E_n}}, \quad (2.6)$$

respectively, where we have introduced the quark and antiquark coordinates $\boldsymbol{r}_n$, with the corresponding momentum, $\boldsymbol{p}_n \hookleftarrow -i\boldsymbol{\nabla}_n$, and energy, $E_n = \sqrt{m^2+p_n^2}$, first-quantized operators.

Inserting the vector current (2.6) in Equation (2.1) gives the first-quantized interaction Hamiltonian

$$H^{\text{int}}_{\text{QED}}(\boldsymbol{r}_1,\boldsymbol{r}_2,t) = -\sum_{n=1}^{2} e_n\sqrt{\frac{m+E_n}{2E_n}}\Bigg[\boldsymbol{A}(\boldsymbol{r}_n,t)\cdot\frac{\boldsymbol{p}_n}{m+E_n}+\frac{\boldsymbol{p}_n}{m+E_n}\cdot\boldsymbol{A}(\boldsymbol{r}_n,t) - i\boldsymbol{\sigma}_{(n)}\times\left(\boldsymbol{A}(\boldsymbol{r}_n,t)\cdot\frac{\boldsymbol{p}_n}{m+E_n}-\frac{\boldsymbol{p}_n}{m+E_n}\cdot\boldsymbol{A}(\boldsymbol{r}_n,t)\right)\Bigg]\sqrt{\frac{m+E_n}{2E_n}},$$

from which we can obtain the QED transition operator for the emission of a photon with momentum $\boldsymbol{k}$, energy $k_0 = |\boldsymbol{k}|$, and helicity λ from a quark-antiquark pair as

$$\langle\boldsymbol{k},\lambda|\, H^{\text{int}}_{\text{QED}}(\boldsymbol{r}_1,\boldsymbol{r}_2,t)\,|0\rangle = -\frac{1}{\sqrt{2k_0}}\sum_{n=1}^{2} e_n\sqrt{\frac{m+E_n}{2E_n}}\Bigg[e^{-i(\boldsymbol{k}\cdot\boldsymbol{r}_n-k_0t)}\frac{\boldsymbol{p}_n}{m+E_n}+\frac{\boldsymbol{p}_n}{m+E_n}e^{-i(\boldsymbol{k}\cdot\boldsymbol{r}_n-k_0t)} - i\boldsymbol{\sigma}_{(n)}\times\left(e^{-i(\boldsymbol{k}\cdot\boldsymbol{r}_n-k_0t)}\frac{\boldsymbol{p}_n}{m+E_n}-\frac{\boldsymbol{p}_n}{m+E_n}e^{-i(\boldsymbol{k}\cdot\boldsymbol{r}_n-k_0t)}\right)\Bigg]\cdot\boldsymbol{\varepsilon}^{\lambda*}_{\boldsymbol{k}}\sqrt{\frac{m+E_n}{2E_n}}. \quad (2.7)$$

Then, the transition matrix element between the initial and final $Q\bar{Q}$ bound states, represented, respectively, by the wave functions

$$\Psi_i(\boldsymbol{r},\boldsymbol{R},t) = \psi_i(\boldsymbol{r})e^{i(\boldsymbol{P}_i\cdot\boldsymbol{R}-E_it)},$$
$$\Psi_f(\boldsymbol{r},\boldsymbol{R},t) = \psi_f(\boldsymbol{r})e^{i(\boldsymbol{P}_f\cdot\boldsymbol{R}-E_ft)}$$

with $\psi_i(\boldsymbol{r})$ and $\psi_f(\boldsymbol{r})$, respectively, the internal wave function of the initial and final state, can be expressed as

$$\int \mathrm{d}\boldsymbol{r}\,\mathrm{d}\boldsymbol{R}\,\mathrm{d}t\,\Psi_f^*(\boldsymbol{r},\boldsymbol{R},t)\,\langle\boldsymbol{k},\lambda|\,H_{\mathrm{QED}}^{\mathrm{int}}(\boldsymbol{r},\boldsymbol{R},t)\,|0\rangle\,\Psi_i(\boldsymbol{r},\boldsymbol{R},t) = \\ \delta(E_i-(E_f+k_0))\delta(\boldsymbol{P_i}-(\boldsymbol{P}_f+\boldsymbol{k}))\frac{1}{\sqrt{2k_0}}\mathcal{M}_{\mathrm{QED}}^{f\leftarrow i}(\boldsymbol{k},\lambda).$$

Finally, the width for the decay of a $Q\bar{Q}$ bound state through the emission of a photon, $\Gamma(i\to f\gamma)$, reads

$$\Gamma(i\to f\gamma) = \frac{k_0}{2\pi}\frac{E_iE_f}{M_i^2}\frac{1}{2J_i+1}\sum_{\lambda=\pm1}\sum_{m_{J_i},m_{J_f}}|\mathcal{M}_{\mathrm{QED}}^{f\leftarrow i}(\boldsymbol{k},\lambda)|^2.$$

In the rest of this chapter, we shall give explicit expressions for $\mathcal{M}_{\mathrm{QED}}^{f\leftarrow i}(\boldsymbol{k},\lambda)$.

2.2 The Dipole Approximation

Historically, the QED transition operator (2.7) has been used in a simplified form given by the dipole approximation, which consists of a nonrelativistic (NR) approximation for the heavy quarks followed by a long wavelength (LWL) approximation for the emitted photon.

2.2.1 Nonrelativistic Approximation

The NR approximation for the heavy quarks allows to expand the transition operator in powers of p/m and neglect terms of order $(p/m)^2$ and higher. Concretely, in the case of (2.7), this amounts to approximating the heavy-quark energy by its mass, $E_n \approx m$, which results in the NR transition operator

$$\langle\boldsymbol{k},\lambda|\,H_{\mathrm{NR}}^{\mathrm{int}}(\boldsymbol{r}_1,\boldsymbol{r}_2,t)\,|0\rangle = \\ -\frac{e^{ik_0t}}{\sqrt{2k_0}}\sum_{n=1}^{2}\frac{e_n}{2m}\big(e^{-i\boldsymbol{k}\cdot\boldsymbol{r}_n}\boldsymbol{p}_n+\boldsymbol{p}_ne^{-i\boldsymbol{k}\cdot\boldsymbol{r}_n}-i\boldsymbol{\sigma}_{(n)}\times\boldsymbol{k}\,e^{-i\boldsymbol{k}\cdot\boldsymbol{r}_n}\big)\cdot\boldsymbol{\varepsilon}_{\boldsymbol{k}}^{\lambda*},$$

where in the last line we have used

$$e^{-i\boldsymbol{k}\cdot\boldsymbol{r}_n}\boldsymbol{p}_n - \boldsymbol{p}_n e^{-i\boldsymbol{k}\cdot\boldsymbol{r}_n} = \boldsymbol{k}e^{-i\boldsymbol{k}\cdot\boldsymbol{r}_n}.$$

To calculate the transition matrix element, it is convenient to express the quark and antiquark positions and momenta in terms of the relative and center-of-mass ones,

$$\boldsymbol{r}_n = \boldsymbol{R} + (-1)^{n+1}\frac{\boldsymbol{r}}{2}, \qquad \boldsymbol{p}_n = \frac{\boldsymbol{P}}{2} + (-1)^{n+1}\boldsymbol{p},$$

which gives

$$\begin{aligned}\mathcal{M}^{f\leftarrow i}_{\rm NR}(\boldsymbol{k},\lambda) = -\sqrt{4\pi\alpha}\frac{\mathcal{Q}}{2m}\sum_{n=1}^{2}\int \mathrm{d}\boldsymbol{r}\,\psi_f^*(\boldsymbol{r}) \\ \Big[e^{i(-1)^n\frac{\boldsymbol{k}\cdot\boldsymbol{r}}{2}}\boldsymbol{p} + \boldsymbol{p}e^{i(-1)^n\frac{\boldsymbol{k}\cdot\boldsymbol{r}}{2}} + i(-1)^n\boldsymbol{\sigma}_{(n)}\times\boldsymbol{k}\,e^{i(-1)^n\frac{\boldsymbol{k}\cdot\boldsymbol{r}}{2}} \\ - (-1)^n(2\boldsymbol{P}_i - \boldsymbol{k})e^{i(-1)^n\frac{\boldsymbol{k}\cdot\boldsymbol{r}}{2}}\Big]\psi_i(\boldsymbol{r})\cdot\boldsymbol{\varepsilon}^{\lambda *}_{\boldsymbol{k}}.\end{aligned}$$

In the center-of-mass rest frame of the initial state, one has $\boldsymbol{P}_i = 0$ and the above equation simplifies into

$$\begin{aligned}\mathcal{M}^{f\leftarrow i}_{\rm NR}(\boldsymbol{k},\lambda) = -\sqrt{4\pi\alpha}\frac{\mathcal{Q}}{2m}\sum_{n=1}^{2}\int \mathrm{d}\boldsymbol{r}\,\psi_f^*(\boldsymbol{r}) \\ \Big(e^{i(-1)^n\frac{\boldsymbol{k}\cdot\boldsymbol{r}}{2}}\boldsymbol{p} + \boldsymbol{p}e^{i(-1)^n\frac{\boldsymbol{k}\cdot\boldsymbol{r}}{2}} + i(-1)^n\boldsymbol{\sigma}_{(n)}\times\boldsymbol{k}\,e^{i(-1)^n\frac{\boldsymbol{k}\cdot\boldsymbol{r}}{2}}\Big)\psi_i(\boldsymbol{r})\cdot\boldsymbol{\varepsilon}^{\lambda *}_{\boldsymbol{k}}, \quad (2.8)\end{aligned}$$

where we have used

$$\boldsymbol{k}\cdot\boldsymbol{\varepsilon}^{\lambda *}_{\boldsymbol{k}} = 0.$$

2.2.2 Long Wavelength Approximation

The LWL approximation for the emitted photon consists in assuming $\boldsymbol{k}\cdot\boldsymbol{r} \ll 1$, which is equivalent to approximating $e^{i(-1)^n\frac{\boldsymbol{k}\cdot\boldsymbol{r}}{2}} \approx 1$ in (2.8). This gives

$$\mathcal{M}^{f\leftarrow i}_{\rm LWL}(\boldsymbol{k},\lambda) = -\sqrt{4\pi\alpha}\frac{\mathcal{Q}}{2m}\sum_{n=1}^{2}\int \mathrm{d}\boldsymbol{r}\,\psi_f^*(\boldsymbol{r})\big(2\boldsymbol{p} + i(-1)^n\boldsymbol{\sigma}_{(n)}\times\boldsymbol{k}\big)\psi_i(\boldsymbol{r})\cdot\boldsymbol{\varepsilon}^{\lambda *}_{\boldsymbol{k}}.$$

Moreover, by using

$$\boldsymbol{p} = -i\frac{m}{2}[\boldsymbol{r}, H]$$

where H is the Hamiltonian of the relative motion, one has

$$\int \mathrm{d}\boldsymbol{r}\, \psi_f^*(\boldsymbol{r})\boldsymbol{p}\psi_i(\boldsymbol{r}) = i\frac{m}{2}(M_f - M_i)\int \mathrm{d}\boldsymbol{r}\, \psi_f^*(\boldsymbol{r})\boldsymbol{r}\psi_i(\boldsymbol{r})$$

and $\mathcal{M}_{\mathrm{LWL}}^{f\leftarrow i}(\boldsymbol{k},\lambda)$ can be rewritten as

$$\mathcal{M}_{\mathrm{LWL}}^{f\leftarrow i}(\boldsymbol{k},\lambda) = i\sqrt{4\pi\alpha}\mathcal{Q} \int \mathrm{d}\boldsymbol{r}\, \psi_f^*(\boldsymbol{r})\left[(M_i - M_f)\boldsymbol{r} + \frac{1}{2m}\big(\boldsymbol{\sigma}_{(1)} - \boldsymbol{\sigma}_{(2)}\big)\times\boldsymbol{k}\right]\psi_i(\boldsymbol{r})\cdot\boldsymbol{\varepsilon}_{\boldsymbol{k}}^{\lambda *}. \quad (2.9)$$

2.2.3 Electric and Magnetic Amplitudes

The transition amplitude (2.9) is usually represented as the sum of electric dipole (E1) and magnetic quadrupole (M2) amplitudes,

$$\mathcal{M}_{\mathrm{LWL}}^{f\leftarrow i}(\boldsymbol{k},\lambda) = \mathcal{M}_{\mathrm{E1}}^{f\leftarrow i}(\boldsymbol{k},\lambda) + \mathcal{M}_{\mathrm{M2}}^{f\leftarrow i}(\boldsymbol{k},\lambda)$$

with

$$\mathcal{M}_{\mathrm{E1}}^{f\leftarrow i}(\boldsymbol{k},\lambda) = i\sqrt{4\pi\alpha}\mathcal{Q}(M_i - M_f)\,\langle\psi_f|\boldsymbol{r}\cdot\boldsymbol{\varepsilon}_{\boldsymbol{k}}^{\lambda *}|\psi_i\rangle$$

and

$$\mathcal{M}_{\mathrm{M2}}^{f\leftarrow i}(\boldsymbol{k},\lambda) = i\sqrt{4\pi\alpha}\frac{\mathcal{Q}}{2m}\,\langle\psi_f|\big(\boldsymbol{\sigma}_{(1)} - \boldsymbol{\sigma}_{(2)}\big)\times\boldsymbol{k}\cdot\boldsymbol{\varepsilon}_{\boldsymbol{k}}^{\lambda *}|\psi_i\rangle\,,$$

where we have adopted a shorthand bracket notation for the matrix elements between the internal wave functions $\psi_f(\boldsymbol{r})$ and $\psi_i(\boldsymbol{r})$.

These amplitudes can be calculated explicitly by expressing the internal wave functions in terms of their radial and spin-orbital parts,

$$\psi_i(\boldsymbol{r}) = \mathcal{Y}_{l_i,s_i,J_i}^{m_{J_i}}(\hat{\boldsymbol{r}})\frac{u_{i,l_i}(r)}{r},$$
$$\psi_f(\boldsymbol{r}) = \mathcal{Y}_{l_f,s_f,J_f}^{m_{J_f}}(\hat{\boldsymbol{r}})\frac{u_{f,l_f}(r)}{r}.$$

In fact, after some SU(2) algebra, one finds

$$\mathcal{M}_{\mathrm{E1}}^{f\leftarrow i}(\boldsymbol{k},\lambda) = i\sqrt{4\pi\alpha}\mathcal{Q}\delta_{s_i s_f}(-1)^{l_i}\sqrt{2l_f+1}C_{1,J_f,J_i}^{\lambda,m_{J_f},m_{J_i}} \begin{pmatrix} l_f & 1 & l_i \\ 0 & 0 & 0 \end{pmatrix}\begin{bmatrix} 1 & l_f & l_i \\ s_f & J_i & J_f \end{bmatrix}(M_i - M_f)\,\langle u_{f,l_f}|r|u_{i,l_i}\rangle$$

and

$$\mathcal{M}_{\mathrm{M2}}^{f\leftarrow i}(\boldsymbol{k},\lambda) = i\sqrt{4\pi\alpha}\frac{\mathcal{Q}}{m}\frac{1+(-1)^{s_f-s_i}}{2}\lambda k(-1)^{l_i}\sqrt{3(2l_f+1)}C_{1,J_f,J_i}^{\lambda,m_{J_f},m_{J_i}} \begin{pmatrix} l_f & 0 & l_i \\ 0 & 0 & 0 \end{pmatrix}\begin{bmatrix} s_i & 1 & s_f \\ 1/2 & 1/2 & 1/2 \end{bmatrix}\begin{bmatrix} l_f & 0 & l_i \\ s_f & 1 & s_i \\ J_f & 1 & J_i \end{bmatrix}\langle u_{f,l_f}|u_{i,l_i}\rangle\,,$$

with

$$\begin{pmatrix} j_1 & j_2 & j_3 \\ m_1 & m_2 & m_3 \end{pmatrix}$$

the Wigner 3j-symbol,

$$\begin{bmatrix} j_1 & j_2 & J_{12} \\ j_3 & J & J_{23} \end{bmatrix} = (-1)^{j_1+j_2+j_3+J}\sqrt{(2J_{12}+1)(2J_{23}+1)}\begin{Bmatrix} j_1 & j_2 & J_{12} \\ j_3 & J & J_{23} \end{Bmatrix}$$

a "modified" Wigner 6j-symbol, and

$$\begin{bmatrix} j_1 & j_2 & j_5 \\ j_3 & j_4 & j_6 \\ j_7 & j_8 & j_9 \end{bmatrix} = \sqrt{(2j_5+1)(2j_6+1)(2j_7+1)(2j_8+1)}\begin{Bmatrix} j_1 & j_2 & j_5 \\ j_3 & j_4 & j_6 \\ j_7 & j_8 & j_9 \end{Bmatrix}$$

a "modified" Wigner 9j-symbol.

From these expressions, and the properties of the Wigner nj-symbols, selection rules can be readily inferred. So, in the dipole approximation, EM transitions reduce to electric dipole transitions, with selection rules $s_f = s_i$ and $l_f = l_i \pm 1$, and magnetic quadrupole transitions, with selection rules $s_f \neq s_i$ and $l_f = l_i$.

The dipole approximation has played a prominent role in the analysis of radiative transitions in quarkonium. One should realize, though, that its application is only justified when the conditions $k\sqrt{\langle r^2\rangle} \ll 1$ and $\sqrt{\langle p^2\rangle}/m \ll 1$, where the average is taken with respect to either the initial or final state wave function, are satisfied.

2.3 Beyond the Dipole Approximation

2.3.1 Beyond Long Wavelength Photons

Although useful, the LWL approximation cannot be justified in some cases of practical interest, such as, for example, the radiative transitions $\chi_{bJ}(2P) \to \gamma\Upsilon((1,2)S)$ between bottomonium states [55]. In these cases, the exponentials in Equation (2.8) cannot be approximated as 1, and the calculation of the matrix element becomes much more complicated. The transition amplitude is instead expressed as a sum of electric and magnetic multipoles

$$\mathcal{M}_{\mathrm{NR}}^{f\leftarrow i}(\boldsymbol{k},\lambda) = \sum_{l=0}^{\infty}\big(\mathcal{E}_l^{f\leftarrow i}(\boldsymbol{k},\lambda) + \mathcal{B}_l^{f\leftarrow i}(\boldsymbol{k},\lambda)\big).$$

The electric contribution is given by

$$\mathcal{E}_l^{f\leftarrow i}(\boldsymbol{k},\lambda) = i\sqrt{4\pi\alpha}\mathcal{Q}\delta_{s_i s_f}(-1)^{l+l_f+l_i}(4l+1)\sum_{\tilde{n},\widetilde{J},\tilde{l}}(2\tilde{l}+1)$$
$$(M_i - M_{\tilde{n}})\,\langle u_{f,l_f}|j_{2l}(kr/2)|u_{\tilde{n},\tilde{l}}\rangle\,\langle u_{\tilde{n},\tilde{l}}|r|u_{i,l_i}\rangle\,C^{0,m_{J_f},m_{J_f}}_{2l,\widetilde{J},J_f}C^{\lambda,m_{J_f},m_{J_i}}_{1,\widetilde{J},J_i}$$
$$\begin{pmatrix}\tilde{l} & 2l & l_f\\ 0 & 0 & 0\end{pmatrix}\begin{pmatrix}\tilde{l} & 1 & l_i\\ 0 & 0 & 0\end{pmatrix}\begin{bmatrix}J_j & 2l & \widetilde{J}\\ \tilde{l} & s_f & l_f\end{bmatrix}\begin{bmatrix}J_i & 1 & \widetilde{J}\\ \tilde{l} & s_i & l_i\end{bmatrix}$$

or, equivalently, by

$$\mathcal{E}_l^{f\leftarrow i}(\boldsymbol{k},\lambda) = i\sqrt{4\pi\alpha}\mathcal{Q}\delta_{s_i s_f}(-1)^{l}(4l+1)\sqrt{(2l_i+1)(2l_f+1)}\sum_{\tilde{n},\widetilde{J},\tilde{l}}$$
$$(M_{\tilde{n}} - M_f)\,\langle u_{f,l_f}|r|u_{\tilde{n},\tilde{l}}\rangle\,\langle u_{\tilde{n},\tilde{l}}|j_{2l}(kr/2)|u_{i,l_i}\rangle\,C^{0,m_{J_i},m_{J_i}}_{2l,J_i,\widetilde{J}}C^{\lambda,m_{J_f},m_{J_i}}_{1,J_f,\widetilde{J}}$$
$$\begin{pmatrix}l_i & 2l & \tilde{l}\\ 0 & 0 & 0\end{pmatrix}\begin{pmatrix}l_f & 1 & \tilde{l}\\ 0 & 0 & 0\end{pmatrix}\begin{bmatrix}\widetilde{J} & 2l & J_i\\ l_i & s_i & \tilde{l}\end{bmatrix}\begin{bmatrix}\widetilde{J} & 1 & J_f\\ l_f & s_f & \tilde{l}\end{bmatrix}$$

with $j_l(z)$ the lth spherical Bessel function of the first kind, where a sum over intermediate quarkonium states, labeled by the quantum numbers $\tilde{n}$, $\tilde{l}$, $\widetilde{J}$, has been introduced.

The magnetic contribution, on the other hand, is given by

$$\mathcal{B}_l^{f\leftarrow i}(\boldsymbol{k},\lambda) = \sqrt{4\pi\alpha}\mathcal{Q}\frac{(-1)^l-(-1)^{s_f-s_i}}{2}$$
$$i^l\lambda\frac{k}{m}(-1)^{l_f+l}(2l+1)\sqrt{3(2l_f+1)}\,\langle u_{f,l_f}|j_l(kr/2)|u_{i,l_i}\rangle$$
$$\begin{pmatrix}l_f & l & l_i\\ 0 & 0 & 0\end{pmatrix}\begin{bmatrix}s_i & 1 & s_f\\ 1/2 & 1/2 & 1/2\end{bmatrix}\sum_{\widehat{J}}C^{0,\lambda,\lambda}_{l,1,\widehat{J}}C^{\lambda,m_{J_f},m_{J_i}}_{\widehat{J},J_f,J_i}\begin{bmatrix}l_f & l & l_i\\ s_f & 1 & s_i\\ J_f & \widehat{J} & J_i\end{bmatrix}$$

where it is intended that $\widehat{J}$ runs over positive integer values satisfying the triangular relation with l and 1. From these results, one can see that the main difference with respect to the LWL approximation is that selection rules on l are now relaxed, as a consequence of the expansion containing many multipoles.

2.3.2 Beyond Nonrelativistic Quark Currents

Even relaxing the LWL approximation, the use of the p/m expansion may not be justified for some radiative transitions in charmonium [56]. To calculate

the transition matrix element $\mathcal{M}_{\mathrm{QED}}^{f\leftarrow i}$ from the full relativistic expression of the transition operator (2.7), let us observe that the action of the quark energy operator E_n on the initial state $|\Psi_i\rangle$ is given by

$$\begin{aligned} E_n |\Psi_i\rangle &= \sqrt{m^2 + p_n^2}\, |\Psi_i\rangle \\ &= \sqrt{m^2 + \left|\frac{\boldsymbol{P}}{2} + (-1)^{n+1}\boldsymbol{p}\right|^2}\, |\Psi_i\rangle \\ &= \sqrt{m^2 + p^2}\, |\Psi_i\rangle\,, \end{aligned}$$

where we have used $\boldsymbol{P}_i = 0$ in the rest frame of the initial state. Therefore, in order to simplify the calculation, we shall order the factors containing E_n in Equation (2.7) so that they act directly on the initial state, this is, without interposition of the exponential factor $e^{-i(\boldsymbol{k}\cdot\boldsymbol{r}_n - k_0 t)}$. To do this reordering, let us realize that if the (anti-)quark emitting the photon has energy E_n in the initial state, after the emission, represented in first-quantized form by the operator $e^{-i(\boldsymbol{k}\cdot\boldsymbol{r}_n - k_0 t)}$, its energy must be $E_n - k_0$. Hence, for a general function $f(E_n)$ we may write

$$f(E_n) e^{-i(\boldsymbol{k}\cdot\boldsymbol{r}_n - k_0 t)} = e^{-i(\boldsymbol{k}\cdot\boldsymbol{r}_n - k_0 t)} f(E_n - k_0).$$

Then the transition matrix element can be written as

$$\begin{aligned} \mathcal{M}_{\mathrm{QED}}^{f\leftarrow i}(\boldsymbol{k},\lambda) = -\sqrt{4\pi\alpha}\frac{\mathcal{Q}}{2m}\sum_{n=1}^{2}\int \mathrm{d}\boldsymbol{r}\, \psi_f^*(\boldsymbol{r}) e^{i(-1)^n \frac{\boldsymbol{k}\cdot\boldsymbol{r}}{2}} \\ \left\{ 2\boldsymbol{p}\left(\frac{m}{m+E} + \frac{m}{m+E-k_0}\right) \right. \\ + i\boldsymbol{\sigma}_{(n)} \times \left[(-1)^n \boldsymbol{k} \frac{2m}{m+E-k_0} \right. \\ \left. \left. - 2\boldsymbol{p}\left(\frac{m}{m+E} - \frac{m}{m+E-k_0}\right) \right] \right\} g(E)\psi_i(\boldsymbol{r}) \cdot \boldsymbol{\varepsilon}_{\boldsymbol{k}}^{\lambda *} \end{aligned}$$

where we have defined $E = \sqrt{m^2 + p^2}$ and

$$g(E) = \sqrt{\frac{(m+E)(m+E-k_0)}{4E(E-k_0)}}.$$

Explicitly, it can be expressed as a sum

$$\mathcal{M}_{\mathrm{QED}}^{f\leftarrow i}(\boldsymbol{k},\lambda) = \sum_{l=0}^{\infty}\left(\mathcal{E}_l^{f\leftarrow i}(\boldsymbol{k},\lambda) + \mathcal{B}_l^{f\leftarrow i}(\boldsymbol{k},\lambda) + \widetilde{\mathcal{B}}_l^{f\leftarrow i}(\boldsymbol{k},\lambda)\right)$$

with $\widetilde{\mathcal{B}}_l^{f\leftarrow i}(\boldsymbol{k},\lambda)$ an additional magnetic contribution, absent in the NR limit.

The electric contribution can be written as

$$\mathcal{E}_l^{f\leftarrow i}(\boldsymbol{k},\lambda) =$$
$$i\sqrt{4\pi\alpha}\mathcal{Q}\delta_{s_i s_f}(-1)^{l+l_f+l_i}(4l+1)\sum_{\tilde{n},\widetilde{J},\tilde{l}}(2\tilde{l}+1)\,\langle u_{f,l_f}|j_{2l}\Big(\frac{kr}{2}\Big)|u_{\tilde{n},\tilde{l}}\rangle$$
$$\left[\sum_{n'}(M_{n'}-M_{\tilde{n}})\,\langle u_{\tilde{n},\tilde{l}}|r|u_{n',l_i}\rangle\,\langle u_{n',l_i}|\left(\frac{m}{m+E}+\frac{m}{m+E-k_0}\right)g(E)|u_{i,l_i}\rangle\right]$$
$$C^{0,m_{J_f},m_{J_f}}_{2l,\widetilde{J},J_f}C^{\lambda,m_{J_f},m_{J_i}}_{1,\widetilde{J},J_i}\begin{pmatrix}\tilde{l}&2l&l_f\\0&0&0\end{pmatrix}\begin{pmatrix}\tilde{l}&1&l_i\\0&0&0\end{pmatrix}\begin{bmatrix}J_j&2l&\widetilde{J}\\\tilde{l}&s_f&l_f\end{bmatrix}\begin{bmatrix}J_i&1&\widetilde{J}\\\tilde{l}&s_i&l_i\end{bmatrix}$$

or, equivalently, as

$$\mathcal{E}_l^{f\leftarrow i}(\boldsymbol{k},\lambda) =$$
$$i\sqrt{4\pi\alpha}\mathcal{Q}\delta_{s_i s_f}(-1)^{l}(4l+1)\sqrt{(2l_i+1)(2l_f+1)}\sum_{\tilde{n},\widetilde{J},\tilde{l}}(M_{\tilde{n}}-M_f)\,\langle u_{f,l_f}|r|u_{\tilde{n},\tilde{l}}\rangle$$
$$\left[\sum_{n'}\langle u_{\tilde{n},\tilde{l}}|j_{2l}(kr/2)|u_{n',l_i}\rangle\,\langle u_{n',l_i}|\left(\frac{m}{m+E}+\frac{m}{m+E-k_0}\right)g(E)|u_{i,l_i}\rangle\right]$$
$$C^{0,m_{J_i},m_{J_i}}_{2l,J_i,\widetilde{J}}C^{\lambda,m_{J_f},m_{J_i}}_{1,J_f,\widetilde{J}}\begin{pmatrix}l_i&2l&\tilde{l}\\0&0&0\end{pmatrix}\begin{pmatrix}l_f&1&\tilde{l}\\0&0&0\end{pmatrix}\begin{bmatrix}\widetilde{J}&2l&J_i\\l_i&s_i&\tilde{l}\end{bmatrix}\begin{bmatrix}\widetilde{J}&1&J_f\\l_f&s_f&\tilde{l}\end{bmatrix}$$

where an additional sum over intermediate states n', with the same angular momentum quantum numbers of the initial state, has been introduced.

The magnetic contributions $\mathcal{B}_l^{f\leftarrow i}(\boldsymbol{k},\lambda)$ and $\widetilde{\mathcal{B}}_l^{f\leftarrow i}(\boldsymbol{k},\lambda)$ can be written, respectively, as

$$\mathcal{B}_l^{f\leftarrow i}(\boldsymbol{k},\lambda) =$$
$$\sqrt{4\pi\alpha}\mathcal{Q}\frac{(-1)^l-(-1)^{s_f-s_i}}{2}i^l\lambda\frac{k}{m}(-1)^{l_f+l}(2l+1)\sqrt{3(2l_f+1)}$$
$$\left[\sum_{n'}\langle u_{f,l_f}|j_l(kr/2)|u_{n',l_i}\rangle\,\langle u_{n',l_i}|\frac{2m}{m+E-k_0}g(E)|u_{i,l_i}\rangle\right]$$
$$\begin{pmatrix}l_f&l&l_i\\0&0&0\end{pmatrix}\begin{bmatrix}s_i&1&s_f\\1/2&1/2&1/2\end{bmatrix}\sum_{\widehat{J}}C^{0,\lambda,\lambda}_{l,1,\widehat{J}}C^{\lambda,m_{J_f},m_{J_i}}_{\widehat{J},J_f,J_i}\begin{bmatrix}l_f&l&l_i\\s_f&1&s_i\\J_f&\widehat{J}&J_i\end{bmatrix}$$

and

$$\widetilde{\mathcal{B}}_l^{f\leftarrow i}(\boldsymbol{k},\lambda) = i\sqrt{4\pi\alpha}\mathcal{Q}\frac{(-1)^l+(-1)^{s_f-s_i}}{2}i^l\sqrt{6}(-1)^{l_f+l_i}(2l+1)$$
$$\sum_{\tilde{n},\widetilde{J},\tilde{l}}(2\tilde{l}+1)\,\langle u_{f,l_f}|j_l(kr/2)|u_{\tilde{n},\tilde{l}}\rangle\left[\sum_{n'}(M_{n'}-M_{\tilde{n}})\,\langle u_{\tilde{n},\tilde{l}}|r|u_{n',l_i}\rangle\right.$$
$$\left.\langle u_{n',l_i}|\left(\frac{m}{m+E}-\frac{m}{m+E-k_0}\right)g(E)|u_{i,l_i}\rangle\right]C^{0,m_{J_f},m_{J_f}}_{l,\widetilde{J},J_f}C^{\lambda,m_{J_f},m_{J_i}}_{1,\widetilde{J},J_i}$$
$$\begin{pmatrix}\tilde{l}&l&l_f\\0&0&0\end{pmatrix}\begin{pmatrix}\tilde{l}&1&l_i\\0&0&0\end{pmatrix}\begin{bmatrix}J_f&l&\widetilde{J}\\\tilde{l}&s_f&l_f\end{bmatrix}\begin{bmatrix}s_i&1&s_f\\1/2&1/2&1/2\end{bmatrix}\begin{bmatrix}\tilde{l}&1&l_i\\s_f&1&s_i\\\widetilde{J}&1&J_i\end{bmatrix}.$$

Alternatively, the two magnetic contributions can be also written, respectively, in the equivalent form

$$\mathcal{B}_l^{f\leftarrow i}(\boldsymbol{k},\lambda) = \sqrt{4\pi\alpha}\mathcal{Q}\frac{(-1)^l-(-1)^{s_f-s_i}}{2}i^l\lambda\frac{k}{m}(-1)^{l_f+l}(2l+1)\sqrt{3(2l_f+1)}$$
$$\left[\sum_{n'}\langle u_{f,l_f}|j_l(kr/2)|u_{n',l_i}\rangle\,\langle u_{n',l_i}|\left(\frac{m}{m+E}+\frac{m}{m+E-k_0}\right)g(E)|u_{i,l_i}\rangle\right]$$
$$\begin{pmatrix}l_f&l&l_i\\0&0&0\end{pmatrix}\begin{bmatrix}s_i&1&s_f\\1/2&1/2&1/2\end{bmatrix}\sum_{\widehat{J}}C^{0,\lambda,\lambda}_{l,1,\widehat{J}}C^{\lambda,m_{J_f},m_{J_i}}_{\widehat{J},J_f,J_i}\begin{bmatrix}l_f&l&l_i\\s_f&1&s_i\\J_f&\widehat{J}&J_i\end{bmatrix}$$

and

$$\widetilde{\mathcal{B}}_l^{f\leftarrow i}(\boldsymbol{k},\lambda) = i\sqrt{4\pi\alpha}\mathcal{Q}\frac{(-1)^l+(-1)^{s_f-s_i}}{2}i^l\sqrt{6}(-1)^{l_f+l_i}(2l+1)$$
$$\sqrt{(2l_i+1)(2l_f+1)}\sum_{\tilde{n},\widetilde{J},\tilde{l}}\langle u_{f,l_f}|j_l(kr/2)|u_{\tilde{n},\tilde{l}}\rangle\left[\sum_{n'}(M_{n'}-M_{\tilde{n}})\,\langle u_{\tilde{n},\tilde{l}}|r|u_{n',l_i}\rangle\right.$$
$$\left.\langle u_{n',l_i}|\left(\frac{m}{m+E}-\frac{m}{m+E-k_0}\right)g(E)|u_{i,l_i}\rangle\right]C^{0,m_{J_i},m_{J_i}}_{l,J_i,\widetilde{J}}C^{\lambda,m_{J_f},m_{J_i}}_{1,J_f,\widetilde{J}}$$
$$\begin{pmatrix}l_i&l&\tilde{l}\\0&0&0\end{pmatrix}\begin{pmatrix}l_f&1&\tilde{l}\\0&0&0\end{pmatrix}\begin{bmatrix}\widetilde{J}&l&J_i\\l_i&s_i&\tilde{l}\end{bmatrix}\begin{bmatrix}s_i&1&s_f\\1/2&1/2&1/2\end{bmatrix}\begin{bmatrix}l_f&1&\tilde{l}\\s_f&1&s_i\\J_f&1&\widetilde{J}\end{bmatrix}.$$

2.3.3 Radiative Transitions in Charmonium

As an illustrative example of the degree of improvement of the complete formulae with respect to the dipole ones, in Table 2.1 we list some radiative

Decay	Dipole	NR only	Complete	Data
$\psi(2S) \to \gamma\chi_{c_0}(1P)$	47	57	43	28.8 ± 1.4
$\psi(2S) \to \gamma\chi_{c_1}(1P)$	41	41	30	28.7 ± 1.5
$\psi(2S) \to \gamma\chi_{c_2}(1P)$	29	29	18	28.0 ± 1.3
$\chi_{c_0}(1P) \to \gamma J/\psi$	128	118	130	151 ± 14
$\chi_{c_1}(1P) \to \gamma J/\psi$	266	315	284	288 ± 22
$\chi_{c_2}(1P) \to \gamma J/\psi$	353	419	385	374 ± 27

Table 2.1: Radiative decay widths between charmonium states calculated within various schemes versus data. All numbers are in units of keV. The listed values are taken from Reference [56].

decay widths between charmonium states in the dipole (i.e., both LWL and NR) approximation versus NR approximation alone versus the complete result. Experimental widths are also listed for comparison. Notice that, in order to improve the comparison with data, the experimental charmonium masses and photon momenta have been implemented, instead of those obtained from the predicted spectrum, see [55, 56] for more details.

The transitions included in Table 2.1 are examples in which neither the NR or LWL approximations apply, as signaled by the differences between the calculated widths from the different schemes. The results from the complete formulae are in rather good agreement with data, with the modest residual differences that may be attributed to the neglected relativistic and spin-dependent corrections to the wave functions.[1] Moreover, the sensitivity of the results to the string tension and charm quark mass in the quarkonium potential constrains very much the values of these parameters to be about their standard phenomenological values [56].

These results indicate that a phenomenological study using the complete EM transition operator, which exploits the accurate theoretical knowledge of the EM interactions to the fullest, might function as an extremely sensitive probe of the quarkonium potential. In fact, one may use the calculated widths to discriminate between different phenomenological values of its parameters, as well as appreciate the extent of the corrections to be expected from relativistic and other spin-dependent contributions.

[1] Notice that spin corrections are expected to be more significant for $\chi_{c0}(2P)$ and $\chi_{c2}(2P)$ than for $\chi_{c1}(2P)$.

Chapter 3

Strong Decay Models

In general, the most important decay modes of a quarkonium or quarkonium hybrid meson are expected to be those to an open-flavor meson pair, if kinematically allowed. This is because, in the first place, the strong interaction is much more intense than its EM and weak counterparts and, secondly, because this kind of transitions are allowed by the Okubo-Zweig-Izuka (OZI) rule, since the corresponding Feynman diagram cannot be separated into two disconnected diagrams by the removal of the gluon lines. In this chapter we study these important decays of quarkonia and quarkonium hybrids, respectively in Sections 3.1 and 3.2, through a consistent implementation of QPC models in the BO framework. Then, in Section 3.3 we review a phenomenological application of these models.

3.1 The $^3P_0$ Model for Quarkonia

The decay of an initial quarkonium state A to a final open-flavor heavy-light meson pair BC is expected to occur from the creation of a light quark pair from the hadronic medium and their recombination with the heavy quarks, as pictured in Figure 3.1.

In BO with quenched lattice QCD potentials there is no lattice input on the light quarks dynamics, so these decays cannot be calculated *ab initio*. Instead, the transition probability may be estimated by implementing a QPC model in what may be called an "extended" BO framework. Although QPC models lack a direct connection with QCD (in this respect, the use of the diabatic formalism established in Part II should be preferred), their study is worthwhile as it provides a simple physical image of the decay that can be easily extended to quarkonium hybrids, as we shall see in the following section.

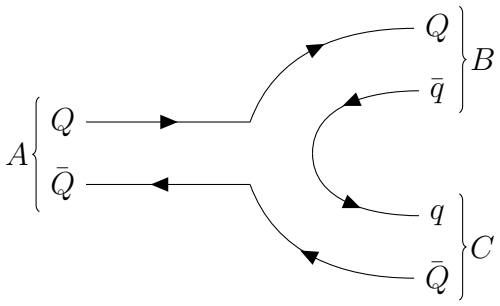

Figure 3.1: Diagram for the strong decay of a quarkonium state A into an open-flavor meson-meson state BC through the creation of a light quark pair. Gluon lines have been omitted, to show clearly that the diagram is connected.

Let us now focus on the implementation of a QPC model for the decay of an initial quarkonium meson A to a final open-flavor meson-meson pair BC. The process may be separated into two steps:

1. the emission of the light quark pair from the hadronic medium, $A \to A(q\bar{q})$;

2. the recombination of $q\bar{q}$ with the $Q\bar{Q}$ in A to form the final meson-meson pair, $A(q\bar{q}) \to BC$.

Formally, the first step may be represented as

$$\underbrace{|(l_{Q\bar{Q}}, s_{Q\bar{Q}})J_{Q\bar{Q}}, m_{J_{Q\bar{Q}}}, \Sigma_g^+\rangle}_{A} \to \underbrace{|[(l'_{Q\bar{Q}}, s'_{Q\bar{Q}})J'_{Q\bar{Q}}, (l_{q\bar{q}}, s_{q\bar{q}})J_{q\bar{q}}]J', \Sigma_g^+\rangle}_{A(q\bar{q})} \tag{3.1}$$

where, as explained in Appendix A, Σ_g^+ stands for the ground state BO configuration of the light fields, and we have introduced the parenthesis notation $(j_1, j_2)j_3$ to indicate that j_3 is the sum of j_1 and j_2. Notice that the hadronic medium of the initial quarkonium state, represented by the BO configuration Σ_g^+, has the same quantum numbers of the vacuum, $J^{PC} = 0^{++}$.

Using the symmetries of BO, the quantum numbers $l'_{Q\bar{Q}}$, $s'_{Q\bar{Q}}$, $l_{q\bar{q}}$, and $s_{q\bar{q}}$ of the intermediate state may be determined. First, let us realize that in BO with quenched lattice QCD the spin of the heavy quarks is completely decoupled from the dynamics of the gluons and light quarks (heavy-quark spin symmetry). Hence, one has $s_{Q\bar{Q}} = s'_{Q\bar{Q}}$. Moreover, from conservation of total angular momentum we have $J'_{Q\bar{Q}} = J_{Q\bar{Q}}$. Let us also remind that a quark-antiquark pair with orbital angular momentum l and total spin s has parity $P = (-1)^{l+1}$ and C-parity $C = (-1)^{l+s}$. Then, conservation of parity

in Equation (3.1) gives

$$(-1)^{l'_{Q\bar{Q}}+l_{q\bar{q}}} = (-1)^{l_{Q\bar{Q}}+1}$$

and conservation of C-parity gives

$$(-1)^{l'_{Q\bar{Q}}+l_{q\bar{q}}+s_{q\bar{q}}} = (-1)^{l_{Q\bar{Q}}},$$

which together imply $(-1)^{s_{q\bar{q}}} = -1$, this is,

$$s_{q\bar{q}} = 1.$$

To fix $l_{q\bar{q}}$, one can make the reasonable assumption that the most energetically favored emission occurs for $J_{q\bar{q}}$ taking its minimal possible value, in this case

$$J_{q\bar{q}} = 0.$$

Then one has

$$l_{q\bar{q}} = 1$$

and $l'_{Q\bar{Q}} = l_{Q\bar{Q}}$.

Therefore, by implementing a QPC model for quarkonium in an "extended" BO framework, one recovers the $^3P_0$ model extensively studied in phenomenological models. Notice, however, that in this case the quantum numbers of the emitted $q\bar{q}$ pair are fixed from the quantum numbers of the quarkonium BO configuration, under the loose assumptions of J^{PC} conservation and the transition being dominated by the smallest possible value of $J_{q\bar{q}}$.

In contrast, the symmetries of BO cannot tell us anything about how the probability of the $q\bar{q}$ emission should depend on their relative momentum $p_{q\bar{q}}$. Following what is usually done in phenomenological applications of the $^3P_0$ model, we work under the assumption that the emission probability may be given in first approximation by a constant, that we call γ_0, independent on the $q\bar{q}$ relative momentum.

As for the second step, the recombination process of $q\bar{q}$ with $Q\bar{Q}$ to form the final meson-meson state BC, it can be easily calculated using SU(2) algebra. Concretely, let $l_A = l_{Q\bar{Q}}$, l_B, and l_C be the orbital angular momenta of the initial and final mesons, respectively, $s_A = s_{Q\bar{Q}}$, s_B, and s_C their spins, and M_A, M_B, and M_C their masses. In the rest frame of A, the final mesons B and C have energy

$$E_{B,C} = \sqrt{M_{B,C}^2 + k^2}$$

with

$$k = \frac{\sqrt{(M_A^2 - (M_B + M_C)^2)(M_A^2 - (M_B - M_C)^2)}}{2M_A}$$

their momentum. Then the width for the decay $A \to BC$ is given by

$$\Gamma(A \to BC) = \gamma_0^2 2\pi \frac{E_B E_C}{M_A} k |\mathcal{M}(A \to BC)|^2,$$

where the transition matrix element may be written as

$$|\mathcal{M}(A \to BC)|^2 = \frac{1}{2\pi^2} \left(C_{I_B,I_C,0}^{\tau_B,\tau_C,0}\right)^2 \begin{bmatrix} 1/2 & 1/2 & 0 \\ 1/2 & 1/2 & 0 \\ I_B & I_C & 0 \end{bmatrix}^2 \begin{bmatrix} 1/2 & 1/2 & s_A \\ 1/2 & 1/2 & 1 \\ s_B & s_C & s_{BC} \end{bmatrix}^2$$
$$\left(\begin{bmatrix} l_A & s_A & J_A \\ 1 & 1 & 0 \\ l_A - 1 & s_{BC} & J_A \end{bmatrix}^2 |\mathcal{J}_-(k)|^2 + \begin{bmatrix} l_A & s_A & J_A \\ 1 & 1 & 0 \\ l_A + 1 & s_{BC} & J_A \end{bmatrix}^2 |\mathcal{J}_+(k)|^2 \right) \quad (3.2)$$

where we have substituted $I_A = 0$, s_{BC} is the total meson-meson spin, $I_B = I_C = 1/2$ are the isospin of B and C, respectively, and τ_B, τ_C their projections. The factors $\mathcal{J}_\pm(k)$ can be expressed as

$$\mathcal{J}_+(k) = i^{l_A} \sqrt{\frac{3(l_A+1)}{2l_A+3}} \mathcal{I}_+(k),$$
$$\mathcal{J}_-(k) = i^{l_A} \sqrt{\frac{3l_A}{2l_A-1}} \mathcal{I}_-(k),$$

where $\mathcal{I}_\pm(k)$ is the radial integral

$$\mathcal{I}_\pm(k) = \int \mathrm{d}r\, \mathrm{d}q\, u_B^*(q) u_C^*(q) u_A(r) \left(qr j_1(qr) j_{l_A \pm 1}\left(\frac{kr}{2}\right) \pm \frac{kr}{2} j_0(qr) j_{l_A}\left(\frac{kr}{2}\right) \right)$$

with $u_B(q)$ and $u_C(q)$, respectively, the reduced radial wave functions of the final mesons B and C, in momentum space, and $u_A(r)$ the reduced radial wave function of the quarkonium state A in position space.

3.2 The $^1P_1$ Model for Quarkonium Hybrids

An "extended" BO framework can also be used to study the strong decays of a quarkonium hybrid into an open-flavor heavy-light meson pair, $\mathcal{H} \to BC$. The light quark pair emission process in this case may be written as

$$|[(l_{Q\bar{Q}}, J_\Pi)\tilde{l}, s_{Q\bar{Q}}]J, m_J, \Pi_u\rangle \to |[(l'_{Q\bar{Q}}, s'_{Q\bar{Q}})J'_{Q\bar{Q}}, (l_{q\bar{q}}, s_{q\bar{q}})J_{q\bar{q}}]J', \Sigma_g^+\rangle$$

where Π_u denotes the first excited BO configuration, $J_\Pi = 1$ the total angular momentum of the light fields, and $\tilde{l} \geq 1$ an effective orbital angular momentum

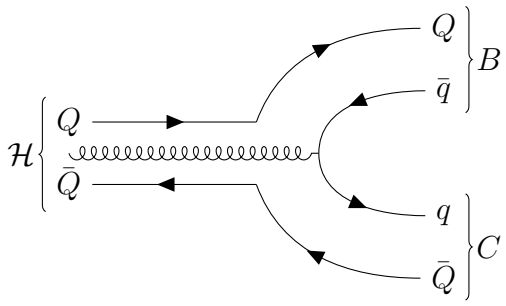

Figure 3.2: Pictorial diagram for the strong decay of a quarkonium hybrid state $\mathcal{H}$ into a open-flavor meson-meson state BC through the emission of a $q\bar{q}$ pair from the excited hadronic medium, represented as a coil-shaped line.

incorporating both the $Q\bar{Q}$ orbital angular momentum and the light field angular momentum (see Appendix A for more details). In this decomposition, it is assumed that the $q\bar{q}$ pair is emitted from the excited hadronic medium decaying into its ground state, see Figure 3.2, so the light field configuration of the intermediate state is Σ_g^+, as in the quarkonium case previously examined. Hence, the parity and C-parity of the intermediate state are the same as before, while for the initial hybrid state they are given by $P = (-1)^{\tilde{l}}$ and $C = (-1)^{\tilde{l}+s_{Q\bar{Q}}}$, respectively.

Let us now concentrate on the decays of the lowest quarkonium hybrid. Presumably, this state shall correspond to minimal values of the $\tilde{l}$ and $s_{Q\bar{Q}}$ quantum numbers, under the reasonable assumption that spin splittings in quarkonium hybrid states follow the same hierarchy of those in quarkonium states. Then we may assume $\tilde{l} = 1$ and $s_{Q\bar{Q}} = 0$, meaning that for the lowest hybrid state we expect $J^{PC} = 1^{--}$, and consequently we have

$$(-1)^{l'_{Q\bar{Q}}+l_{q\bar{q}}} = -1, \qquad \text{and} \qquad (-1)^{l'_{Q\bar{Q}}+l_{q\bar{q}}+s_{q\bar{q}}} = -1$$

from conservation of parity and C-parity, respectively. Comparing the two expressions above, we get $(-1)^{s_{q\bar{q}}} = 1$ and hence

$$s_{q\bar{q}} = 0.$$

Using $\tilde{l} = 1$, $s_{Q\bar{Q}} = s_{q\bar{q}} = 0$, conservation of total angular momentum reads $l'_{Q\bar{Q}} + l_{q\bar{q}} = 1$. Moreover, it can be shown that, since the $q\bar{q}$ is emitted from the excited Π_u configuration, one also has $J_{q\bar{q}} = l_{q\bar{q}} \geq 1$. Then,assuming that the decay is dominated by the lowest possible value of $J_{q\bar{q}}$, we have

$$J_{q\bar{q}} = l_{q\bar{q}} = 1$$

and $l'_{Q\bar{Q}} = 0$.

Thus, the quantum numbers of the QPC decay model for the lowest quarkonium hybrid are $^1P_1$. This results constitutes a major difference with respect to the $^3P_0$ decay model obtained in quarkonium, and it can be regarded as its natural generalization to the lowest hybrid state within an "extended" BO framework. Notice that the quantum numbers of the emitted $q\bar{q}$ pair are those of the ground gluelump state, $J^{PC} = 1^{+-}$.

As for the recombination process, the calculation is done in exactly the same manner as in the quarkonium case. The width for the strong decay of the lowest quarkonium hybrid may then be written as

$$\Gamma(\mathcal{H} \to BC) = \gamma_1^2 2\pi \frac{E_B E_C}{M_{\mathcal{H}}} k |\mathcal{M}(\mathcal{H} \to BC)|^2,$$

where, analogously to γ_0 in the quarkonium case, we have defined a constant γ_1 for the probability of a $q\bar{q}$ pair being created from the excited hadronic medium. The transition matrix element is now given by

$$|\mathcal{M}(\mathcal{H} \to BC)|^2 = \frac{1}{2\pi^2} \left(C^{\tau_B,\tau_C,0}_{I_B,I_C,0}\right)^2 \begin{bmatrix} 1/2 & 1/2 & 0 \\ 1/2 & 1/2 & 0 \\ I_B & I_C & 0 \end{bmatrix}^2 \begin{bmatrix} 1/2 & 1/2 & 0 \\ 1/2 & 1/2 & 0 \\ s_B & s_C & s_{BC} \end{bmatrix}^2 \begin{bmatrix} 0 & 0 & 0 \\ 1 & 0 & 1 \\ 1 & s_{BC} & 1 \end{bmatrix}^2 |\mathcal{I}_+(k)|^2 \quad (3.3)$$

with

$$\mathcal{I}_+(k) = \int \mathrm{d}r\, \mathrm{d}q\, u_B^*(q) u_C^*(q) u_{\mathcal{H}}(r) \left(qr j_1(qr) j_1\left(\frac{kr}{2}\right) + \frac{kr}{2} j_0(qr) j_0\left(\frac{kr}{2}\right)\right)$$

where $u_{\mathcal{H}}(r)$ is the reduced radial wave function of the hybrid state in position space, and we have taken into account that $l'_{Q\bar{Q}} = 0$, $l_{q\bar{q}} = 1$, and $s_{Q\bar{Q}} = s_{q\bar{q}} = 0$.

The crucial difference between Equation (3.3) and the corresponding one for quarkonium, Equation (3.2), is the appearance of a new spin selection rule for the strong decay of the lowest quarkonium hybrid to an open-flavor meson-meson pair. In fact, the Wigner 9j-symbols vanish if any of its rows or columns does not satisfy the triangular rule. Then, one has that strong decays to meson-meson states with $s_{BC} \neq 0$ are forbidden.

The spin selection rule $s_{BC} = 0$ is a direct consequence of $s_{q\bar{q}} = 0$ from the QPC decay model, which is fixed by the symmetries of BO. It is worth to point out that this selection rule is different from the one obtained in constituent models of hybrids, see, for instance, [75, 76] and references therein.

In these models the $q\bar{q}$ pair is assumed to have the quantum numbers 1^{--} of a free gluon, instead of the gluelump quantum numbers of the hadronic medium in the hybrid. Our derived selection rule implies that, for example, the lowest bottomonium hybrid is not expected to decay to $B\bar{B}^*$, which could constitute a distinctive signature for its experimental discovery. Let us note, however, that this hybrid is expected to mix with quarkonium states with the same $J^{PC} = 1^{--}$ quantum numbers and a similar mass.

3.3 The Lowest Bottomonium Hybrid and $\Upsilon(10860)$

The calculated mass of the lowest bottomonium hybrid $\mathcal{H}_b(1P)$, 10855.2 MeV, is extremely close to that of the $\Upsilon(5S)$ bottomonium state, 10856.5 MeV, and both of them are close to the peak of the experimental $\Upsilon(10860)$ resonance at $10885.2^{+2.6}_{-1.6}$ MeV. Hence, we may try to establish the nature of $\Upsilon(10860)$ as either a bottomonium, hybrid, or mixed state using the decay widths to open-bottom calculated within the "extended" BO framework developed in this chapter.

In the remaining of this section, we shall discuss the values calculated in [58]. They were calculated in the same QPC decay models detailed here, but the parameters of the underlying bottomonium and hybrid potentials, namely the string tension σ and bottom quark mass m_b, were different from the ones used in this thesis. However, as no qualitative difference is expected in the results if the current values of σ and m_b were used, we may review the results of Reference [58] to appreciate the usefulness of the "extended" BO framework.

Since in both QPC models there is an arbitrary constant, γ_0 and γ_1, respectively, for $^3P_0$ and $^1P_1$, it is more useful to study ratios of decay widths rather than the widths themselves. Then, for the experimental $\Upsilon(10860)$ one has

$$\frac{\Gamma_{\Upsilon(10860)\to B\bar{B}}}{\Gamma_{\Upsilon(10860)\to B\bar{B}^*}} = 0.40 \pm 0.12, \quad \frac{\Gamma_{\Upsilon(10860)\to B^*\bar{B}^*}}{\Gamma_{\Upsilon(10860)\to B\bar{B}^*}} = 2.8 \pm 0.8,$$

and

$$\frac{\Gamma_{\Upsilon(10860)\to B_s^*\bar{B}_s^*}}{\Gamma_{\Upsilon(10860)\to B_s\bar{B}_s^*}} = 13 \pm 5.$$

On the other hand, for $\Upsilon(5S)$ the $^3P_0$ model predicts

$$\frac{\Gamma_{\Upsilon(5S)\to B\bar{B}}}{\Gamma_{\Upsilon(5S)\to B\bar{B}^*}} = 0.4, \quad \frac{\Gamma_{\Upsilon(5S)\to B^*\bar{B}^*}}{\Gamma_{\Upsilon(5S)\to B\bar{B}^*}} = 0.3, \quad \text{and} \quad \frac{\Gamma_{\Upsilon(5S)\to B_s^*\bar{B}_s^*}}{\Gamma_{\Upsilon(5S)\to B_s\bar{B}_s^*}} = 0.2.$$

These values support an assignment of $\Upsilon(10860)$ different than the $5S$ quarkonium state. However, it cannot be assigned to the hybrid $\mathcal{H}_b(1P)$, either. In fact, as mentioned before, the spin selection rule of the $^1P_1$ model implies

$$\Gamma_{\mathcal{H}_b(1P)\to B\bar{B}^*} = 0 \quad \text{and} \quad \Gamma_{\mathcal{H}_b(1P)\to B_s\bar{B}_s^*} = 0,$$

which is clearly incompatible with the observed branching fractions of $13.7 \pm 1.6\%$ and $1.35 \pm 0.32\%$ for $\Upsilon(10860) \to B\bar{B}^*$ and $\Upsilon(10860) \to B_s\bar{B}_s^*$, respectively.

As an alternative, one may consider the $\Upsilon(10860)$ as being a mixture of bottomonium and bottomonium hybrid components,

$$|\Upsilon(10860)\rangle = \cos\vartheta\,|\Upsilon(5S)\rangle + \sin\vartheta\,|\mathcal{H}_b(1P)\rangle$$

with ϑ the mixing angle. Then, using the "extended" BO framework it is possible to show that a small hybrid component, $\sin^2\vartheta \lesssim 0.1$, could be sufficient to explain the observed decay width ratios of $\Upsilon(10860)$ to open-bottom meson-meson. It has also been shown that a small hybrid component in $\Upsilon(10860)$ may serve to explain its observed dipion and dilepton decay widths [57]. Moreover, in this mixing scenario, the predicted orthogonal state,

$$|\mathcal{H}(10860)\rangle = -\sin\vartheta\,|\Upsilon(5S)\rangle + \cos\vartheta\,|\mathcal{H}_b(1P)\rangle\,,$$

which is dominated by the hybrid component, is expected to have a total width to open-bottom of several hundreds of MeV at least. This would make it very difficult to disentangle the corresponding peak from data, which may justify its lack of detection to date. We refer the interested reader to [57, 58] for further details.

Part II

The Diabatic Approach

Chapter 4

String Breaking in Heavy-Quark Systems

The single channel BO approximation relies on the fundamental assumption that the coupling between different adiabatic energy levels is negligible or, at least, has no overlap with the adiabatic wave functions. For quarkonium states with quenched lattice QCD potentials, as seen in Chapter 1, this may be deemed a good approximation. However, the situation changes dramatically when the quenched approximation is lifted. In this chapter, we adapt the diabatic framework, first introduced in molecular physics, to the study of heavy-quark systems made of quark-antiquark and meson-meson components. Concretely, in Section 4.1, we consider the breaking of the adiabatic approximation and introduce the diabatic expansion. The Schrödinger equation in the diabatic representation is derived Section 4.2. Then, in Section 4.3 we connect the diabatic potential with unquenched lattice results.

4.1 String Breaking and the Diabatic Expansion

Recent exploratory studies of the static energy levels in unquenched lattice QCD [15, 17] show that as the energy level corresponding to a quark-antiquark configuration, $V_{Q\bar{Q}}$, approaches the threshold mass T_1 of an open-flavor meson-meson one, a mixing between the two configurations takes place. This phenomenon, depicted in Figure 4.1, is known as *adiabatic surface mixing* or *avoided crossing*, and it clearly breaks the single channel approximation.

The adiabatic surface mixing calculated in unquenched lattice QCD is an expected consequence of having introduced sea quarks in the calculation of the static energy levels. In fact, References [15, 17] constitute the first

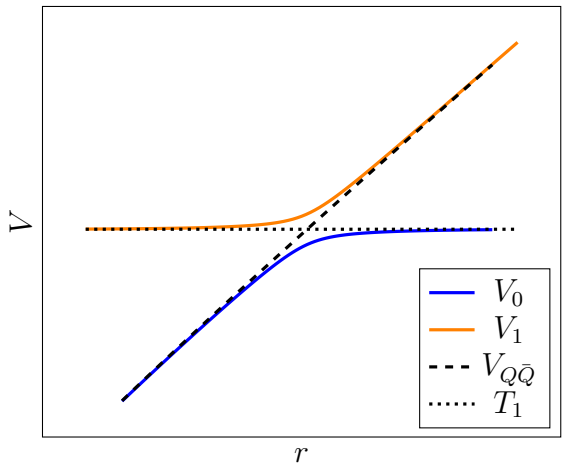

Figure 4.1: Pictorial representation of the ground and first excited radial potentials in unquenched lattice QCD, versus the quark-antiquark static energy $V_{Q\bar{Q}}$ and the meson-meson threshold mass T_1.

observations in lattice QCD of the mixing between quarkonium and meson-meson states depicted in Figure 3.1. In this context, the physical mechanism underlying this mixing is referred to as *string breaking*. From a static point of view, it may be pictured as follows:

1. Because of the confining interaction, as the distance between Q and $\bar{Q}$ increases, so does their static energy.

2. As the $Q\bar{Q}$ energy approaches a meson-meson threshold T_1, creation of light quark pairs $q\bar{q}$ from the sea becomes more probable.

3. The light fields may adjust into a static meson-meson configuration in place of a $Q\bar{Q}$ one.

Pictorially, one may imagine this process as if the heavy quark and antiquark were connected by an elastic string which may break with the creation of a light quark-antiquark pair from the sea, see Figure 4.2.

As a consequence of string breaking, the NACTs in the Schrödinger-like equation (1.7) cannot be neglected, and one should solve the complete system of coupled equations. However, this is unpractical for at least two reasons: first, the connection between the NACTs and lattice QCD calculations is not straightforward, second, the adiabatic wave function components would not be associated to a well-defined configuration, but rather to a mixing of $Q\bar{Q}$ and meson-meson where the amount of the mixing depends on $\boldsymbol{r}$.

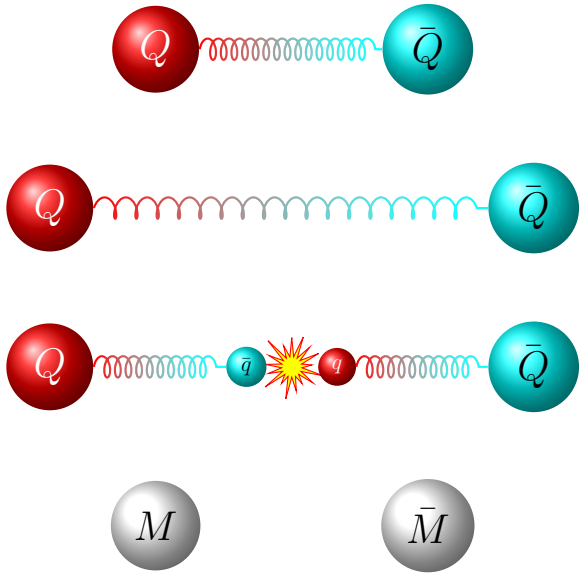

Figure 4.2: Pictorial representation of the mixing induced by string breaking. From top to bottom: the $Q\bar{Q}$ are connected by an elastic string; the string stretches as the $Q\bar{Q}$ distance increases; the string breaks with the creation of a light $q\bar{q}$ pair; an open-flavor meson-meson pair is formed.

These difficulties may be easily averted by using, instead of the adiabatic expansion (1.3), a *diabatic expansion* for the heavy-quark meson state:

$$|\psi\rangle = \sum_j \int \mathrm{d}\boldsymbol{r}' \widetilde{\psi}_j(\boldsymbol{r}', \boldsymbol{r}_0) \, |\boldsymbol{r}'\rangle \, |\zeta_j(\boldsymbol{r}_0)\rangle \, . \tag{4.1}$$

By comparison with Equation (1.3), one can see that the diabatic expansion differs from its adiabatic counterpart in that the light field states are calculated at a fixed position $\boldsymbol{r}_0$, instead of the position $\boldsymbol{r}$ of the heavy degrees of freedom. This crucial difference makes so that the light field configuration associated to each wave function component $\widetilde{\psi}_j$ does not change with $\boldsymbol{r}$. In this sense, fixing $\boldsymbol{r}_0$ is equivalent to fixing the light-field basis for the expansion of the heavy-quark meson state.

Plugging Equation (4.1) into Equation (1.1) and multiplying on the left with $\langle\zeta_i(\boldsymbol{r}_0)|$ gives

$$\sum_j \left(-\frac{\nabla^2}{2\mu}\delta_{ij} + V_{ij}(\boldsymbol{r}, \boldsymbol{r}_0) - E\delta_{ij} \right) \widetilde{\psi}_j(\boldsymbol{r}, \boldsymbol{r}_0) = 0, \tag{4.2}$$

this is, a multichannel Schrödinger equation where the dynamics is governed

by a *diabatic potential matrix* defined as

$$V_{ij}(\boldsymbol{r}, \boldsymbol{r}_0) = \langle \zeta_i(\boldsymbol{r}_0) | H^{\text{static}}_{\text{light}}(\boldsymbol{r}) | \zeta_j(\boldsymbol{r}_0) \rangle \,. \tag{4.3}$$

The diabatic potential matrix enjoys a direct connection with the adiabatic potentials that can be calculated in lattice QCD. To see this, let us introduce the unitary adiabatic-to-diabatic transition (ADT) matrix, defined as

$$A_{ij}(\boldsymbol{r}, \boldsymbol{r}_0) = \langle \zeta_i(\boldsymbol{r}) | \zeta_j(\boldsymbol{r}_0) \rangle \,.$$

From the expansions (1.3) and (4.1), it can be easily checked that the ADT matrix can be used to express the adiabatic wave function in terms of the diabatic one,

$$\psi_i(\boldsymbol{r}) = \sum_j A_{ij}(\boldsymbol{r}, \boldsymbol{r}_0) \widetilde{\psi}_j(\boldsymbol{r}, \boldsymbol{r}_0),$$

which can be substituted in (1.7) to obtain

$$\sum_{jj'} \left(-\frac{1}{2\mu} [(I\boldsymbol{\nabla} + \boldsymbol{\tau}(\boldsymbol{r}))^2]_{i'j'} + \delta_{i'j'}(V_{i'}(\boldsymbol{r}) - E) \right) A_{j'j}(\boldsymbol{r}, \boldsymbol{r}_0) \widetilde{\psi}_j(\boldsymbol{r}, \boldsymbol{r}_0) = 0.$$

Then, multiplying the above expression on the left by $A^\dagger_{ii'}$ and summing over i' yields

$$\sum_j \Bigg(-\frac{1}{2\mu} [A^\dagger(\boldsymbol{r}, \boldsymbol{r}_0)(I\boldsymbol{\nabla} + \boldsymbol{\tau}(\boldsymbol{r}))^2 A(\boldsymbol{r}, \boldsymbol{r}_0)]_{ij} + \sum_{j'} A^\dagger_{ij'}(\boldsymbol{r}, \boldsymbol{r}_0) V_{j'}(\boldsymbol{r}) A_{j'j}(\boldsymbol{r}, \boldsymbol{r}_0) \Bigg) \widetilde{\psi}_j(\boldsymbol{r}, \boldsymbol{r}_0) = 0. \tag{4.4}$$

Finally, by direct comparison of Equation (4.4) with Equation (4.2), one obtains

$$[A^\dagger(\boldsymbol{r}, \boldsymbol{r}_0)(I\boldsymbol{\nabla} + \boldsymbol{\tau}(\boldsymbol{r}))^2 A(\boldsymbol{r}, \boldsymbol{r}_0)]_{ij} = \delta_{ij} \nabla^2 \tag{4.5}$$

and

$$\sum_{j'} A^\dagger_{ij'}(\boldsymbol{r}, \boldsymbol{r}_0) V_{j'}(\boldsymbol{r}) A_{j'j}(\boldsymbol{r}, \boldsymbol{r}_0) = V_{ij}(\boldsymbol{r}, \boldsymbol{r}_0). \tag{4.6}$$

Equation (4.5) can be rearranged in the form of a differential equation relating the ADT matrix and the NACTs, which is of no particular interest to the current analysis.[1] We focus instead on Equation (4.6), which connects the

[1] We refer the interested reader to [65] for more details.

diabatic potential matrix to the adiabatic potentials and the ADT matrix. This useful relation can be inverted as

$$[A(\boldsymbol{r},\boldsymbol{r}_0)V(\boldsymbol{r},\boldsymbol{r}_0)A^\dagger(\boldsymbol{r},\boldsymbol{r}_0)]_{ij} = V_i(\boldsymbol{r})\delta_{ij},$$

showing that the ADT matrix diagonalizes the diabatic potential matrix and that the eigenvalues of the diabatic potential matrix are the adiabatic potentials that can be calculated in lattice QCD.

4.2 The Diabatic Schrödinger Equation

Let us now examine in more detail how the diabatic potential matrix may be inferred from the energy levels calculated in quenched and unquenched lattice QCD. To do so, let us realize that the correspondence between the diabatic and adiabatic representations outlined above can be only approximate when $Q\bar{Q}$ mix with meson-meson. There are two reasons for this. On the one hand, the meson-meson reduced mass is different from the heavy quark-antiquark one. On the other hand, the spin-orbital quantum numbers of a meson-meson pair may be different from those of a quark-antiquark pair, hence the diabatic potential cannot be in general neither spherically symmetric nor spin-independent, unlike the quenched lattice QCD potentials. However, as we shall see in the remaining of this chapter, a radial diabatic potential matrix may still be defined. This allows to draw a correspondence between the diabatic potential matrix and lattice QCD data on string breaking.

Let us concentrate on a heavy-quark meson system made of $Q\bar{Q}$ mixing with N open-flavor meson-meson components $M_1^i\bar{M}_2^i$ with $i = 1, 2, \ldots, N$. Let us also fix the coordinate $\boldsymbol{r}_0$ in the diabatic expansion (4.1) to some value far from the string breaking region, so that we may identify $|\zeta_0(\boldsymbol{r}_0)\rangle = |Q\bar{Q}\rangle$ and $|\zeta_i(\boldsymbol{r}_0)\rangle = |M_1^i\bar{M}_2^i\rangle$. Then the diabatic Schrödinger equation may be written formally as

$$(K+V)\,|\Psi\rangle = E\,|\Psi\rangle \tag{4.7}$$

where K is the kinetic energy operator, V the diabatic potential operator, and $|\Psi\rangle$ the heavy-quark meson state, represented as a column vector

$$|\Psi\rangle = \begin{pmatrix} |\psi_0\rangle \\ |\psi_1\rangle \\ \vdots \\ |\psi_N\rangle \end{pmatrix}$$

with $|\psi_0\rangle$ and $|\psi_i\rangle$ the state of the $Q\bar{Q}$ and $M_1^i\bar{M}_2^i$ component, respectively.

To write explicitly the kinetic energy operator, let us realize that the mass m_M of any open-flavor meson may be expressed as $m_M = m_Q + c$, where m_Q is the mass of the heavy quark and c may be assumed to be well-behaved in the limit $m_Q \to \infty$. Then, for $c/m_Q \ll 1$, as it is the case for all known charmed and bottom mesons [70], the center of mass of $M_1^i \bar{M}_2^i$ practically coincides with that of $Q\bar{Q}$, and the kinetic energy operator in the center-of-mass reference frame may be expressed as

$$K = \begin{pmatrix} \frac{p^2}{2\mu_0} & & & \\ & \frac{p^2}{2\mu_1} & & \\ & & \ddots & \\ & & & \frac{p^2}{2\mu_N} \end{pmatrix}$$

where $\mu_0 = m_Q/2$ is the $Q\bar{Q}$ reduced mass,

$$\mu_i = \frac{m_{M_1^i} m_{\bar{M}_2^i}}{m_{M_1^i} + m_{\bar{M}_2^i}}$$

that of $M_1^i \bar{M}_2^i$, p^2 is the squared relative momentum operator, and we have omitted vanishing matrix elements, for simplicity. It is important to notice that this form of the kinetic energy operator may be expanded in powers of $1/m_Q$ as

$$K = I\frac{p^2}{m_Q} + \mathcal{O}(m_Q^{-2}),$$

hence, at leading order it coincides with the kinetic energy term of Equation (4.2).

As for the diabatic potential operator, we write it in the general form

$$V = \begin{pmatrix} V_{00} & V_{01} & \dots & V_{0N} \\ V_{01}^\dagger & V_{11} & & \\ \vdots & & \ddots & \\ V_{01}^\dagger & & & V_{NN} \end{pmatrix}$$

where V_{00}, V_{ii}, and V_{0i} are, respectively, the potential operators associated to $Q\bar{Q}$, $M_1^i \bar{M}_2^i$, and the mixing between them. Notice that in writing this expression we have assumed that direct mixing between different meson-meson components is negligible, i.e., $V_{ij} = 0$ for $i \neq j$.

Equation (4.7) may be projected onto coordinate space using

$$\int \mathrm{d}\boldsymbol{r}' \, \langle \boldsymbol{r}|K + V|\boldsymbol{r}'\rangle \, \langle \boldsymbol{r}'|\Psi\rangle = E \, \langle \boldsymbol{r}|\Psi\rangle \,,$$

and the wave function $\Psi(\boldsymbol{r}) = \langle \boldsymbol{r}|\Psi\rangle$ reads

$$\Psi(\boldsymbol{r}) = \begin{pmatrix} \psi_0(\boldsymbol{r}) \\ \psi_1(\boldsymbol{r}) \\ \vdots \\ \psi_N(\boldsymbol{r}) \end{pmatrix}$$

where $\psi_0(\boldsymbol{r}) = \langle \boldsymbol{r}|\psi_0\rangle$ and $\psi_i(\boldsymbol{r}) = \langle \boldsymbol{r}|\psi_i\rangle$ are the wave function components.

Notice that at this stage we have not projected explicitly on spin space, hence each wave function component must be intended as a spin vector. Concretely, we impose J^{PC} conservation, following the symmetries of QCD, so that each solution to (4.7) must possess definite J^{PC} quantum numbers. Therefore, it is natural to express each wave function component in terms of a radial wave function times a spin-orbital one:

$$\psi_0^{m_J}(\boldsymbol{r}) = \sum_t R_0^t(r)\mathcal{Y}^{m_J}_{l_0^t,s_0^t,J}(\hat{\boldsymbol{r}}) \tag{4.8a}$$

$$\psi_i^{m_J}(\boldsymbol{r}) = \sum_k R_i^k(r)\mathcal{Y}^{m_J}_{l_i^k,s_i^k}(\hat{\boldsymbol{r}}) \tag{4.8b}$$

where t and k are used, respectively, to label the different (l_0, s_0) and (l_i, s_i) partial waves contributing to the given J^{PC}, while the J^{PC} label has been omitted from the wave function components, for simplicity, in the understanding that it is always implicit. The definition of the spin-orbital wave functions $\mathcal{Y}^{m_J}_{l,s,J}(\hat{\boldsymbol{r}})$ for the $M_1^i\bar{M}_2^i$ component is given by Equation (1.15) with the formal substitutions $Q \to M_1^i$ and $\bar{Q} \to \bar{M}_2^i$.

It is worth recalling that the parity and C-parity of a $Q\bar{Q}$ pair in a (l_0, s_0) partial wave are given by

$$P = (-1)^{l_0+1} \qquad \text{and} \qquad C = (-1)^{l_0+s_0},$$

respectively. As for the meson-meson components, we have

$$P = P_{M_1^i}P_{\bar{M}_2^i}(-1)^{l_i}$$

with P_M the intrinsic parity of the open-flavor meson, while C-parity is well-defined only if $\bar{M}_2^i$ is the antiparticle of M_1^i, i.e., $\bar{M}_2^i \equiv \bar{M}_1^i$, in which case it is given by

$$C = (-1)^{l_i+s_i}.$$

If otherwise $\bar{M}_2^i \not\equiv \bar{M}_1^i$, both positive and negative C-parity meson-meson configurations may be constructed,

$$C\,|M_1^i\bar{M}_2^i\rangle_\pm = \pm\,|M_1^i\bar{M}_2^i\rangle\,,$$

Table 4.1: Quark-antiquark (l_0, s_0) and meson-meson (l_i, s_i) partial waves coupling to some J^{PC}. M and M^* stand, respectively, for a pseudoscalar and vector open-flavor meson.

J^{PC}	$Q\bar{Q}$	$M\bar{M}$	$M\bar{M}^*$	$M^*\bar{M}^*$
0^{++}	$(1,1)$	$(0,0)$		$(0,0),(2,2)$
1^{++}	$(1,1)$		$(0,1),(2,1)$	$(2,2)$
2^{++}	$(1,1),(3,1)$	$(2,0)$	$(2,1)$	$(0,2),(2,0),(2,2),(4,2)$
1^{--}	$(0,1),(2,1)$	$(1,0)$	$(1,1)$	$(1,0),(1,2),(3,2)$

with

$$|M_1^i \bar{M}_2^i\rangle_\pm = \frac{1}{\sqrt{2}}\big(|M_1^i \bar{M}_2^i\rangle \pm \mathcal{C}\,|\bar{M}_1^i M_2^i\rangle\big)$$

and

$$\mathcal{C} = (-1)^{l_i + s_i + l_{M_1^i} + l_{\bar{M}_2^i} + s_{M_1^i} + s_{\bar{M}_2^i} + J_{M_1^i} + J_{\bar{M}_2^i}}.$$

Henceforth, it will be implicitly understood that we deal exclusively with meson-meson configurations with definite C-parity. So, for example, we may write $B\bar{B}^*$ as a shorthand notation for the $|B\bar{B}^*\rangle_\pm$ configuration (with the opportune C-parity, depending on the context), not to be confused with $|B\bar{B}^*\rangle$. The list of partial waves coupling to $J^{PC} = (0,1,2)^{++}$ and $J^{PC} = 1^{--}$ is given in Table 4.1, for completeness.

In position space, the kinetic energy operator is represented by the usual kernel

$$\langle \boldsymbol{r}|K|\boldsymbol{r}'\rangle = \delta(\boldsymbol{r}' - \boldsymbol{r}) \begin{pmatrix} -\frac{\nabla^2}{2\mu_0} & & & \\ & -\frac{\nabla^2}{2\mu_1} & & \\ & & \ddots & \\ & & & -\frac{\nabla^2}{2\mu_N} \end{pmatrix}.$$

As for the diagonal terms of the diabatic potential operator, one may safely assume that up to order $1/m_Q$ they are represented by spherical, spin-independent potentials

$$V_{00} = \delta(\boldsymbol{r}' - \boldsymbol{r}) V_{00}(r),$$
$$V_{11} = \delta(\boldsymbol{r}' - \boldsymbol{r}) V_{11}(r).$$

The kernel of the offdiagonal terms V_{0i}, on the other hand, is slightly more involved. As mentioned at the beginning of this section, string breaking may couple quark-antiquark and meson-meson components with different orbital

and spin quantum numbers. Hence, one should not assume the potential to be spherically symmetric or spin-independent. However, utilizing J^{PC} conservation it is possible to expand the kernel of the mixing potential operator as

$$\langle \boldsymbol{r}|V_{0i}|\boldsymbol{r}'\rangle = \delta(r'-r)V_{0i}(r)\sum_{J^{PC},m_J}\sum_{t',k'}\mathcal{Y}^{m_J}_{l_0^{t'},s_0^{t'},J}(\hat{\boldsymbol{r}})\mathcal{Y}^{m_J\dagger}_{l_i^{k'},s_i^{k'},J}(\hat{\boldsymbol{r}}'). \tag{4.9}$$

In the most general case, each partial-wave mixing, characterized by J^{PC}, l_0, s_0, l_i, and s_i, may possess its own independent radial potential. However, in writing Equation (4.9) we have made the simplifying assumption that the same radial potential applies to each partial-wave mixing. Notice also that time reversal invariance requires $V_{0i}(r)$ be a real function, $V_{0i}(r) = V^*_{0i}(r)$.

4.3 Quark-Antiquark–Meson-Meson Mixing

To show explicitly how the quark-antiquark–meson-meson mixing potential may be determined from lattice QCD studies of string breaking, let us consider the simplest possible example of a single $Q\bar{Q}$ partial wave coupling to only one meson-meson partial wave with the same J^{PC}. In this example we may suppress the redundant indices t and k, and simply write

$$\psi_0^{m_J}(\boldsymbol{r}) = R_0(r)\mathcal{Y}^{m_J}_{l_0,s_0,J}(\hat{\boldsymbol{r}})$$
$$\psi_1^{m_J}(\boldsymbol{r}) = R_1(r)\mathcal{Y}^{m_J}_{l_1,s_1,J}(\hat{\boldsymbol{r}})$$

for the wave function components and

$$\langle \boldsymbol{r}|V_{01}|\boldsymbol{r}'\rangle = \delta(r'-r)V_{01}(r)\mathcal{Y}^{m_J}_{l_0,s_0,J}(\hat{\boldsymbol{r}})\mathcal{Y}^{m_J\dagger}_{l_1,s_1,J}(\hat{\boldsymbol{r}}').$$

for the mixing potential. If we substitute these expressions back into Equation (4.7) we obtain, in position space,

$$\begin{cases}\left(-\dfrac{\nabla^2}{2\mu_0}+V_{00}(r)-E\right)\psi_0^{m_J}(\boldsymbol{r})+V_{01}(r)R_1(r)\mathcal{Y}^{m_J}_{l_0,s_0,J}(\hat{\boldsymbol{r}})=0\\ \left(-\dfrac{\nabla^2}{2\mu_1}+V_{11}(r)-E\right)\psi_1^{m_J}(\boldsymbol{r})+V_{01}(r)R_0(r)\mathcal{Y}^{m_J}_{l_1,s_1,J}(\hat{\boldsymbol{r}})=0,\end{cases}$$

where we have used the orthogonality relation (1.16). This system can be cast as a multichannel radial Schrödinger equation in the form

$$\left[\begin{pmatrix}-\frac{1}{2\mu_0}\frac{\mathrm{d}^2}{\mathrm{d}r^2}+\frac{l_0(l_0+1)}{2\mu_0 r^2} & \\ & -\frac{1}{2\mu_1}\frac{\mathrm{d}^2}{\mathrm{d}r^2}+\frac{l_1(l_1+1)}{2\mu_1 r^2}\end{pmatrix}+\begin{pmatrix}V_{00}(r) & V_{01}(r)\\ V_{01}(r) & V_{11}(r)\end{pmatrix}-E\right]\begin{pmatrix}u_0(r)\\ u_1(r)\end{pmatrix}=0 \tag{4.10}$$

with $u_0(r) = rR_0(r)$ and $u_1(r) = rR_1(r)$ the reduced radial wave functions. Notice that each partial wave is treated as an independent channel in the radial Schrödinger equation. It is also important to realize that the second term inside square brackets in Equation (4.10),

$$V(r) = \begin{pmatrix} V_{00}(r) & V_{01}(r) \\ V_{01}(r) & V_{11}(r) \end{pmatrix}, \tag{4.11}$$

is a radial multichannel potential that can be interpreted as a radial diabatic potential matrix. This can be put in correspondence with the adiabatic potentials calculated in unquenched lattice QCD through a radial ADT matrix. In this example, the radial ADT matrix can be written in general as a rotation matrix:

$$A(r) = \begin{pmatrix} \cos\theta(r) & \sin\theta(r) \\ -\sin\theta(r) & \cos\theta(r) \end{pmatrix}$$

where $\theta(r)$, the mixing angle between $Q\bar{Q}$ and meson-meson configurations in the light field eigenstates, has also been calculated in unquenched lattice QCD [15]. Then, the radial diabatic potential matrix can be obtained from the unquenched potentials and the mixing angle using Equation (4.6), which gives

$$V(r) = \begin{pmatrix} \cos\theta(r) & -\sin\theta(r) \\ \sin\theta(r) & \cos\theta(r) \end{pmatrix} \begin{pmatrix} \tilde{V}_0(r) & \\ & \tilde{V}_1(r) \end{pmatrix} \begin{pmatrix} \cos\theta(r) & \sin\theta(r) \\ -\sin\theta(r) & \cos\theta(r) \end{pmatrix}$$

where, in order to avoid any possible confusion, we have renamed the ground and first excited state adiabatic potentials as $\tilde{V}_0(r)$ and $\tilde{V}_1(r)$, respectively. Explicitly, the diabatic potential matrix elements are given as

$$V_{00}(r) = \frac{\tilde{V}_0(r) + \tilde{V}_1(r)}{2} - \frac{\tilde{V}_1(r) - \tilde{V}_0(r)}{2}\cos 2\theta(r), \tag{4.12}$$

$$V_{11}(r) = \frac{\tilde{V}_0(r) + \tilde{V}_1(r)}{2} + \frac{\tilde{V}_1(r) - \tilde{V}_0(r)}{2}\cos 2\theta(r), \tag{4.13}$$

$$V_{01}(r) = -\frac{\tilde{V}_1(r) - \tilde{V}_0(r)}{2}\sin 2\theta(r). \tag{4.14}$$

The adiabatic potentials, $\tilde{V}_0(r)$ and $\tilde{V}_1(r)$, and the mixing angle, $\theta(r)$, have been calculated in unquenched lattice QCD when $Q\bar{Q}$ mixes with one meson-meson configuration [15]. Their behavior near the avoided crossing is graphically represented in Figures 4.1 and 4.3.

The analysis of the diagonal elements $V_{00}(r)$ and $V_{11}(r)$ though Equations (4.12) and (4.13) gives no new physical insight. In fact, $V_{00}(r)$, corresponding to the static potential of $Q\bar{Q}$ in absence of mixing, behaves like

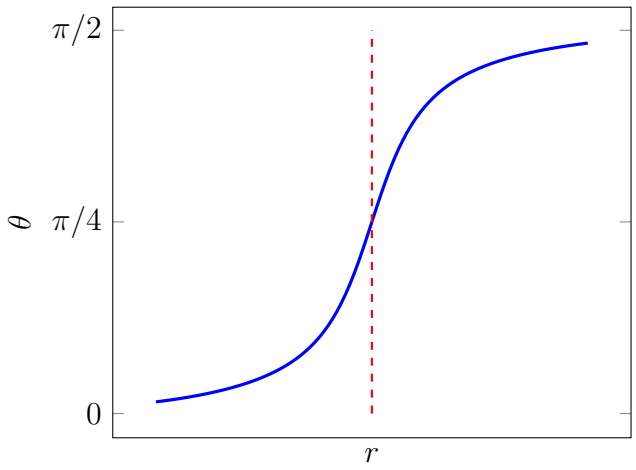

Figure 4.3: Pictorial representation of the mixing angle $\theta(r)$ in unquenched lattice QCD. The avoided crossing radius is highlighted by the dashed vertical line.

the ground state quenched lattice QCD potential [22] already examined in Section 1.2.1. We therefore identify it with the quarkonium potential,

$$V_{00}(r) = V_{\mathrm{C}}(r)$$

where the Cornell potential $V_{\mathrm{C}}(r)$ is given in Equation (1.10). As for $V_{11}(r)$, this is, the static meson-meson energy in absence of mixing, it is very close to the meson-meson threshold mass $T_1 = m_{M_1^1} + m_{\bar{M}_2^1}$, just as expected.[2] So we have

$$V_{11}(r) = T_1. \tag{4.15}$$

On the contrary, it is quite revealing to study the behavior of the mixing potential $V_{01}(r)$ from Equation (4.14) and unquenched lattice QCD data. Concretely, one can see from Figure 4.3 that $\sin 2\theta(r)$ may be different from zero only in the vicinity of the avoided crossing, since for smaller (larger) distances we have $\theta(r) \approx 0\,(\pi/2)$. Moreover, at the avoided crossing radius r_1^{c}, defined as the distance where $V_{\mathrm{C}}(r_1^{\mathrm{c}}) = T_1$, we have $\sin 2\theta(r_1^{\mathrm{c}}) \approx 1$. Therefore, the mixing potential approaches an absolute minimum $V_{01}(r_1^{\mathrm{c}}) = -\Delta/2$, where $\Delta = \tilde{V}_1(r_1^{\mathrm{c}}) - \tilde{V}_0(r_1^{\mathrm{c}})$ is the energy gap between the ground and first excited adiabatic potentials at the avoided crossing. Finally, considering that the energy gap $\tilde{V}_1(r) - \tilde{V}_0(r)$ and $\sin 2\theta(r)$ are approximately symmetric with

[2] Some unquenched lattice QCD data [15] shows a small "bump" of $\tilde{V}_1(r)$ and $\theta(r)$ at short ranges, which the authors attribute to light meson exchange. Since we expect the mixing to be driven mainly by string breaking, we neglect such short-range features.

respect to the avoided crossing radius, we may write the general functional form of $V_{01}(r)$ as

$$V_{01}(r) = -\frac{\Delta}{2} f\left(\frac{V_{\mathrm{C}}(r) - T_1}{\Lambda}\right) \tag{4.16}$$

where Λ is some energy scale and $f(x)$ is in general a positive, even function, with an absolute maximum $f(0) = 1$, that vanishes for $|x| \gg 1$.

Chapter 5

The Diabatic Spectrum

In this chapter we calculate a spectrum of heavy-quark mesons using the diabatic approach. The building of the phenomenological diabatic potential matrix is the subject of Section 5.1. Then, in Section 5.2, we solve the diabatic Schrödinger equation with this potential by using a bound state approximation. The problem of the coupling between the bound states above threshold and the continuum of free meson-meson states is addressed in Section 5.3.

5.1 The Spectroscopic Potential

In the previous chapter, we have seen how the form of the diabatic potential matrix can be inferred from lattice QCD results. However, in practical applications, a suitable parametrization of the diabatic Hamiltonian must be constructed. It is also important, in order to obtain an accurate description of experimental data, to fix the parameters from a fitting to lattice data and phenomenology. Hence these parameters will have an effective character as they may be correcting, at least to some extent, the shortcomings of the diabatic approach.

So, the parameters of the quarkonium potential (1.10) can be fixed by fitting the spin-averaged spectrum of bottomonium and quarkonium states below threshold. As discussed in Section 1.2.1, this leads to the standard phenomenological values listed in Equation (1.12).

For what concerns the heavy-light meson masses, which determine the values of the reduced meson-meson masses μ_i and threshold masses T_i, we take them as the PDG values from [70].

In order to fix the parameters in the mixing potentials, we first need to generalize Equation (4.16) to the case of many thresholds. Equation (4.16)

was derived from the study of the static energy levels in unquenched lattice QCD with $Q\bar{Q}$ mixing with only a single meson-meson configuration [15]. However, the static energy levels have been also calculated in the case of two thresholds with distinct masses mixing with $Q\bar{Q}$ [17]. Although not as conclusive as the results obtained in the single-threshold case, those static energy levels are also compatible with mixing potentials of a similar shape, this is

$$V_{0i}(r) = -\frac{\Delta_Q}{2} f\left(\frac{V_{\mathrm{C}}(r) - T_i}{\Lambda}\right) \tag{5.1}$$

where $i = 0, 1, \ldots$ labels the meson-meson threshold, T_i is the corresponding mass, and we have introduced an effective, phenomenological energy gap Δ_Q, which we allow to be flavor-dependent in general. In contrast, we have assumed Λ to be flavor independent. We have also assumed Δ_Q and Λ to be the same for every threshold, meaning that the only difference between mixing potentials with different thresholds is given by the threshold mass inside the argument of f.

Secondly, we have to address the problem of degenerate thresholds. Let us consider, for example, a heavy-quark meson containing one $Q\bar{Q}$ (partial-wave) channel coupling with two meson-meson ones. The radial diabatic potential matrix for this system is

$$\begin{pmatrix} V_{\mathrm{C}}(r) & V_{01}(r) & V_{02}(r) \\ V_{01}(r) & T_1 & \\ V_{02}(r) & & T_2 \end{pmatrix}.$$

Let us now consider the case $T_2 = T_1$. From Equation (5.1), it is clear that in this case one has $V_{02}(r) = V_{01}(r)$. Then the potential matrix becomes

$$\begin{pmatrix} V_{\mathrm{C}}(r) & V_{01}(r) & V_{01}(r) \\ V_{01}(r) & T_1 & \\ V_{01}(r) & & T_1 \end{pmatrix}$$

and a simple change of basis transformation mixing the meson-meson channels reduces it into

$$\begin{pmatrix} V_{\mathrm{C}}(r) & \sqrt{2}V_{01}(r) & \\ \sqrt{2}V_{01}(r) & T_1 & \\ & & T_1 \end{pmatrix}.$$

This means that a heavy-quark meson system with two degenerate thresholds is physically equivalent to a system with only one effective threshold coupling to $Q\bar{Q}$, with a strength $\sqrt{2}$ times that of a nondegenerate threshold, plus a decoupled effective threshold. Furthermore, if two degenerate thresholds form an isospin doublet, such as in References [15] and [17], then it can be

shown that the effective threshold coupling to $Q\bar{Q}$ is given by their isoscalar combination, as required by isospin symmetry, while the decoupled one is associated with the isovector combination.

The energy gap has been calculated in unquenched lattice QCD [15] to be around 51 MeV. This value, calculated for a doubly degenerate threshold, corresponds to

$$\Delta_{\text{Lattice}} \approx 51/\sqrt{2}\ \text{MeV} \approx 36.1\ \text{MeV}$$

for the mixing strength with a nondegenerate threshold. The effective gap Δ_Q, on the other hand, may be fixed from the requirement that the spectroscopic potential yields a good description of quarkoniumlike mesons close below and above the lowest open-flavor threshold. For bottomoniumlike mesons, $Q \equiv b$, a good description is obtained for a value of

$$\Delta_b = 36.1\ \text{MeV}, \tag{5.2}$$

similar to the lattice one. As for charmoniumlike mesons, $Q \equiv c$, we shall see shortly that there is one experimental state, the $\chi_{c1}(3872)$, whose unconventional nature makes its mass the ideal parameter to tune the effective energy gap. This corresponds to a value of around

$$\Delta_c = 102.2\ \text{MeV}. \tag{5.3}$$

The reason for which the effective gap Δ_c is almost three times bigger than the value calculated in lattice QCD is still unclear at the moment of the writing. A short review of this open topic is given in Appendix B. Because of this, the study presented here should be considered as being purely phenomenological, at least in the charmoniumlike sector. The intended purpose of the current analysis is to present the descriptive power of the diabatic framework by assessing the capacity of string breaking to accommodate the spectrum of quarkoniumlike mesons interacting with open-flavor thresholds.

Finally, fixing the value of Λ requires choosing a suitable shape of the arbitrary function f in Equation (5.1). Recalling that f must be significant only near the avoided crossing radius r_i^{c}, defined by $V_{\text{C}}(r_i^{\text{c}}) = T_i$, and that $f(0) = 1$ by definition, we opt for the simplest Gaussian parametrization: $f(x) = e^{-x^2/2}$. This choice gives the spectroscopic mixing potential as

$$V_{0i}(r) = -\frac{\Delta_Q}{2} \exp\left\{ -\frac{1}{2}\left(\frac{V_{\text{C}}(r) - T_i}{\rho\sigma} \right)^2 \right\}, \tag{5.4}$$

where we have conveniently converted the energy scale Λ into a length scale ρ using the string tension,

$$\Lambda = \rho\sigma.$$

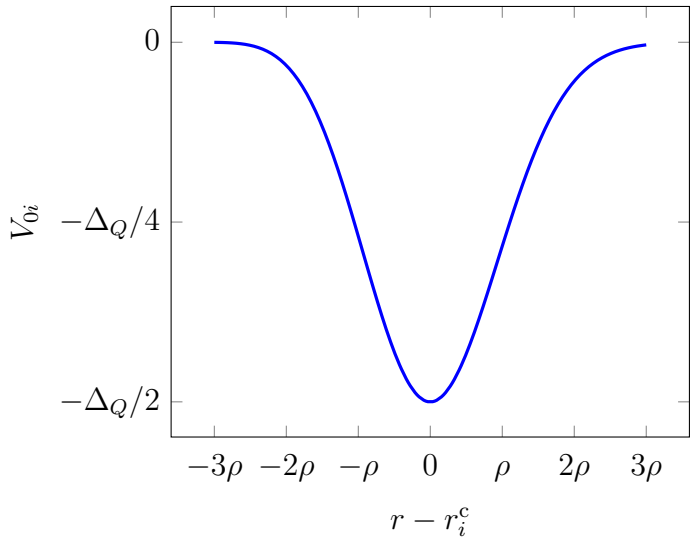

Figure 5.1: Mixing potential V_{0i} in the Gaussian parametrization (5.4), centered on the corresponding crossing radius r_i^c.

The Gaussian parametrization (5.4) of the mixing potential is plotted in Figure 5.1

Note that the particular choice of the function f makes no significant difference, as long as it respects the general features outlined above. Indeed, the freedom in the parametrization of f is reabsorbed in the energy scale Λ when fitting lattice data. This also means that, unlike the energy gap Δ_Q, the value of Λ is parametrization dependent. Then, a good fit of the mixing angle from [15] is obtained with

$$\rho = 0.3 \text{ fm}. \tag{5.5}$$

As a last remark, let us note that there is presumably an infinite number of open-flavor meson-meson thresholds coupling to $Q\bar{Q}$, but only a finite subset of them can be included in any numerical calculation. This may be a good approximation for any finite energy, as long as all thresholds with mass below or relatively close above the given energy are taken into account. In fact, under the assumption that the meson-meson static energy is approximately given by the threshold mass alone and the mixing potential has the general shape (4.16), it can be shown that a threshold with mass much higher than the given energy suffers a strong kinematical suppression and hardly plays any role. The same suppression may take place for the mixing with quarkonium hybrids, under reasonable assumptions on the unknown mixing potentials, for energies far below the minimum of the lowest hybrid potential. Hence,

Table 5.1: List of open-bottom meson-meson thresholds included in the diabatic study of this thesis.

Channel	Threshold (MeV)
$B\bar{B}$	10559.0
$B\bar{B}^*$	10604.2
$B^*\bar{B}^*$	10649.4
$B_s\bar{B}_s$	10733.8
$B_s\bar{B}_s^*$	10782.3
$B_s^*\bar{B}_s^*$	10830.8

one should keep in mind that a diabatic potential with $Q\bar{Q}$ and N thresholds can be deemed a good approximation of the complete meson system only as long as other neglected channels are strongly suppressed.

The spectroscopic study illustrated in this thesis includes only thresholds made of pseudoscalar or vector open-flavor mesons. Pseudovector open-flavor mesons or quarkonium hybrids are not considered. This limits the range of applicability of this study to energies below 10.8 and 4.1 GeV, respectively, for hidden-bottom and hidden-charm mesons. The complete list of open-bottom and open-charm thresholds included in this study are given in Tables 5.1 and 5.2, respectively. Note that the isospin-degenerate thresholds $B^{(*)+}B^{(*)-}$ and $B^{(*)0}\bar{B}^{(*)0}$ are combined in effective isosinglet thresholds $B^{(*)}\bar{B}^{(*)}$, with an effective mixing strength of $\sqrt{2}\Delta_b$. On the other hand, the isospin splittings between the $D^{(*)0}\bar{D}^{(*)0}$ and $D^{(*)+}D^{(*)-}$ thresholds are taken into account.

Notice also that, in some cases, some meson-meson channels may contribute to a given J^{PC} only as a kinematically suppressed partial wave ($l_i \gtrsim 2$) or not contribute at all, see Table 4.1. In some other cases, two partial-wave thresholds with the same l_i but different values of s_i may contribute at the same time. When that happens, these partial waves can be treated as degenerate thresholds and therefore combined into a single effective channel where the mixing strength is multiplied by a factor $\sqrt{2}$ with respect to that of the original partial waves.

5.2 Bound State Solutions

The solutions to the diabatic Schrödinger equation with the spherical potential matrix described in the previous sections provide all the physical information on a quarkoniumlike meson system, made of one $Q\bar{Q}$ and N meson-meson

Table 5.2: List of open-charm meson-meson thresholds included in the diabatic study of this thesis.

Channel	Threshold (MeV)
$D^0\bar{D}^0$	3729.6
D^+D^-	3739.4
$D^0\bar{D}^{*0}$	3871.7
D^+D^{*-}	3880.0
$D_s\bar{D}_s$	3936.6
$D^{*0}\bar{D}^{*0}$	4013.8
$D^{*+}D^{*-}$	4020.6
$D_s\bar{D}_s^*$	4080.5
$D_s^*\bar{D}_s^*$	4224.4

components in the given J^{PC} configuration. However, the way the physical information has to be extracted from these solutions is different depending on whether their energy is below or above the lowest open-flavor meson-meson threshold. In this section we shall deal with the former case. An approximate treatment above threshold is given in the next section.

Without loss of generality, let us assume that the thresholds are sorted in order of increasing mass, $T_i \leq T_{i+1}$ for every $i = 1, 2, \ldots, N$. For energies below the lowest threshold, $E < T_1$, the solutions form a discrete spectrum of bound states. Each of these bound-state solutions corresponds to a quarkoniumlike meson with quantum numbers J^{PC} and mass E that is stable against decays to open-flavor. The wave function $\Psi(\boldsymbol{r})$ of any such solution represents a normalizable quantum state, thus its square modulus $|\Psi(\boldsymbol{r})|^2$ can be interpreted as a probability density. The total probability of each component can be simply defined as the square modulus of the respective wave function component integrated over $\boldsymbol{r}$. With the help of the partial wave expansion (4.8) and the orthogonality condition (1.16), it is then easy to show that the total $Q\bar{Q}$, $M_1^i\bar{M}_2^i$ probabilities are given, respectively, by

$$\mathfrak{p}_0 = \sum_t \int \mathrm{d}r |u_0^t(r)|^2,$$

$$\mathfrak{p}_i = \sum_k \int \mathrm{d}r |u_i^k(r)|^2$$

with $u_0^t(r) = rR_0^t(r)$ and $u_i^k(r) = rR_i^k(r)$ the reduced radial wave functions. The diabatic spectrum of bottomoniumlike and charmoniumlike bound states

is listed in Tables 5.3 and 5.4, respectively. The numerical method used to solve the diabatic Schrödinger equation is detailed in Appendix C.

From the calculated probabilities in Tables 5.3 and 5.4, it is clear that the lowest-lying diabatic states are just quarkonium mesons. This is even more clear from the comparison between the diabatic spectrum and that of low-lying quarkonium states in Tables 1.1 and 1.2, respectively. There is an almost perfect correspondence between the calculated diabatic and quarkonium masses with only one notable exception that we discuss next. As can be checked, states whose mass lies far below any open-flavor threshold are pure quarkonium states and have the same mass as obtained from the Cornell potential alone. On the other hand, states somewhat closer below threshold possess some small meson-meson component(s) and a mass slightly smaller than the corresponding one in the spin-independent Cornell spectrum of Tables 1.1 and 1.2, signaling an attractive nature of the threshold interaction induced by string breaking.

5.2.1 $\chi_{c1}(3872)$ in the Diabatic Framework

There is one 1^{++} state in the diabatic spectrum of Table 5.4 that does not correspond to any charmonium state of Table 1.2 or 1.4. Actually, the mixing strength Δ_c has been fixed to get this supernumerary state, with a calculated mass very close below the $D^0\bar{D}^{*0}$ threshold at 3871.7 MeV, in natural correspondence with the famous $X(3872)$ meson, discovered by the Belle collaboration in 2003 [77] and now labeled $\chi_{c1}(3872)$ in the PDG particle listings [70] as per its 1^{++} quantum numbers.

The $\chi_{c1}(3872)$ was the first well-established experimental meson state to be candidate for exotic structure, this is, whose properties were at odds with those expected for a bound state of a quark-antiquark pair. In fact, while its discovery channel $\pi^+\pi^- J/\psi$ suggests that its minimal quark configuration must contain at least a $c\bar{c}$ pair, its PDG average mass of 3871.65 ± 0.06 MeV [70] (compatible with the $D^0\bar{D}^{*0}$ threshold within errors) has no counterpart in the charmonium spectrum of Table 1.2 or 1.4. Moreover, its decay width to $\omega J/\psi$ has been observed to be compatible with that to $\pi^+\pi^- J/\psi$ [78, 79]. This fact, under the assumption that many of the produced $\pi^+\pi^-$ come from the decay of an intermediate ρ meson, is in contrast with the naive expectation that a $c\bar{c}$ state, having isospin zero, is forbidden to emit a ρ under isospin symmetry.

The puzzling properties of $\chi_{c1}(3872)$ can be more easily understood from our assignment to the supernumerary charmoniumlike state calculated in the diabatic framework. Indeed, from its diabatic wave function one may give account of many of its observed decay properties, as we show next.

Table 5.3: Diabatic spectrum of bottomoniumlike bound states with their J^{PC} quantum numbers, mass M, $b\bar{b}$ probability, and open-bottom meson-meson probabilities.

J^{PC}	M (MeV)	$b\bar{b}$	$B\bar{B}$	$B\bar{B}^*$	$B^*\bar{B}^*$
0^{++}	9900.7	100%			
	10254.2	100%			
	10531.1	92%	7%		1%
1^{++}	9900.7	100%			
	10254.3	100%			
	10532.8	97%		2%	1%
2^{++}	9900.7	100%			
	10254.1	100%			
	10341.0	100%			
	10529.2	95%	2%	1%	2%
1^{--}	9401.3	100%			
	9993.8	100%			
	10150.3	100%			
	10337.5	100%			
	10439.8	99%	1%		

Table 5.4: Diabatic spectrum of charmoniumlike bound states with their J^{PC} quantum numbers, mass M, $c\bar{c}$ probability, and open-charm meson-meson probabilities.

J^{PC}	M (MeV)	$c\bar{c}$	$D^0\bar{D}^0$	D^+D^-	$D^0\bar{D}^{*0}$	D^+D^{*-}
0^{++}	3508.6	99%	1%			
1^{++}	3509.7	100%				
	3871.6	4%			93%	3%
2^{++}	3508.4	100%				
1^{--}	3082.4	100%				
	3657.3	93%	3%	2%	1%	1%

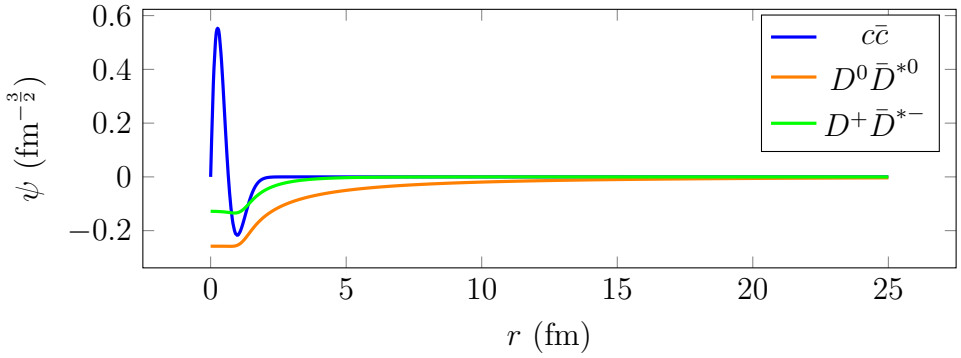

Figure 5.2: Radial wave function of $\chi_{c1}(3872)$.

The diabatic wave function of $\chi_{c1}(3872)$ is plotted in Figure 5.2. As one can see, the diabatic state is composed of $c\bar{c}$ and $D^0\bar{D}^{*0}$ components with comparable probability density at short range, which is compatible with phenomenological indications about the short-distance properties of $\chi_{c1}(3872)$, in particular its EM decays, see, for example, [80, 81] and references therein. Then, for $r \gtrsim 3$ fm the confined $c\bar{c}$ and deeply bound meson-meson components fade, leaving only a very long tail due to the loosely bound $D^0\bar{D}^{*0}$ component. This molecular component is in fact so extended (with 14 fm of root-mean-square radius) that it dominates the overall composition of the diabatic $\chi_{c1}(3872)$ state with a total 93% total probability, against a mere 4% for $c\bar{c}$ and 3% for $D^+\bar{D}^{*-}$. This composition may help understanding the baffling decay widths of $\chi_{c1}(3872)$ to $\pi^+\pi^- J/\psi$ and $\omega J/\psi$. Indeed, the dominant $D^0\bar{D}^{*0}$ component contains, unlike $c\bar{c}$, both isospin-zero and isospin-one components in equal amounts, so no isospin suppression is expected for $\chi_{c1}(3872) \to \pi^+\pi^- J/\psi$ through an intermediate ρ emission.

To summarize, the diabatic description of $\chi_{c1}(3872)$ is that of a loosely bound $D^0\bar{D}^{*0}$ molecule, where the binding is provided through (effective) string breaking by a small $c\bar{c}$ component at its core. This picture is somehow equivalent to that of molecular models, see, for instance, [37–42] and references therein, where hadronic molecules are generated from nonperturbative meson-meson interactions.

5.3 Fano Resonances

For energy above the lowest threshold, $E > T_1$, the situation changes quite dramatically because of the presence of one or more open meson-meson channels. The exact (numerical) treatment of these solutions and their

interpretation in terms of meson-meson scattering states are explained in detail in Chapter 6. For now it suffices to say that the wave function components associated to the open thresholds are not normalizable, which makes the connection between solutions above threshold and quarkoniumlike meson states somewhat more intricate.

5.3.1 Bound State Approximation

As an alternative to the full scattering treatment, one may follow a *bound state approximation* [60]. Thanks to its simplicity, this treatment, albeit being approximate, may help us shed some light on the role played by the quark-antiquark–meson-meson mixing for states above threshold.

Let us consider an energy E above a certain number $n \leq N$ of thresholds, $E > T_j$ for $j = 1, 2, \ldots, n$. The bound-state approximation consists in separating the diabatic potential operator with N thresholds in a bare potential $\mathring{V}$ plus an interaction potential V_{I}:

$$V = \mathring{V} + V_{\mathrm{I}} \tag{5.6}$$

with

$$\mathring{V} = \begin{pmatrix} V_{00} & & & & V_{0n+1} & \cdots & V_{NN} \\ & T_1 & & & & & \\ & & \ddots & & & & \\ & & & T_n & & & \\ V_{0n+1} & & & & T_{n+1} & & \\ \vdots & & & & & \ddots & \\ V_{0N} & & & & & & T_N \end{pmatrix}$$

and

$$V_{\mathrm{I}} = \begin{pmatrix} & V_{01} & \cdots & V_{0n} & & & \\ V_{01} & & & & & & \\ \vdots & & & & & & \\ V_{0n} & & & & & & \\ & & & & & & \\ & & & & & & \end{pmatrix}.$$

As one can see from its expression, the solutions of the bare potential $\mathring{V}$ consist in a discrete spectrum of bound states,

$$(K + \mathring{V})\,|\mathring{\Psi}\rangle = \mathring{M}\,|\mathring{\Psi}\rangle$$

with $\mathring{M}$ the bare mass and $|\mathring{\Psi}\rangle$ the bare bound state

$$|\mathring{\Psi}\rangle = \begin{pmatrix} |\mathring{\psi}_0\rangle \\ |\mathring{\psi}_{n+1}\rangle \\ \vdots \\ |\mathring{\psi}_N\rangle \end{pmatrix}$$

containing only the $Q\bar{Q}$ and closed meson-meson components, plus n different continuum spectra,

$$(K + \mathring{V})\,|\tilde{\Psi}_j\rangle = E_j(p)\,|\tilde{\Psi}_j\rangle$$

where $E_j(p)$ is the meson-meson energy in the center-of-mass reference frame,

$$E_j(p) = T_j + \frac{p^2}{2\mu_j}$$

with p the relative meson-meson momenta, and $|\tilde{\Psi}_j\rangle$ the free meson-meson state

$$|\tilde{\Psi}_j\rangle = \begin{pmatrix} |\tilde{\psi}_j\rangle \\ \\ \\ \end{pmatrix}$$

containing only the meson-meson component j.

In the bound state approximation, an approximate solution above threshold is constructed through two separate steps:

1. Given a number n of open thresholds, the bare potential $\mathring{V}$ is constructed and its spectrum calculated for bare masses within the range $\mathring{M} \in [T_n, T_{n+1}]$.

2. The coupling with the open thresholds, mediated by the interaction potential V_{I}, is reintroduced. This gives the bound-state solutions a width for the decay to an open-flavor meson-meson pair as well as a mass shift from meson loops.

In this manner, by varying the energy or, equivalently, the number n of open thresholds we get the complete bound state spectrum. Let us note that each threshold is treated differently depending on whether it is open or closed. More precisely, if the threshold is closed, its corresponding mixing potential is included in the bare potential $\mathring{V}$. Otherwise, it appears in the interaction

potential $V_{\rm I}$. This procedure may be deemed to yield a good approximation only for states whose corrections coming from $V_{\rm I}$ do not bring their masses outside the range $[T_n, T_{n+1}]$, this is, the range of validity of the decomposition (5.6) for a given number n of open thresholds. Otherwise, one cannot regard the calculated bound state as a consistent approximation to a resonant state of the full diabatic system.

The spectrum of bound-state solutions is listed in Tables 5.5 and 5.6 for bottomoniumlike and charmoniumlike states, respectively. One can easily notice that there are many supernumerary bound-state solutions with respect to the Cornell spectrum in Tables 1.1 and 1.2 (or Tables 1.3 and 1.4). In previous works [59–61] some of these states were discarded by arguing a one-to-one correspondence between diabatic and Cornell states, implying that the supernumerary states were artifacts of the bound-state approximation. However, a diabatic analysis of open-flavor meson-meson scattering [62, 82] reveals that these solutions should not be discarded. Hence, they are kept in the current analysis. Note also that in the charmoniumlike case we have taken into account the different threshold masses between $D^{(*)0}\bar{D}^{(*)0}$ and $D^{(*)+}D^{(*)-}$ channels, unlike in References [59, 60] where effective isospin zero $D^{(*)}\bar{D}^{(*)}$ channels were considered.

5.3.2 Mass Corrections and Widths

The coupling of a discrete spectrum of states to a continuum spectrum of decay products transforms each bound state into a resonance whose position and width can be calculated using a procedure by Fano [83]. In our context, a bound state with bare mass $\mathring{M}$ becomes a resonance with mass M determined implicitly by the relation

$$M - \mathring{M} = \sum_{j,k} \mathcal{P}\!\int_0^\infty \mathrm{d}p \frac{p^2}{M - E_j(p)} \left|\mathcal{I}_j^k(p)\right|^2, \tag{5.7}$$

with $\mathcal{P}\!\int$ for Cauchy principal value integral, and width

$$\frac{\Gamma}{2} = \sum_{j,k} \pi p_j \left|\mathcal{I}_j^k(p_j)\right|^2, \tag{5.8}$$

where $\mathcal{I}_j^k(p)$ is the radial transition matrix element

$$\mathcal{I}_j^k(p) = \sqrt{\frac{2}{\pi}} i^{-l_j^k} \int \mathrm{d}r\, r^2 j_{l_j^k}(pr) V_{0j}(r) \left(\textstyle\sum_t R_0^t(r)\right)$$

and

$$p_j = \sqrt{2\mu_j(M - T_j)}$$

is the nonrelativistic meson-meson momentum in channel j. The detailed derivation of the mass correction and width can be found in [48, 83]. Their adaptation to the diabatic framework, which yields the expressions given above, is explained in [60].

The physical picture behind the mass correction (5.7) is that the bound state $|\mathring{\Psi}\rangle$ receives a contribution to its self-energy from open-flavor meson loops. This, however, does not mean that Equation (5.7) should be interpreted as a perturbative loop correction. On the contrary, it can be shown that, whilst a perturbative calculation at leading order yields a very similar result, the perturbative expansion diverges at next-to-leading order. More details on this can be found in Appendix of Reference [60].

The width (5.8) is the total width of the resonance for decays into open-flavor meson-meson pairs. It can be expressed as a sum of partial widths

$$\Gamma = \sum_j \Gamma_j$$

with

$$\Gamma_j = 2\pi p_j \sum_k \left|\mathcal{I}_j^k(p_j)\right|^2,$$

where the residual sum is over partial waves labeled by k.

The diabatic spectrum of bottomoniumlike and charmoniumlike resonances calculated within the bound-state approximation is listed in Tables 5.7 and 5.8, respectively. As one can see comparing the second and third columns, there are both positive and negative mass corrections from the open thresholds. This is in contrast to the situation below threshold, where inclusion of closed thresholds results in a downward shift of the masses with respect to the pure quarkonium spectrum. Notice that states marked by an asterisk in Tables 5.5 and 5.6 do not appear in the corresponding corrected spectra. This is because, for these bound states, the correction calculated with Equation (5.7) would result in a resonance mass M below the highest open threshold or above the lowest closed threshold considered in their calculation. This behavior is an artifact of the bound-state approximation, due to the asymmetric treatment of the $Q\bar{Q}$–meson-meson mixing between open and closed thresholds. It is not clear yet how these cases should be interpreted.

To summarize, the bound-state approximation has the great virtue of providing an intuitive representation for the physics of a quarkoniumlike system with energy above threshold. This description consists in a spectrum of resonances with mass M and widths to open-flavor meson-meson channels

Γ_j calculated from the diabatic potential matrix. Moreover, an approximate bound-state wave function is provided for each resonance. These wave functions may be used not only to obtain the probability composition of each state, but also to calculate other decay modes like, for example, leptonic ones, see [59–61]. However, the bound state approximation does not give a completely unified treatment, and it fails in those cases where the mass corrections change the position of a state relative to the meson-meson thresholds. A unified and detailed understanding of the resonant structures requires a scattering analysis, which is the subject of the next chapter.

Table 5.5: Spectrum of bottomoniumlike bound states above threshold, including the J^{PC} quantum numbers, bare mass $\mathring{M}$, $b\bar{b}$ probability, and open-bottom meson-meson probabilities. An asterisk preceding a bare mass value means that the state is spurious, in the sense that it goes out of the range of validity of the bound state approximation when corrections from open thresholds are included.

J^{PC}	$\mathring{M}$ (MeV)	$b\bar{b}$	$B\bar{B}^*$	$B^*\bar{B}^*$	$B_s\bar{B}_s$	$B_s\bar{B}_s^*$	$B_s^*\bar{B}_s^*$
0^{++}	10780.4	98%					2%
1^{++}	10776.0	76%				24%	
2^{++}	10593.9	93%	3%	4%			
	*10777.1	93%				4%	3%
1^{--}	10600.8	72%	22%	6%			
	*10607.2	92%		8%			
	10691.8	98%			1%		1%

Table 5.6: Spectrum of charmoniumlike bound states above threshold, including the J^{PC} quantum numbers, bare mass $\mathring{M}$, $c\bar{c}$ probability, and open-charm meson-meson probabilities. An asterisk preceding a bare mass value means that the state is spurious, in the sense that it goes out of the range of validity of the bound state approximation when corrections from open thresholds are included.

J^{PC}	$\mathring{M}$ (MeV)	$c\bar{c}$	$D^0\bar{D}^{*0}$	D^+D^{*-}	$D_s\bar{D}_s$	$D^{*0}\bar{D}^{*0}$	$D^{*+}D^{*-}$	$D_s\bar{D}_s^*$	$D_s^*\bar{D}_s^*$
0^{++}	3923.8	62%			32%	3%	3%		
	*3938.1	90%				5%	5%		
1^{++}	3943.7	96%				1%	1%	2%	
2^{++}	*3911.9	78%			5%	8%	7%	1%	1%
	4006.3	74%				17%	9%		
	*4013.9	70%					29%	1%	
1^{--}	3785.8	96%	1%	1%	1%	1%			
	*4001.4	41%				31%	24%	3%	1%
	*4075.3	69%						28%	3%

Table 5.7: Spectrum of bottomoniumlike resonances in the bound-state approximation. The bare mass $\mathring{M}$, corrected mass M, total open-bottom meson-meson width Γ, and partial widths are all in MeV units.

J^{PC}	$\mathring{M}$	M	Γ	$\Gamma_{B\bar{B}}$	$\Gamma_{B\bar{B}^*}$	$\Gamma_{B^*\bar{B}^*}$	$\Gamma_{B_s\bar{B}_s}$
0^{++}	10780.4	10787.9	9.4	2.3		5.3	1.8
1^{++}	10776.0	10780.9	2.2		1.3	0.9	
2^{++}	10593.9	10589.3	5.2	5.2			
1^{--}	10600.8	10603.8	22.4	22.4			
	10691.8	10700.2	46.0	3.1	0.4	42.5	

Table 5.8: Spectrum of charmoniumlike resonances in the bound-state approximation. The bare mass $\mathring{M}$, corrected mass M, total open-charm meson-meson width Γ, and partial widths are all in MeV units.

J^{PC}	$\mathring{M}$	M	Γ	$\Gamma_{D^0\bar{D}^0}$	$\Gamma_{D^+D^-}$	$\Gamma_{D^0\bar{D}^{*0}}$	$\Gamma_{D^+D^{*-}}$	$\Gamma_{D_s\bar{D}_s}$
0^{++}	3923.8	3925.8	2.3	1.4	0.9			
1^{++}	3943.7	3952.4	80.5	38.2	42.3			
2^{++}	4006.3	4003.8	22.5	3.2	3.4	6.1	6.0	3.8
1^{--}	3785.8	3766.8	21.8	12.6	9.2			

Chapter 6

Coupled-Channel Meson-Meson Scattering

In this chapter we develop a complete diabatic treatment of heavy-quark mesons above threshold, this is, a diabatic description of coupled-channel meson-meson scattering [62]. Specifically, in Section 6.1, we examine the analytical properties of solutions of the diabatic Schrödinger equation above one and more open-flavor meson-meson thresholds. In Section 6.2 we relate these solutions to the stationary states in a coupled-channel meson-meson scattering problem and derive a general formula for calculating the on-shell S matrix. Finally, in Section 6.3, we compare the calculated cross-sections with results from the bound-state approximation and existing data.

6.1 Asymptotic Solutions above Threshold

6.1.1 Single Threshold with Single Partial Wave

The solutions of the diabatic Schrödinger equation have some well-defined properties at large distances, which allow to derive general analytical expressions for their asymptotic behavior as $r \to \infty$. The simplest possible example is that of a diabatic system with only one threshold T_1 with a single partial wave (l_1^1, s_1^1) coupling to the given J^{PC}.

Let us begin, for the sake of simplicity, with a nonphysical example where string breaking effects are neglected, i.e., we artificially set $V_{01}(r) = 0$. In this case it is obvious that the spectrum of solutions factorizes in a discrete spectrum of pure quarkonium states, for which the mass M and $Q\bar{Q}$ reduced wave function $u_0^t(r)$ correspond to a solution of the Cornell potential and $u_1^1(r) = 0$, plus a continuum of free meson-meson states with center-of-mass

energy $E \geq T_1$, $u_0^t(r) = 0$, and $u_1^1(r)$ the spherical solution of the free Schrödinger equation,

$$u_1^1(r) = \sqrt{\frac{2}{\pi}\mu_1 p_1 i^{l_1^1}}\, r j_{l_1^1}(p_1 r)$$

where $p_1 = \sqrt{2\mu_1(E - T_1)}$ is the modulus of the relative meson-meson momentum and the normalization factor $\sqrt{\frac{2}{\pi}\mu_1 p_1 i^{l_1^1}}$ is chosen to facilitate the comparison with the scattering states normalized by energy that will be introduced in Section 6.2.1. These analytical solutions of the free radial Schrödinger equation have the well-known asymptotic behavior

$$u_1^1(r) \simeq \sqrt{\frac{2}{\pi}\frac{\mu_1}{p_1}} i^{l_1^1} \sin\Big(p_1 r - l_1^1 \frac{\pi}{2}\Big),$$

where we have introduced the equivalence relation $\simeq$ for asymptotic equality in the limit $r \to \infty$ and used

$$j_l(pr) \simeq \frac{1}{pr} \sin\left(pr - l\frac{\pi}{2}\right)$$

for the spherical Bessel functions.

When string breaking is included, the mixing potential $V_{01}(r)$ is not zero and the continuum solutions are not pure meson-meson states. Instead, the analytical continuum solutions possess a $Q\bar{Q}$ component. Although this confined $Q\bar{Q}$ component has a trivial asymptotic behavior $u_0^t \simeq 0$ in all cases, its mixing effect is reflected in the asymptotic behavior of the meson-meson component through a phase shift η_1^1 with respect to a free wave:

$$u_1^1(r) \simeq \sqrt{\frac{2}{\pi}\frac{\mu_1}{p_1}} i^{l_1^1} e^{i\eta_1^1} \sin\Big(p_1 r - l_1^1 \frac{\pi}{2} + \eta_1^1\Big). \tag{6.1}$$

These continuum solutions can be naturally interpreted as stationary states of a meson-meson pair scattering through their mixing with $Q\bar{Q}$.

The form (6.1) of the asymptotic behavior is perfectly general under the assumption that the scattering interaction has a finite range,[1] which is clearly the case of our diabatic potential with a confining $Q\bar{Q}$ potential and a $Q\bar{Q}$–meson-meson mixing being significant only near the avoided crossing radius. Notice that all information about the mixing interaction is encoded in the phase shift.

In the rest of this chapter, we shall focus on the asymptotic behavior of the meson-meson components, which contain all physical information about the scattering process.

[1] See any textbook on quantum mechanical scattering, like [84], for example.

6.1.2 Single Threshold with Many Partial Waves

Let us now allow for the single threshold T_1 to have $\mathfrak{n}_1$ partial waves coupling to J^{PC}, (l_1^k, s_1^k) with $k = 1, 2, \ldots, \mathfrak{n}_1$. In this case each continuum solution is degenerate, with the degree of degeneracy equal to $\mathfrak{n}_1$, and an additional label $h = 1, 2, \ldots, \mathfrak{n}_1$ is necessary to distinguish linearly independent solutions.

The reduced wave function components at large distances may be cast as[2]

$$u_{1,h}^k(r) \simeq \sqrt{\frac{2}{\pi}\frac{\mu_1}{p_1}} i^{l_1^k} a_{1,h}^k \sin\Big(p_1 r - l_1^k \frac{\pi}{2} + \eta_{1,h}^k\Big). \tag{6.2}$$

As one can see, the main difference with respect to Equation (6.1) is the appearance of the coefficients $a_{1,h}^k$. If string breaking effects were neglected, one would trivially have $\eta_{1,h}^k = 0$ and $a_{1,h}^k = \delta_h^k$. With the diabatic mixing in place, the phase shifts $\eta_{1,h}^k$ contain information on the scattering in each partial-wave channel, while the coefficients $a_{1,h}^k$ give account of the probability flow between them.

6.1.3 Many Thresholds

Finally, in the most general case of an arbitrary number N of thresholds, the number of open channels, and hence the degree of degeneracy of the continuum solutions, depends on the energy. If at some energy value E in the continuum spectrum there is a number $n \leq N$ of open thresholds, $E \geq T_j$ with $j = 1, 2, \ldots, n$, each with $\mathfrak{n}_j$ partial waves coupling to J^{PC}, (l_j^k, s_j^k) with $k = 1, 2 \ldots, \mathfrak{n}_j$, then that energy level is degenerate $\tilde{n}$ times, with $\tilde{n} = \sum_j \mathfrak{n}_j$ the total number of partial waves coupling to J^{PC} from all open channels.

It is easy to show that for the reduced wave functions corresponding to closed meson-meson channels one has

$$u_i^k(r) \simeq e^{-r\sqrt{2\mu_i(T_i - E)}} \simeq 0 \qquad \text{for} \qquad i = n+1, n+2, \ldots, N.$$

As for the reduced wave functions associated to the open channels, their asymptotic behavior is a straightforward generalization of Equation (6.2),

$$u_{j,h}^k(r) \simeq \sqrt{\frac{2}{\pi}\frac{\mu_j}{p_j}} i^{l_j^k} a_{j,h}^k \sin\Big(p_j r - l_j^k \frac{\pi}{2} + \eta_{j,h}^k\Big) \tag{6.3}$$

where the label h now goes from 1 to $\tilde{n}$. Notice that the modulus of the meson-meson momentum, $p_j = \sqrt{2\mu_j(E - T_j)}$, is in general different for each channel.

[2]Compare, for instance, with Equations (12) and (14) in [85].

These solutions correspond to stationary states of a coupled-channel meson-meson scattering system. All the physical information on the scattering process is exhausted by the asymptotic behavior of the open channels through the coefficients $a^k_{j,h}$ and phase shifts $\eta^k_{j,h}$. Their values can be calculated numerically by fitting Equation (6.3) to the long-distance part of a continuum numerical solution of the diabatic Schrödinger equation. A way to calculate all the linearly independent numerical solutions for any continuum energy E is illustrated in Appendix C.

6.2 The S Matrix

6.2.1 Asymptotic Scattering States

The diabatic mixing induced by string breaking mediates a nonperturbative meson-meson scattering interaction. Pictorially, the scattering process can be thought as an initial open-flavor meson pair $M_1^{j'}\bar{M}_2^{j'}$ scattering into a final state $M_1^{j}\bar{M}_2^{j}$ via an intermediate $Q\bar{Q}$ state,

$$M_1^{j'}\bar{M}_2^{j'} \to (Q\bar{Q}) \to M_1^{j}\bar{M}_2^{j}.$$

This physical image can be also represented in a diagrammatic form, see top panel of Figure 6.1.

This mechanism is different from the meson-meson interaction mediated by light meson exchange, see bottom panel of Figure 6.1, often studied in heavy hadron EFTs. In the diabatic framework, where all dynamical information about light degrees of freedom is encoded in the diabatic potential, such interactions would be included as elements of the meson-meson potential submatrix. Our ansatz $V_{jj'}(r) = T_j\delta_{jj'}$ is equivalent to the assumption that, in diabatic meson-meson scattering, the effect of light-meson exchange is negligible with respect to the string-breaking induced interaction.

Treating open-flavor mesons as pointlike particles, the asymptotic scattering state from an initial $M_1^{j'}\bar{M}_2^{j'}$ state, with spins s_1', s_2' and projections σ_1', σ_2', into a final $M_1^{j}\bar{M}_2^{j}$ state, with spins s_1, s_2 and projections σ_1, σ_2, can be cast in the general form[3]

$$\psi^{\sigma_1,\sigma_2,\sigma_1',\sigma_2'}_{j\leftarrow j',\hat{\boldsymbol{p}}}(\boldsymbol{r}) \simeq \frac{\sqrt{\mu_j p_j}}{(2\pi)^{\frac{3}{2}}}\left(\delta_{jj'}\delta_{\sigma_1\sigma_1'}\delta_{\sigma_2\sigma_2'}e^{i\boldsymbol{p}_{j'}\cdot\boldsymbol{r}} + f^{\sigma_1,\sigma_2,\sigma_1',\sigma_2'}_{j\leftarrow j'}(\hat{\boldsymbol{p}}\cdot\hat{\boldsymbol{r}})\frac{e^{ip_j r}}{r}\right) \quad (6.4)$$

where $f^{\sigma_1,\sigma_2,\sigma_1',\sigma_2'}_{j\leftarrow j'}(\hat{\boldsymbol{p}}\cdot\hat{\boldsymbol{r}})$ is the scattering amplitude and $\boldsymbol{p}_{j'} = \hat{\boldsymbol{p}}\,p_{j'}$, with $\hat{\boldsymbol{p}}$ and $\hat{\boldsymbol{r}}$ the beam and detection directions, respectively. Notice that, similarly

[3] See, for instance, Eq. (20.11) in [84].

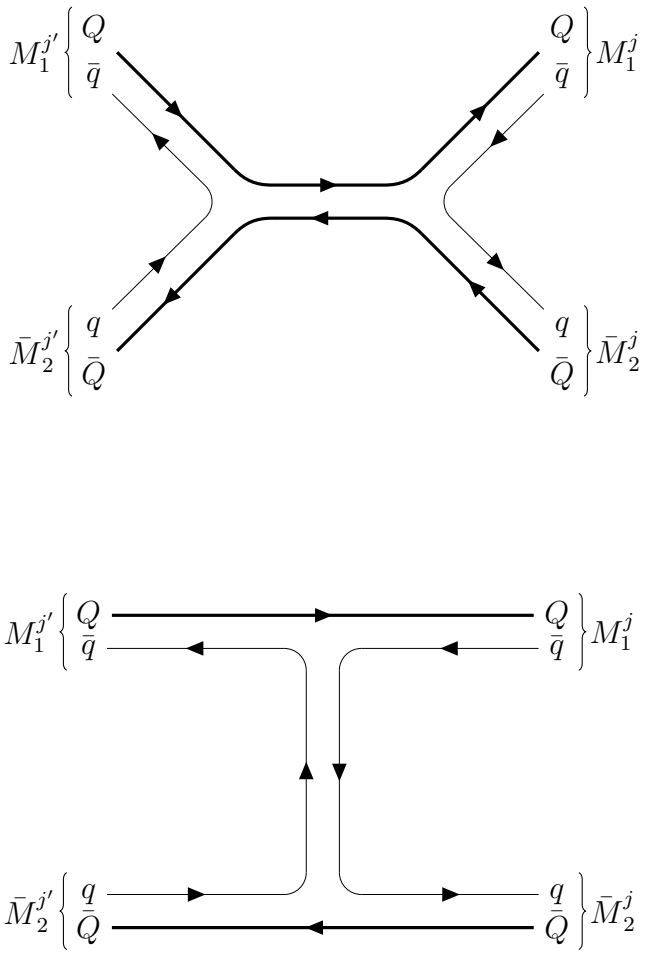

Figure 6.1: Diagrammatic representation of meson-meson scattering interactions. Heavy and light quarks are drawn with thick and thin lines, respectively. Top panel: scattering mediated by mixing with $Q\bar{Q}$. Bottom panel: scattering mediated by light meson exchange.

to what we have done with the J^{PC} labels for the solutions of the diabatic Schrödinger equation, we have omitted the labels s_1, s_2, s_1', s_2' from the scattering states, in order to simplify the notation.

In order to better compare the asymptotic scattering states with the radial solutions above threshold (6.3), we use the plane wave expansion,

$$\begin{aligned} e^{i\boldsymbol{p}_{j'}\cdot\boldsymbol{r}} &= 4\pi \sum_{l',m_l'} i^{l'} j_{l'}(p_{j'}r) Y_{l'}^{m_l'}(\hat{\boldsymbol{r}}) Y_{l'}^{m_l'*}(\hat{\boldsymbol{p}}) \\ &= 4\pi \sum_{l,m_l} \sum_{l',m_l'} \delta_{ll'}\delta_{m_l m_l'} i^{l} j_{l}(p_{j'}r) Y_{l}^{m_l}(\hat{\boldsymbol{r}}) Y_{l'}^{m_l'*}(\hat{\boldsymbol{p}}) \end{aligned} \tag{6.5}$$

where in the second line we have introduced an additional sum over l, m_l using two Kronecker deltas. Using Equation (6.5), the first term inside parentheses on the right hand side of (6.4) can be rearranged as

$$\begin{aligned} \delta_{jj'}\delta_{\sigma_1\sigma_1'}\delta_{\sigma_2\sigma_2'} e^{i\boldsymbol{p}_{j'}\cdot\boldsymbol{r}} = 4\pi \sum_{J,m_J} \sum_{l,m_l} \sum_{s,m_s} \sum_{l',m_l'} \sum_{s',m_s'} \delta_{jj'}\delta_{ll'}\delta_{ss'} i^{l} j_l(p_j r) \\ C_{s_1,s_2,s}^{\sigma_1,\sigma_2,m_s} C_{l,s,J}^{m_l,m_s,m_J} Y_l^{m_l}(\hat{\boldsymbol{r}}) C_{s_1',s_2',s'}^{\sigma_1',\sigma_2',m_s'} C_{l',s',J}^{m_l',m_s',m_J} Y_{l'}^{m_l'*}(\hat{\boldsymbol{p}}), \end{aligned} \tag{6.6}$$

where we have introduced multiple times the orthogonality relation of the Clebsch-Gordan coefficients and utilized the multiplying $\delta_{jj'}$ to substitute $p_{j'}$ by p_j inside the argument of the spherical Bessel function.

In a similar fashion, we can expand the scattering amplitudes as

$$f_{j\leftarrow j'}^{\sigma_1,\sigma_2,\sigma_1',\sigma_2'}(\hat{\boldsymbol{p}}\cdot\hat{\boldsymbol{r}}) = 4\pi \sum_{l,m_l} \sum_{l',m_l'} f_{j\leftarrow j'}^{l,m_l,l',m_l',\sigma_1,\sigma_2,\sigma_1',\sigma_2'} Y_l^{m_l}(\hat{\boldsymbol{r}}) Y_{l'}^{m_l'*}(\hat{\boldsymbol{p}})$$

and then rewrite it as

$$\begin{aligned} f_{j\leftarrow j'}^{\sigma_1,\sigma_2,\sigma_1',\sigma_2'}(\hat{\boldsymbol{p}}\cdot\hat{\boldsymbol{r}}) = 4\pi \sum_{J,m_J} \sum_{l,m_l} \sum_{s,m_s} \sum_{l',m_l'} \sum_{s',m_s'} f_{j\leftarrow j'}^{l,s,l',s'} \\ C_{s_1,s_2,s}^{\sigma_1,\sigma_2,m_s} C_{l,s,J}^{m_l,m_s,m_J} Y_l^{m_l}(\hat{\boldsymbol{r}}) C_{s_1',s_2',s'}^{\sigma_1',\sigma_2',m_s'} C_{l',s',J}^{m_l',m_s',m_J} Y_{l'}^{m_l'*}(\hat{\boldsymbol{p}}), \end{aligned} \tag{6.7}$$

where we have used angular momentum algebra and total momentum conservation to expand the scattering amplitude in terms of spin-orbital partial wave amplitudes, $f_{j\leftarrow j'}^{l,s,l',s'}$, and Clebsch-Gordan coefficients. Notice that, in order to simplify the notation, we have suppressed the total angular momentum label J in the scattering amplitude. It is understood to be implicit.

Furthermore, from the definition of the spin-orbital wave functions[4] it follows that

$$\sum_{m_l,m_s} C^{\sigma_1,\sigma_2,m_s}_{s_1,s_2,s} C^{m_l,m_s,m_J}_{l,s,J} Y^{m_l}_{l}(\hat{\boldsymbol{r}}) = \xi^{\sigma_1\dagger}_{s_1}\xi^{\sigma_2\dagger}_{s_2}\mathcal{Y}^{m_J}_{l,s,J}(\hat{\boldsymbol{r}}) \tag{6.8}$$

$$\sum_{m'_l,m'_s} C^{\sigma'_1,\sigma'_2,m'_s}_{s'_1,s'_2,s'} C^{m'_l,m'_s,m_J}_{l',s',J} Y^{m'_l *}_{l'}(\hat{\boldsymbol{p}}) = \mathcal{Y}^{m_J\dagger}_{l',s',J}(\hat{\boldsymbol{p}})\xi^{\sigma'_1}_{s'_1}\xi^{\sigma'_2}_{s'_2} \tag{6.9}$$

So, inserting Equations (6.6)-(6.9) into Equation (6.4), the asymptotic scattering states can be written as an expansion in reduced radial wave functions,

$$\psi^{\sigma_1,\sigma_2,\sigma'_1,\sigma'_2}_{j\leftarrow j',\hat{\boldsymbol{p}}}(\boldsymbol{r}) = \xi^{\sigma_1\dagger}_{s_1}\xi^{\sigma_2\dagger}_{s_2}\left(\sum_{J,m_J}\sum_{l,s}\sum_{l',s'}\frac{u^{l,s,l',s'}_{j\leftarrow j'}(r)}{r}\mathcal{Y}^{m_J}_{l,s,J}(\hat{\boldsymbol{r}})\mathcal{Y}^{m_J\dagger}_{l',s',J}(\hat{\boldsymbol{p}})\right)\xi^{\sigma'_1}_{s'_1}\xi^{\sigma'_2}_{s'_2} \tag{6.10}$$

with[5]

$$u^{l,s,l',s'}_{j\leftarrow j'}(r) \simeq \sqrt{\frac{2}{\pi}\frac{\mu_j}{p_j}}\left[\delta_{jj'}\delta_{ll'}\delta_{ss'}\sin\left(p_j r - l\frac{\pi}{2}\right) + p_j f^{l,s,l',s'}_{j\leftarrow j'} e^{i(p_j r - l\frac{\pi}{2})}\right],$$

where we have omitted the label J in the reduced wave functions.

One can also utilize conservation of parity and charge-conjugation parity to reorganize the expansion (6.10) in the form of a sum over J^{PC} partial waves,

$$\psi^{\sigma_1,\sigma_2,\sigma'_1,\sigma'_2}_{j\leftarrow j',\hat{\boldsymbol{p}}}(\boldsymbol{r}) = \xi^{\sigma_1\dagger}_{s_1}\xi^{\sigma_2\dagger}_{s_2}\left(\sum_{J^{PC},m_J}\sum_{k,k'}\frac{u^{k,k'}_{j\leftarrow j'}(r)}{r}\mathcal{Y}^{m_J}_{l^k_j,s^k_j,J}(\hat{\boldsymbol{r}})\mathcal{Y}^{m_J\dagger}_{l^{k'}_{j'},s^{k'}_{j'},J}(\hat{\boldsymbol{p}})\right)\xi^{\sigma'_1}_{s'_1}\xi^{\sigma'_2}_{s'_2}$$

with

$$u^{k,k'}_{j\leftarrow j'}(r) \simeq \sqrt{\frac{2}{\pi}\frac{\mu_j}{p_j}}\left[\delta_{jj'}\delta_{kk'}\sin\left(p_j r - l^k_j\frac{\pi}{2}\right) + p_j f^{k,k'}_{j\leftarrow j'} e^{i(p_j r - l^k_j\frac{\pi}{2})}\right], \tag{6.11}$$

where we introduced the notation $(l^k_j,\, s^k_j)$ and $(l^{k'}_{j'},\, s^{k'}_{j'})$ to label spin-orbital partial waves coupling to the given J^{PC} in the final and initial channel, respectively.

Notice that the arbitrary multiplicative factor $\sqrt{\frac{2}{\pi}\frac{\mu_j}{p_j}}$ introduced back in Equation (6.3) matches the normalization factor in Equation (6.11). It

[4]Not repeated here, since it is formally the same as Equation (1.15) with appropriate substitutions in the arguments and labels.

[5]See, for example, Equations (15.12) and (15.16) in [86].

is important to realize that this factor comes from the state normalization by energy adopted in the definition of the scattering states (6.4). It is also worth noticing that the commonly used normalization by momentum is unfit to our study. In fact, the different channels share the same center-of-mass energy E but may have different values of the meson-meson momentum $p_j = \sqrt{2\mu_j(E - T_j)}$.

6.2.2 Calculating the S Matrix

The scattering amplitudes can be calculated by direct comparison between the reduced wave functions of the asymptotic scattering states (6.11) and the general parametrization of the asymptotic solutions (6.3) of the diabatic Schrödinger equation above threshold. Note that there are as many independent scattering states as input partial-wave channels, $\sum_{j'} \mathfrak{n}_{j'} = \tilde{n}$ states in total. Unsurprisingly, this number coincides with the degree of degeneracy of a continuum energy E in the diabatic spectrum, meaning that Equations (6.3) and (6.11) are nothing but two different, equivalent ways of representing the solutions of the diabatic Schrödinger equation with energy E. As such, the two expressions can be transformed into one another by a linear change of basis,

$$\sum_h u^k_{j,h}(r)\Gamma^{k'}_{h,j'} = u^{k,k'}_{j\leftarrow j'}(r) \tag{6.12}$$

with $\Gamma^{k'}_{h,j'}$ the change of basis matrix elements.

Inserting (6.3) and (6.11) into (6.12), using Euler's formula for the sine function, and comparing the terms multiplying $e^{\pm ip_j r}$, one obtains

$$\sum_h a^k_{j,h} e^{-i\eta^k_{j,h}} \Gamma^{k'}_{h,j'} = \delta_{jj'}\delta_{kk'}, \tag{6.13a}$$

$$\sum_h a^k_{j,h} e^{i\eta^k_{j,h}} \Gamma^{k'}_{h,j'} = S^{k,k'}_{j\leftarrow j'} \tag{6.13b}$$

where we have introduced the S matrix[6] elements $S^{k,k'}_{j\leftarrow j'}$ using the definition of the scattering amplitude,

$$f^{k,k'}_{j\leftarrow j'} = \frac{S^{k,k'}_{j\leftarrow j'} - \delta_{jj'}\delta_{kk'}}{2ip_j}.$$

The meaning of Equations (6.13) can be made more explicit by momentarily switching to a simplified notation. Let us notice that as j, j' go from 1

[6] More precisely, we are referring to the block of the complete S matrix corresponding to the given J^{PC} quantum numbers.

to n and k, k' go from 1 to $\mathfrak{n}_j, \mathfrak{n}_{j'}$, respectively, each pair (j,k) or (j',k') can take up to $\tilde{n}$ distinct values. Hence, we may label the different values of (j,k), (j',k') using the shorthand $\tilde{\jmath}, \tilde{\jmath}' = 1, 2, \ldots, \tilde{n}$ and simplify Equations (6.13) as

$$\sum_h a_{\tilde{\jmath},h} e^{-i\eta_{\tilde{\jmath},h}} \Gamma_{h\tilde{\jmath}'} = \delta_{\tilde{\jmath}\tilde{\jmath}'}, \tag{6.14}$$

$$\sum_h a_{\tilde{\jmath},h} e^{i\eta_{\tilde{\jmath},h}} \Gamma_{h\tilde{\jmath}'} = S_{\tilde{\jmath}\tilde{\jmath}'}, \tag{6.15}$$

where we have introduced the matrix index notation for the change of basis matrix Γ and the S matrix. Finally, defining the $\tilde{n} \times \tilde{n}$ *Jost matrices*

$$\mathscr{F}^{\pm}_{\tilde{\jmath}h} = a_{\tilde{\jmath},h} e^{\pm i\eta_{\tilde{\jmath},h}}, \tag{6.16}$$

Equations (6.14), (6.15) can be cast in matrix notation as

$$\mathscr{F}^{-}\Gamma = I,$$
$$\mathscr{F}^{+}\Gamma = S$$

and ultimately combined together to give

$$S = \mathscr{F}^{+}(\mathscr{F}^{-})^{-1}. \tag{6.17}$$

This is a general result from multichannel scattering theory, see, for example, Equation (20.18) in [84] where an additional momentum factor is present because of the different choice of normalization adopted in this reference (momentum instead of energy).

Equation (6.17) relates the on-shell S matrix to the Jost matrices (6.16), which in turn can be calculated from the amplitudes and phase shifts obtained from the asymptotic solutions (6.3) of the diabatic Schrödinger equation. Then, the combination of Equations (6.3), (6.16), and (6.17) with a numerical algorithm such as the one described in Appendix C yields a completely nonperturbative numerical calculation of the on-shell S matrix.

6.3 Cross-Sections

From the scattering amplitudes, the total unpolarized cross-section can be calculated using the well-known formula

$$\sigma_{j\leftarrow j'} = \frac{1}{2s_1+1}\frac{1}{2s_2+1}\sum_{\sigma_1,\sigma_2}\sum_{\sigma_1',\sigma_2'}\int \mathrm{d}\hat{\boldsymbol{r}}\left|f^{\sigma_1,\sigma_2,\sigma_1',\sigma_2'}_{j\leftarrow j'}(\hat{\boldsymbol{p}}\cdot\hat{\boldsymbol{r}})\right|^2. \tag{6.18}$$

Inserting (6.7) into (6.18) and imposing J^{PC} conservation yields, after some tedious but straightforward SU(2) algebra,

$$\sigma_{j\leftarrow j'} = \sum_{J^{PC}} \sigma^{J^{PC}}_{j\leftarrow j'}$$

with the J^{PC} partial-wave cross-sections $\sigma^{J^{PC}}_{j\leftarrow j'}$ defined as

$$\sigma^{J^{PC}}_{j\leftarrow j'} = \frac{4\pi(2J+1)}{(2s_1+1)(2s_2+1)} \sum_{k,k'} \left| f^{k,k'}_{j\leftarrow j'} \right|^2.$$

For our theoretical analysis, it is more convenient to work with a scaled J^{PC} cross-section, defined as

$$\begin{aligned} \bar{\sigma}^{J^{PC}}_{j\leftarrow j'} &= \frac{(2s_1+1)(2s_2+1)}{4\pi(2J+1)} p_j^2 \sigma^{J^{PC}}_{j\leftarrow j'} \\ &= \sum_{k,k'} \left| p_j f^{k,k'}_{j\leftarrow j'} \right|^2, \end{aligned}$$

rather than the total cross-section. There are multiple reasons for which this scaled cross-section is preferable:

- it is a dimensionless quantity;
- it is symmetric under $j \leftrightarrow j'$, as per time reversal symmetry;
- its values are bounded by unitarity as $\sum_{j,j'} \bar{\sigma}^{J^{PC}}_{j\leftarrow j'} \leq 1$, where the upper bound can be reached only at the peak of an isolated resonance;
- the scaling factor p_j^2 compensates the kinematical p_j^{-2} behavior of the cross-section, allowing for a more detailed study at low momenta.

As an application of the theoretical formalism developed here, in the remainder of this section we shall study the elastic scaled cross-sections calculated from the spectroscopic diabatic potential from Section 5.1. Specifically, in Subsections 6.3.1 and 6.3.2 we shall examine some open-bottom and open-charm meson-meson scattering processes, respectively.

6.3.1 Open-Bottom

The calculated elastic scaled cross-sections for open-bottom meson-meson scattering with $J^{PC} = (0, 1, 2)^{++}$, 1^{--} and center-of-mass energy up to 10.85 GeV are plotted in Figure 6.2. The enhancements in the calculated cross sections

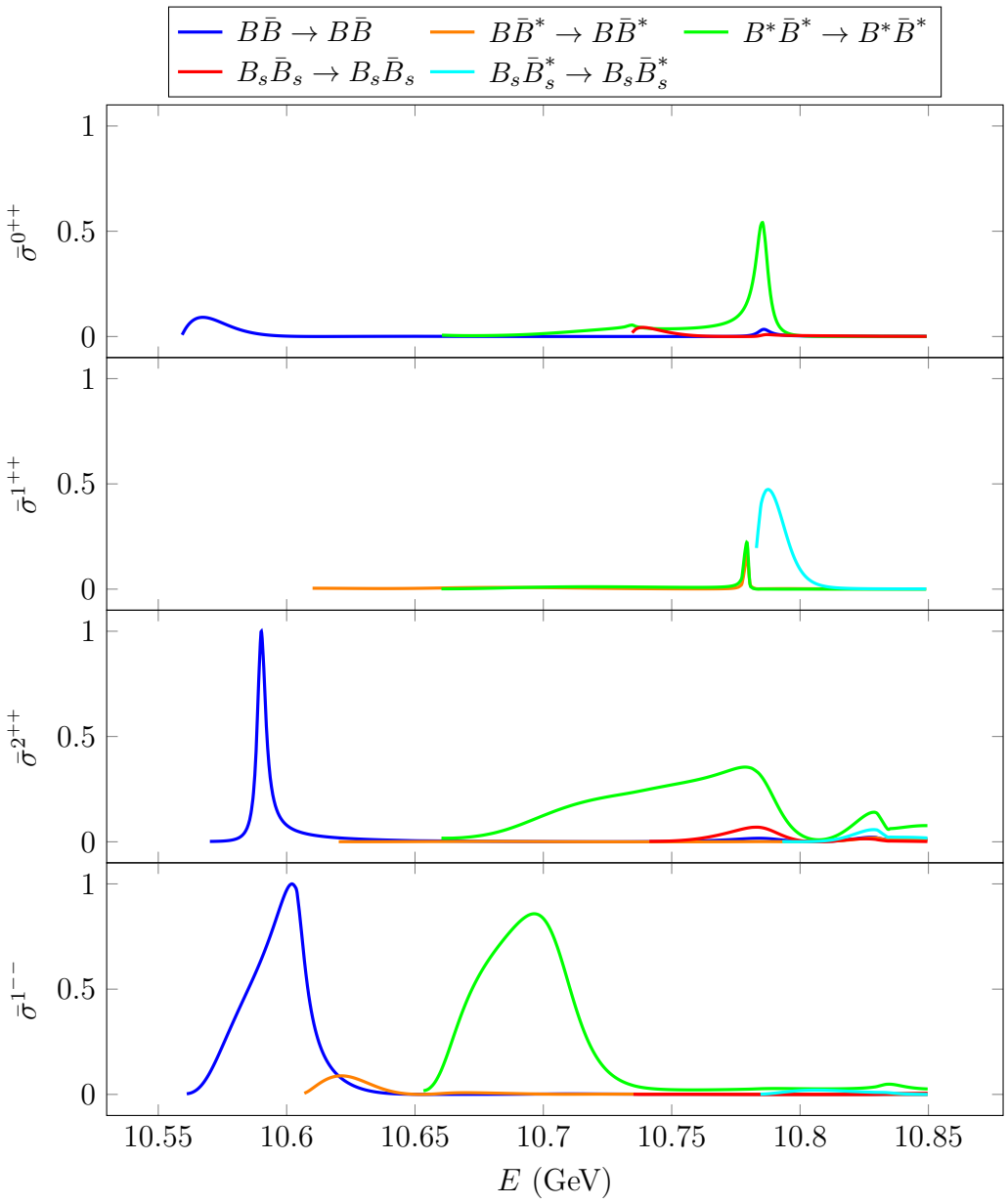

Figure 6.2: Calculated elastic open-bottom scaled cross-sections, $\bar{\sigma}^{J^{PC}}$ with $J^{PC} = (0, 1, 2)^{++}$ and 1^{--}, versus center-of-mass energy.

should be compared with the bound-state spectrum of Tables 5.5 and 5.7, as an independent check of the bound-state approximation, and with candidates in the PDG particle listing of hidden-bottom states [70], when available.

For $J^{PC} = 0^{++}$, there is a peak close below 10.8 GeV, in correspondence with the Fano resonance calculated at 10787.9 MeV. Also in correspondence, the calculated peak is expected to decay more into B^*B^* than other open-bottom channels, as signaled by the peak being higher in the corresponding elastic scattering channel. Hence, this peak corresponds to a quasiconventional $4P$ bottomonium state, and is thus named $\chi_{b0}(4P)$. Apart from this structure, the cross-sections show a small cusp at the $B_s\bar{B}_s$ threshold and a tiny enhancement in the $B\bar{B}$ cross-section at low momenta, the latter due to the presence of the (mostly conventional $3P$ bottomonium) bound state at 10531.7 MeV.

For $J^{PC} = 1^{++}$, there is a narrow peak close below the $B_s\bar{B}_s^*$ threshold, corresponding to the unconventional Fano resonance at 10780.9 MeV, which may be tentatively named $\chi_{b1}(10780)$. This very sharp peak is visible, with equal heights, in both the $B\bar{B}$ and $B^*\bar{B}^*$ channels, which is compatible with the bound-state prediction of the widths in those channels. Right next to this resonance there is an important enhancement in the $B_s\bar{B}_s^*$ cross-section at low momenta. This threshold enhancement is due to the presence of the nearby resonance and may also contain the diluted effect of a quasiconventional $4P$ bottomonium state.

For $J^{PC} = 2^{++}$, there is a Breit-Wigner peak near 10.6 GeV and a wide complex structure stretching from the $B^*\bar{B}^*$ threshold to up above 10.8 GeV, this is, beyond the region of validity of the diabatic approach in the bottom sector. The first structure can be interpreted as a quasiconventional $2F$ bottomonium state, as confirmed by the corresponding Fano resonance calculated at 10589.3 MeV, and is therefore named $\chi_{b2}(2F)$. The complex structure in the $B^*\bar{B}^*$ cross-section may be the result of a coherent sum of many different effects, and has no Fano resonance to be assigned to. In fact, the calculated $\chi_{b2}(4P)$ bound state at 10777.1 MeV goes above the $B_s\bar{B}_s^*$ threshold when mass corrections due to coupling with open thresholds are introduced (see Table 5.5). Notice that the calculated minimum of the cross-sections near 10.8 GeV may signal the coherent superposition of different enhancements, while the threshold cusps at the $B_s\bar{B}_s^*$ threshold indicate a strong interaction between this threshold and the nearby resonances.

For $J^{PC} = 1^{--}$, the two prominent peaks can be put in perfect correspondence with the Fano resonances at 10603.8 and 10700.2 MeV, respectively. The first peak, assigned to a quasiconventional $4S$ bottomonium state, is very close to the experimental $\Upsilon(4S)$ state, with a PDG average mass of 10579.4 ± 1.2 MeV. Notice also that the calculated width to $B\bar{B}$, 22.4 MeV,

is compatible within errors with the total width of $\Upsilon(4S)$, 20.5 ± 2.5 MeV, consistently with the experimental lower limit on its $B\bar{B}$ branching fraction, 96%. The second peak may be dubbed $\Upsilon_1(3D)$, as it is given by a quasiconventional $3D$ bottomonium state. There is no clear experimental candidate at the moment, although it may be put in tentative correspondence with the not-well-established $\Upsilon(10753)$ resonance. Notice the interesting skewing of the two peaks, possibly indicating some mixing between the underlying $4S$ and $3D$ bottomonium states mediated by the diabatic mixing with open-bottom meson-meson pairs.

6.3.2 Open-Charm

The calculated elastic scaled cross-sections for open-charm meson-meson scattering with $J^{PC} = (0, 1, 2)^{++}$, 1^{--} and center-of-mass energy up to 4.1 GeV are plotted in Figure 6.3. Notice that here we have considered the distinct masses between $D^{(*)0}$ and $D^{(*)+}$, which allows us to calculate isospin breaking effects due to the mass differences. This is an important advance with respect to the treatment in [62], where average $D^{(*)}$ masses and effective isospin-zero channels were considered. As in the open-bottom case, the calculated structures give us an independent check of the the bound-state spectrum of Tables 5.6 and 5.8 as well as means for the interpretation of some of the hidden-charm states observed in collider experiments [70].

For $J^{PC} = 0^{++}$, there are two structures close to the $D_s\bar{D}_s$ threshold: a sharp peak in the $D^0\bar{D}^0$ and D^+D^- cross-sections close below it, and an enhancement in the $D_s\bar{D}_s$ one above it. The sharp peak corresponds to the unconventional Fano resonance calculated at 3925.8 MeV. Experimental candidates in this energy region are the quite uncertain $\chi_{c0}(3860)$, with a mass of 3862^{+50}_{-35} MeV, and the $X(3915)$, with a mass of 3921.7 ± 1.8 MeV, under a $J^{PC} = 0^{++}$ assignment of its quantum numbers. However, neither of these two experimental candidates seem to be compatible with the sharpness of the calculated peak (we shall come back to this later on). As for the $D_s\bar{D}_s$ threshold enhancement, it is due to the presence of the unconventional resonance close below threshold. It may also contain the effect of a quasiconventional $2P$ charmonium resonance close above the $D_s\bar{D}_s$ threshold.

For $J^{PC} = 1^{++}$, there are enhancements at the $D^0\bar{D}^{*0}$ and D^+D^{*-} thresholds as well as a soft bump near 3.95 GeV, on the "tail" of these enhancements. The threshold enhancements are caused by the $\chi_{c1}(3872)$ state, the height of the enhancements reflecting its sizable molecular composition. The smaller bump, mostly overshadowed by the threshold enhancements, can be put in correspondence with the quasiconventional $2P$ charmonium resonance calculated in the bound-state approximation to have a mass of

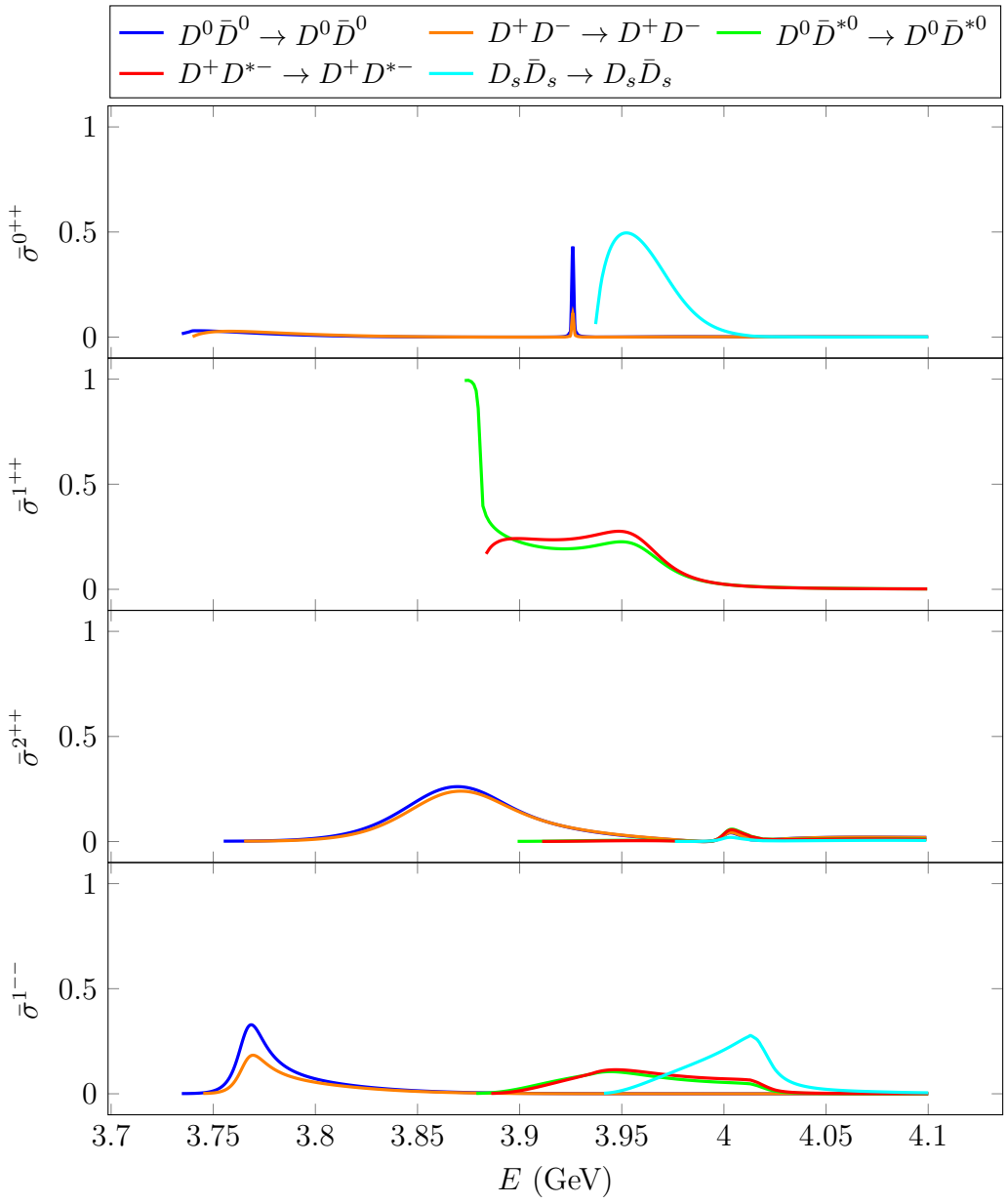

Figure 6.3: Calculated elastic open-charm scaled cross-sections, $\bar{\sigma}^{J^{PC}}$ with $J^{PC} = (0, 1, 2)^{++}$ and 1^{--}, versus center-of-mass energy.

3952.4 MeV and a width of 80.5 MeV. This state, that may be consistently named $\chi_{c1}(2P)$, has no correspondence in the PDG listing of hidden-charm particles, which may be understood given the presumable difficulty of detecting it in the open-charm decay channels due to the big background provided by the threshold enhancements. However, it should be noted that BES III data on $e^+e^- \to \gamma\omega J/\psi$ [79] indicate that a good fit of the $\omega J/\psi$ invariant mass spectrum can be obtained with either two or three peaks. In the three-resonance fitting, along with the $\chi_{c1}(3872)$ and $X(3915)$, there is an additional peak, named $X(3960)$, at 3963.7 ± 5.5 MeV that may be tentatively assigned to the predicted $\chi_{c1}(2P)$. Notice also that in this fitting scenario the width of $X(3915)$ would be smaller than the PDG average value, in accordance instead with the sharp peak calculated in 0^{++} open-charm scattering. More data, as well as a definite assignment of the J^{PC} quantum numbers of $X(3915)$ are needed in order to confirm or refute this prescription.

For $J^{PC} = 2^{++}$, there is a very broad peak located near 3.87 GeV and a narrower peak close to 4 GeV. The broad peak may be assigned to a quasiconventional $2P$ charmonium state, although such assignment is not entirely clear due to the bound-state approximation breaking down for this state when corrections are included (see Table 5.6). The narrower peak, on the other hand, is in almost perfect correspondence with the quasiconventional $1F$ charmonium state, for which we label it $\chi_{c2}(1F)$. From the experimental point of view there are two candidates, the $X(3915)$ under a $J^{PC} = 2^{++}$ assignment and the $\chi_{c2}(3930)$, however, neither of them seems to be compatible with the broad peak.

For $J^{PC} = 1^{--}$, there is a Breit-Wigner peak near 3.77 GeV as well as some more complex structures in between 3.9 and 4.05 GeV. The first peak can be associated with the quasiconventional $1D$ charmonium resonance obtained from the bound-state approximation, with a mass of 3766.8 MeV and a width of 21.8 MeV. This state, which may be called $\psi_1(1D)$, can be put in correspondence with the experimental $\psi(3770)$ state, with a mass of 3773.7 ± 0.4 MeV and a width of 27.2 ± 1.0 MeV. The soft, broad enhancement in the $D^0\bar{D}^{*0}$ and D^+D^{*-} cross sections between 3.9 and 4.05 GeV may have to do with the complicated interaction of the $3S$ and $2D$ charmonium states with the $D_s\bar{D}_s$ and $D^0\bar{D}^0$ thresholds and with each other. The complexity of this energy region can be also inferred from the cusps showed by the $D^0\bar{D}^{*0}$, D^+D^{*-}, and $D_s\bar{D}_s$ cross-sections at the $D^{*0}\bar{D}^{*0}$ threshold.

Conclusions

We have pursued a comprehensive study of hidden-flavor heavy mesons for energies below and above open-flavor meson-meson thresholds by means of various theoretical schemes. In the first part of this study, we have used the BO approximation with potentials derived from quenched lattice QCD to analyze quarkonium and quarkonium hybrids. In the second part, we have adapted the diabatic framework from molecular physics to strong interactions in order to have a description of heavy mesons, made of quark-antiquark and meson-meson components, based on unquenched lattice QCD studies of string breaking. Specifically, here are the conclusions of each chapter:

1. We have reviewed the BO approximation and parametrized the quarkonium and quarkonium hybrid potentials obtained in quenched lattice QCD. We have calculated the spectrum of quarkonium states with phenomenological values of the parameters, then included some spin-dependent corrections, then showed that the experimental low-lying spectrum of heavy mesons is well described in terms of quarkonium states. We have also calculated the masses of the lowest bottomonium and charmonium hybrid states using the same values of the parameters as in the quarkonium potential, without adding any new free parameter.

2. We have reviewed the derivation of the usual dipole transition operator for radiative quarkonium transitions from the QED interaction Hamiltonian. We have briefly reviewed the LWL and NR approximations and their conditions of validity. Since these conditions may not be met by some radiative decays between quarkonium states, we have lifted the LWL and NR approximations and derived more general formulae for the EM transition operator. We have finally shown, through a short review of a radiative decays between charmonium states, that the results from these general formulae are very sensitive to the details of the quarkonium wave functions, and hence may serve as a stringent test of different phenomenological models when comparing with data.

3. We have developed QPC models for strong decays to open-flavor meson-meson pairs respecting the symmetries of the BO approximation. We have shown that the quantum numbers of the BO potential of the decaying state, associated with the hadronic medium, may be used to determine the quantum numbers of the created light quark pair. Specifically, in the quarkonium case, the hadronic medium is in its ground state with vacuum-like quantum numbers, which corresponds to the customary $^3P_0$ QPC model extensively used in phenomenological studies. As for the lowest quarkonium hybrid, whose hadronic medium has the quantum numbers of the ground state gluelump, the corresponding QPC model has quantum numbers $^1P_1$. Thus, we have reviewed the $^3P_0$ model for quarkonium and developed the $^1P_1$ model for the lowest quarkonium hybrid.

4. We have used the diabatic representation of BO, first introduced in molecular and atomic physics, to develop a phenomenological framework for the description of heavy mesons made of quark-antiquark and open-flavor meson-meson components. We have shown that the dynamics is governed by a multichannel Schrödinger equation that, particularizing to a specific set of J^{PC} quantum numbers, can be reduced to a radial form. Then, we have used the static energies calculated in unquenched lattice QCD to infer the form of the radial potential associated to the mixing between quark-antiquark and meson-meson. It turns out that this potential is significant only near the crossing between the quarkonium potential and the threshold mass.

5. We have examined the spectrum of bound states obtained in the diabatic framework, with masses below the lowest open-flavor meson-meson threshold. Then we have briefly discussed the difficulties in solving the diabatic Schrödinger equation for energies above threhsold, and introduced a bound state approximation in which coupling to the open threshold is initially neglected. Then, we have shown that the reintroduction of the coupling with the meson-meson continua transforms the approximated bound states in Fano resonances, associated to heavy mesons decaying to open-flavor meson-meson pairs. We have then calculated a phenomenological spectrum of bottomoniumlike and charmoniumlike states and discussed the limitations of the bound state approximation.

6. We have overcome the limitations of the bound-state approximation by developing a nonperturbative scattering formalism for open-flavor meson-meson pairs. We have shown that the solutions of the diabatic

Schrödinger equation for energies above threshold are naturally interpreted as stationary scattering states. We have then connected these solutions with the usual representation of scattering states in terms of an incoming plane wave plus a spherical wave multiplied by the scattering amplitude. In this way, we have derived a nonperturbative scheme for calculating the on-shell S matrix directly from the diabatic potential matrix. Finally, we have carried out a phenomenological analysis of elastic open-bottom and open-charm cross sections in comparison with the calculated Fano resonances and with data. The resulting physical picture of heavy mesons below and above threshold corresponds to a spectrum of (quasi)conventional quarkonium states, plus unconventional states lying close to some open-flavor meson-meson thresholds. We have also argued that an unconventional state with mass close below some threshold causes an enhancement of the low-momentum cross section in the corresponding channel, which may overshadow quasiconventional resonances lying close by.

From a phenomenological point of view, there are two well-established experimental unconventional states that provide ideal case studies for, respectively, the BO approximation and the diabatic framework developed here. On the one hand the $\Upsilon(10860)$, whose mass and decay properties are compatible with those of a bottomonium state mixing with the lowest bottomonium hybrid, as calculated within a BO framework equipped with consistent QPC models. On the other hand, the $\chi_{c1}(3872)$, which can be interpreted in the diabatic framework as a loosely bound $D^0\bar{D}^{*0}$ state with a compact $c\bar{c}$ core, as shown by a phenomenological calculation with an effective value of the energy gap.

It should be pointed out that the diabatic framework is perfectly general in the sense that it can also be applied for a description of heavy-meson systems made of quarkonium and quarkonium hybrid components, such as the $\Upsilon(10860)$. The current limitation preventing this is the lack of lattice QCD input to derive the form of the mixing potential in such systems. Furthermore, the diabatic treatment is also suited for systems containing quarkonium, quarkonium hybrid, and meson-meson components as well.

Hence, we conclude that a completely unified study of hidden-flavor mesons below and above open-flavor thresholds is possible by means of the diabatic approach. It is important to notice that the diabatic potential matrix treats on equal grounds the potentials of different channels (e.g.: quarkonium, meson-meson, hybrid,...) as well as the mixing potentials between them, so that the descriptions below and above threshold are connected seamlessly.

Resumen

Objetivos

Libertad asintótica y confinamiento son sin duda las características más relevantes de la Cromodinámica Cuántica (QCD), la teoría cuántica de campos de quarks y gluones, basada en la simetría gauge de color, universalmente aceptada como teoría de las interacciones fuertes [1-3]. Libertad asintótica significa que la teoría se aproxima a una teoría sin interacción en el límite de altas energías, lo que permite un tratamiento perturbativo de la misma en dicho régimen. Ello permite derivar, a partir del lagrangiano de la QCD, expresiones analíticas para describir las interacciones a alta energía. Confinamiento o, en forma más precisa, confinamiento de color, pues implica que todos los estados observables son de color neutro, es un fenómeno no perturbativo, lo que impide un cálculo analítico para las interacciones a baja energía, como las que confinan a los quarks en hadrones. Ello hace que, para una descripción hadrónica basada en QCD, sea necesario el desarrollo de métodos no perturbativos aproximados. En este sentido, los mesones pesados con sabor oculto, que contienen, entre otras posibles componentes, un quark Q y su antiquark $\bar{Q}$ cuyas masas son grandes comparadas con la escala de energía característica de QCD, proporcionan un laboratorio ideal para la validación de dichos métodos, debido a las simplificaciones en su descripción derivadas de la gran masa de quark y antiquark [4].

El objetivo final de esta tesis ha sido el desarrollo de un método no perturbativo aproximado para el estudio de los mesones pesados por debajo y por encima del umbral de energía para la producción de pares mesón-mesón con sabor abierto (*open-flavor meson-meson pairs*), es decir, de pares donde cada mesón está formado por un quark pesado o ligero y un antiquark ligero o pesado, respectivamente.

Para la consecución de este objetivo final ha sido necesario el cumplimiento de los siguientes objetivos intermedios:

- la descripción consistente del espectro del quarkonio (estados ligados de $Q\bar{Q}$ donde Q es un quark pesado, $Q \equiv b$ (bottom) o c (charm)) y del

quarkonio híbrido (estados ligados de $Q\bar{Q}g$ siendo g un gluon);

- el cálculo completo detallado de las transiciones radiativas electromagnéticas entre estados del quarkonio, más allá de las expresiones aproximadas que suelen encontrarse en la literatura;

- la construcción de un modelo fenomenológico para el cálculo de las anchuras de desintegración de los estados del quarkonio, y del quarkonio híbrido, a pares mesón-mesón de sabor abierto;

- el desarrollo de un formalismo semifenomenológico para el tratamiento de mesones pesados formados por componentes $Q\bar{Q}$ y mesón-mesón de sabor abierto. Este formalismo, que ha requerido el desarrollo de técnicas analíticas y numéricas para resolver las ecuaciones dinámicas resultantes, está basado tanto en la fenomenología como en los estudios de QCD en la red incluyendo configuraciones de $Q\bar{Q}$ y de mesón-mesón de sabor abierto, que muestran el denominado fenómeno de rotura de la cuerda (*string breaking*).

Metodología

Revisión de Metodologías Existentes

QCD en la red (LQCD), probablemente el método no perturbativo aproximado mejor fundamentado, se basa en la discretización de la acción (continua) de QCD en forma invariante gauge [5-12]. Durante muchos años, en la práctica, para la realización técnica de los cálculos, ha sido necesario recurrir a aproximaciones tales como la utilización de masas no físicas para el pion, la no consideración de los quarks del mar, etc. Hoy en día, los avances técnicos y el aumento constante de la potencia de cálculo de los computadores, ha permitido ir eliminando gradualmente algunas de estas aproximaciones [13-25].

Un método alternativo es la modelización sistemática de QCD a bajas energías mediante el uso de teorías efectivas de campos (EFTs) [26]. Algunas de éstas, como QCD no relativista (NRQCD) [27-36] utilizan campos (efectivos) de quarks pesados en su formulación, mientras que otras utilizan campos hadrónicos [37-42]. Cabe apuntar que, aunque la mejora sistemática de los cálculos de EFT suele implicar un gran aumento del número de parámetros, la capacidad de predicción puede mantenerse mientras haya suficientes datos experimentales y resultados de LQCD para fijar su valor.

Otro método que también se ha usado para realizar cálculos no perturbativos del espectro y las propiedades de los hadrones, es el basado en reglas de suma de QCD, véanse [44, 45] y sus referencias. Este método utiliza identidades entre las funciones de correlación para conectar cantidades medibles, como las masas, anchuras y factores de forma de los hadrones, con las fundamentales de QCD, como la constante de acoplamiento fuerte y las masas de los quarks. Hay que tener en cuenta que, si bien las reglas de suma son en principio exactas, en la práctica se requieren varias aproximaciones y truncamientos para la obtención de resultados.

En cuanto al cálculo específico de estados ligados en QCD, éste puede llevarse formalmente a cabo de forma exacta mediante el uso de la ecuación de Bethe-Salpeter [46]. Sin embargo, su resolución presenta dificultades formidables (véase [47], por ejemplo). Como alternativa, teniendo en cuenta el éxito de los modelos no relativistas de quarks, que utilizan la ecuación de Schrödinger y potenciales estáticos de interacción entre quarks, para la descripción hadrónica [48, 49], se puede intentar reducir la complejidad de la ecuación de Bethe-Salpeter utilizando la aproximación estática y el límite no relativista [50]. Estas dos simplificaciones, que pueden ser válidas para el caso mesones pesados, permiten reducir la ecuación de Bethe-Salpeter a una ecuación de Schrödinger en que la interacción quark-antiquark se describe mediante un potencial efectivo, que puede determinarse de forma invariante gauge mediante el formalismo del "loop" Wilson [51, 52]. Concretamente, este potencial se ha calculado *ab initio* en LQCD utilizando la aproximación de Born-Oppenheimer (BO) para mesones pesados [53, 54]. En esta aproximación, basada en que la masa de los quarks pesados es mucho mayor que la escala de energía característica de QCD, el potencial quark-antiquark se calcula a partir de los niveles de energía de los campos estacionarios de gluones y quarks ligeros en presencia de fuentes de color estáticas (los quarks pesados).

La Approximación de Born-Oppenheimer

La suposición fundamental en la aproximación de BO es que los componentes de un sistema físico pueden clasificarse distintivamente como "pesados" y "ligeros" sobre la base de alguna escala de energía, de manera que la dinámica de los campos ligeros puede resolverse despreciando el movimiento asociado a los grados de libertad pesados. La idea física detrás de esta aproximación es que la escala de tiempo para la evolución de los campos ligeros es tan corta que, en comparación, los grados de libertad pesados pueden tratarse como si estuvieran quietos. Entonces, una vez que los campos ligeros se han integrado en este límite estático, el movimiento de los grados de libertad pesados se determina a partir de una ecuación de Schrödinger no relativista

con potenciales efectivos que encierran toda la información sobre la dinámica de los campos ligeros.

En las moléculas atómicas, donde los núcleos pesan varios miles de veces más que los electrones, los núcleos se tratan como grados de libertad pesados, mientras que los electrones y los fotones constituyen los campos ligeros. En los sistemas de quarks pesados, la distinción entre "pesado" y "ligero" la proporciona la escala de energía QCD, Λ_{QCD}, que es la escala de energía asociada al campo de gluones. Así, los sabores de quarks pesados, charm (c) y bottom (b), cuya masa m_Q es mucho mayor que Λ_{QCD}, pueden considerarse grados de libertad pesados. Por otro lado, los gluones (g) y los sabores de quarks ligeros, up (u), down (d) y strange (s), pueden ser tratados como campos ligeros.

En la aproximación de BO, un estado de mesón pesado $|\psi\rangle$ es la solución de

$$H\,|\psi\rangle = E\,|\psi\rangle$$

donde E es la energía del estado. El hamiltoniano H es separable en la forma

$$H = K_{Q\bar{Q}} + H_{\mathrm{light}}^{(Q\bar{Q})}$$

con $K_{Q\bar{Q}}$ la energía cinética de los quarks pesados y $H_{\mathrm{light}}^{(Q\bar{Q})}$ el hamiltoniano residual que contiene la dinámica de los campos ligeros y su interacción con $Q\bar{Q}$. En el sistema de referencia del centro de masas de $Q\bar{Q}$, E coincide con la masa M del estado del mesón, y el par $Q\bar{Q}$ puede describirse por su posición relativa $\boldsymbol{r}$ o por su momento relativo $\boldsymbol{p}$.

En el límite estático, que corresponde a despreciar la energía cinética de $Q\bar{Q}$, $\boldsymbol{r}$ deja de ser una variable dinámica, convirtiéndose en un parámetro constante en el hamiltoniano residual. Para dejar claro que entonces el hamiltoniano residual corresponde a un hamiltoniano para los campos ligeros en presencia de $Q\bar{Q}$ estático situado en la posición relativa $\boldsymbol{r}$, se renombra $H_{\mathrm{light}}^{(Q\bar{Q})}$ como $H_{\mathrm{light}}^{\mathrm{static}}(\boldsymbol{r})$.

En este límite estático, la dinámica de los campos ligeros está completamente determinada a partir de la solución de la ecuación secular

$$H_{\mathrm{light}}^{\mathrm{static}}(\boldsymbol{r})\,|\zeta_i(\boldsymbol{r})\rangle = V_i(\boldsymbol{r})\,|\zeta_i(\boldsymbol{r})\rangle$$

con i denotando los estados, fundamental ($i = 0$) y excitado ($i = 1, 2, \dots$). Los valores propios $V_i(\boldsymbol{r})$, correspondientes a los niveles de energía estáticos de los campos ligeros, pueden determinarse *ab initio* en LQCD [53].

El movimiento de $Q\bar{Q}$, despreciado en el límite estático, puede incorporarse reintroduciendo el operador de energía cinética y desarrollando el estado del

mesón pesado $|\psi\rangle$ en términos de una base de estados para los campos ligeros. Un posible desarrollo es el denominado desarrollo adiabático

$$|\psi\rangle = \sum_j \int \mathrm{d}\boldsymbol{r}' \psi_j(\boldsymbol{r}') \, |\boldsymbol{r}'\rangle \, |\zeta_j(\boldsymbol{r}')\rangle$$

donde $|\boldsymbol{r}'\rangle$ es el estado de $Q\bar{Q}$ en la posición $\boldsymbol{r}'$ y $\psi_j(\boldsymbol{r}')$ son las funciones de onda adiabáticas asociadas a las distintas componentes mesónicas (o canales) j.

Nótese que la base de estados para los campos ligeros en el desarrollo adiabático, $\{|\zeta_j(\boldsymbol{r}')\rangle\}_j$, se calcula en la misma posición de los quarks pesados, $\boldsymbol{r}'$. Esto hace que sea el desarrollo más natural en la aproximación adiabática, es decir, en la situación idealizada (correspondiente al límite $m_Q \to \infty$) en la que los campos ligeros se ajustan instantáneamente al movimiento de $Q\bar{Q}$, de ahí su nombre.

Se puede demostrar que las funciones de onda adiabáticas $\psi_j(\boldsymbol{r}')$ satisfacen la ecuación de tipo Schrödinger

$$\sum_j \left(-\frac{1}{2\mu} [(I\boldsymbol{\nabla} + \boldsymbol{\tau}(\boldsymbol{r}))^2]_{ij} + \delta_{ij}(V_i(\boldsymbol{r}) - E) \right) \psi_j(\boldsymbol{r}) = 0$$

donde los niveles de energía estáticos $V_i(\boldsymbol{r})$ desempeñan el papel de potenciales efectivos para los canales correspondientes y $\boldsymbol{\tau}(\boldsymbol{r})$ son acoplamientos no adiabáticos (NACTs) entre los diferentes canales. Estos acoplamientos complican mucho la resolución de la ecuación tipo Schrödinger, por lo que habitualmente son despreciados en la aproximación BO para mesones pesados (véase, por ejemplo, [54]). En esta aproximación de canal único, la ecuación factoriza como

$$-\frac{1}{2\mu}\nabla^2 \psi_i(\boldsymbol{r}) + (V_i(\boldsymbol{r}) - E)\psi_i(\boldsymbol{r}) = 0$$

para $i = 0, 1, \ldots$, es decir, una ecuación de Schrödinger para cada componente de la función de onda adiabática $\psi_i(\boldsymbol{r})$ en su potencial BO $V_i(\boldsymbol{r})$.

El potencial correspondiente al estado fundamental de los campos ligeros, que ha sido calculado en LQCD con sólo gluones como campos ligeros [22], puede parametrizarse como un potencial de Cornell

$$V_0(r) = V_{\mathrm{C}}(r) = \sigma r - \frac{\chi}{r} + E_0$$

siendo $r = |\boldsymbol{r}|$ la distancia entre $Q\bar{Q}$, σ la denominada tensión de la cuerda (*string tension*), χ la intensidad de la interacción culombiana de color y E_0 una constante, que en general puede depender del sabor del quark pesado.

Este potencial, que es atractivo a cortas distancias, debido a la interacción culombiana, asociada al intercambio de un gluon, y confinante (confinamiento lineal) a largas distancias, se asocia a la configuración convencional del quarkonio, estudiada ampliamente en los modelos de quarks no relativistas [48, 49].

Los potenciales correspondientes a los estados excitados de los campos ligeros también han sido calculados en LQCD con sólo gluones como campos ligeros [53, 67] y se asocian a configuraciones del quarkonio híbrido. Se ha considerado exclusivamente el potencial híbrido de menor exitación, que en la Referencia [54] se ha parametrizado como

$$V_1(r) = \begin{cases} \frac{0{,}24}{r_0^3} r^2 + \frac{0{,}11}{r} + \frac{2{,}8}{r_0} + E_0, & \text{if } r < r_*, \\ \sigma r \sqrt{1 + \frac{11\pi}{6\sigma r^2}} + E_0, & \text{if } r \geq r_*, \end{cases}$$

donde E_0 es la misma constante aditiva que aparecía en el potencial de Cornell, $r_0 \approx 0{,}5$ fm y $r_* = 2r_0$ es la distancia en la que se conecta la parametrización para distancias cortas e intermedias (primera línea a la derecha en la expresión anterior) con la parametrización para largas distancias (segunda línea a la derecha en la expresión anterior). Este potencial híbrido muestra una interacción de Coulomb repulsiva a cortas distancias, como cabía esperar a partir de un modelo de quarks en que tanto el par $Q\bar{Q}$ como el gluon constituyente están en un estado octete de color. Por otro lado, a grandes distancias se comporta de manera muy similar a un potencial de cuerda (*string potential*), como se espera de los modelos denominados de tubo de flujo (*flux tube models*) [68].

Calculo de Anchuras de Desintegración

Las funciones de onda calculadas en la aproximación BO pueden utilizarse para calcular las anchuras de desintegración de los estados del quarkonio y del quarkonio híbrido. En esta tesis se han analizado desintegraciones radiativas electromagnéticas con emisión de un solo fotón y desintegraciones fuertes a pares mesón-mesón con sabor abierto.

El análisis de estas desintegraciones radiativas es importante en el sentido de que como las interacciones electromagnéticas son bien conocidas y manejables mediante la teoría cuántica de campos Electrodinámica Cuántica (QED), cabe esperar que las anchuras de desintegración calculadas se vean afectadas exclusivamente por la incertidumbre en la descripción aproximada de los estados, lo que permite discriminar entre distintas descripciones.

Las anchuras de desintegración se calculan a partir de las amplitudes de transición. La amplitud de transición para una desintegración radiativa

$A \to B\gamma$, donde A y B epresentan los estados inicial y final del quarkonio, respectivamente, y γ un fotón, puede calcularse usando un modelo de emisión elemental en que el fotón es emitido por el quark o el antiquark actuando el antiquark o el quark restante como espectador. Esta amplitud de transición puede calcularse perturbativamente a partir del hamiltoniano de interacción de QED

$$H_{\mathrm{QED}}^{\mathrm{int}} = \int \mathrm{d}\boldsymbol{x} A_\mu(\boldsymbol{x}, t) j^\mu(\boldsymbol{x}, t),$$

que acopla la corriente electromagnética del quark (o antiquark)

$$j^\mu(\boldsymbol{x}, t) = e\bar{q}(\boldsymbol{x}, t)\gamma^\mu q(\boldsymbol{x}, t),$$

con el campo electromagnético A_μ.

Más concretamente, a partir de este hamiltoniano de interacción se puede derivar un operador de transición entre los estados inicial y final del quarkonio, que puede ser utilizado junto con las funciones de onda correspondientes a dichos estados, para calcular la amplitud de transición.

El operador de transición puede reducirse a una forma simplificada, habitualmente utilizada en la literatura, mediante la aproximación dipolar que, de hecho, consiste en dos aproximaciones separadas: la aproximación de longitud de onda larga para el fotón emitido y la aproximación no relativista para las corrientes de quark y antiquark. Sin embargo, estas aproximaciones no siempre son válidas, por lo que se ha realizado el cálculo completo, no simplificado, para lo cual ha sido necesaria la utilización del álgebra de momento angular y la introducción de varias sumas sobre estados intermedios del quarkonio.

En cuanto a las desintegraciones fuertes a un par mesón-mesón con sabor abierto, hay que subrayar que son excepcionalmente difíciles de calcular a partir de QCD. Nótese, sin embargo, que el cálculo de la anchura de estas desintegraciones es extremadamente importante, ya que se espera que sean las dominantes para los estados del quarkonio y del quarkonio híbrido cuando estén permitidas cinemáticamente. De hecho, la mayoría de los mesones pesados se descubre experimentalmente a partir de los productos de su desintegración.

Dado que los potenciales obtenidos de LQCD con sólo gluones carecen de información sobre la dinámica de los campos de quarks y antiquarks ligeros, las desintegraciones a pares mesón-mesón de sabor abierto tienen que calcularse utilizando algún modelo de desintegración. A este respecto, cabe esperar que la desintegración de un estado inicial de quarkonio o de quarkonio híbrido A a un par final de mesones de sabor abierto BC se produzca a partir de la creación de un par de quark-antiquark ligeros en el medio hadrónico y su posterior recombinación con el quark y antiquark pesados para dar lugar al mesón-mesón final.

Utilizando una aproximación de BO, se puede suponer que los números cuánticos del par quark-antiquark ligero creado son los mismos que los del medio hadrónico en el que tiene lugar la desintegración, que puede identificarse con la configuración BO del estado inicial. Esta suposición, junto con la hipótesis razonable de que la desintegración está dominada por los valores más bajos posibles del momento angular total, fija los números cuánticos del modelo de creación de pares. De esta forma, estos modelos para las desintegraciones de los estados del quarkonio y del estado fundamental del bottomonio híbrido pueden construirse y ser comparados de forma consistente.

El Esquema Diabático

La validez de la aproximación BO de canal único no debe darse por supuesta porque $m_Q \gg \Lambda_{\mathrm{QCD}}$, ya que los NACTs pueden no ser despreciables. De hecho, la aproximación de canal único puede considerarse razonable sólo mientras la función de onda no tenga un solapamiento significativo con los NACTs. Esta condición puede cumplirse para el quarkonio y el quarkonio híbrido con potenciales de LQCD con sólo gluones como campos ligeros, pero deja de hacerlo cuando se utilizan potenciales de LQCD que incluyen a gluones y quarks-antiquarks ligeros. En este caso los potenciales muestran una mezcla entre una configuración de $Q\bar{Q}$ y otra de mesones de sabor abierto debida al fenómeno de rotura de la cuerda. Como consecuencia, los acoplamientos no adiabáticos en la ecuación de Schrödinger no pueden despreciarse, y es preciso resolver el sistema completo de ecuaciones acopladas. Sin embargo, esto no es práctico por al menos dos razones: en primer lugar, la conexión entre los acoplamientos no adiabáticos y LQCD no es directo; en segundo lugar, las componentes de la función de onda adiabática no están asociadas a una configuración bien definida, sino más bien a una mezcla de $Q\bar{Q}$ y mesón-mesón donde los porcentajes de la mezcla dependen de la coordenada $\boldsymbol{r}$.

Estas dificultades pueden obviarse utilizando la expansión diabática para el estado del mesón pesado:

$$|\psi\rangle = \sum_j \int \mathrm{d}\boldsymbol{r}' \widetilde{\psi}_j(\boldsymbol{r}', \boldsymbol{r}_0) \, |\boldsymbol{r}'\rangle \, |\zeta_j(\boldsymbol{r}_0)\rangle \, .$$

En esta representación, los mesones pesados compuestos por $Q\bar{Q}$ y pares mesón-mesón de sabor abierto se describen mediante soluciones de la ecuación diabática de Schrödinger

$$\sum_j \left(-\frac{\nabla^2}{2\mu}\delta_{ij} + V_{ij}(\boldsymbol{r}, \boldsymbol{r}_0) - E\delta_{ij} \right) \widetilde{\psi}_j(\boldsymbol{r}, \boldsymbol{r}_0) = 0$$

con $V_{ij}(\boldsymbol{r}, \boldsymbol{r}_0)$ la matriz de potencial diabático, cuya forma puede inferirse a partir de los potenciales y el ángulo de mezcla calculados en LQCD.

En concreto, los elementos diagonales de la matriz de potencial diabático vienen dados por el potencial de Cornell para la componente de quarkonio y por las masas umbrales para las componentes mesón-mesón. En cuanto a los elementos matriciales no diagonales, correspondientes a la mezcla entre quarkonio y mesón-mesón, un análisis de los estudios exploratorios de rotura de la cuerda realizados en LQCD incluyendo gluones y quarks-antiquarks ligeros [15, 17] muestra que el potencial de mezcla es de la forma general

$$V_{0i}(r) = -\frac{\Delta_Q}{2} f\left(\frac{V_{\mathrm{C}}(r) - T_i}{\Lambda}\right)$$

donde $V_{\mathrm{C}}(r)$ es el potencial de Cornell, T_i la masa del umbral i mesón-mesón, Δ_Q y Λ la intensidad efectiva y la escala de energía de la mezcla respectivamente y $f(x)$ una función positiva y par, con un máximo absoluto $f(0) = 1$, y que se anula para $|x| \gg 1$.

Las soluciones de la ecuación diabática de Schrödinger para energías por debajo del umbral más bajo de mesón-mesón representan estados ligados. Para energías muy por debajo del umbral, las componentes mesón-mesón apenas son relevantes y las soluciones correspondientes son simplemente estados del quarkonio. Sin embargo, para energías más cercanas al umbral, las componentes mesón-mesón pueden aparecer como componentes moleculares gracias a la mezcla diabática inducida por la rotura de la cuerda.

Para energías por encima de uno o más umbrales mesón-mesón, las soluciones de la ecuación diabática de Schrödinger poseen algunas componentes que oscilan indefinidamente. Estas componentes no son normalizables, por lo que su interpretación como funciones de onda de un estado de mesón pesado no es sencilla. Para tratar este problema, se puede utilizar una aproximación de estado ligado en la que, en una primera etapa, se desprecian los potenciales de mezcla con umbrales abiertos. Luego, utilizando un procedimiento debido a Fano [83], se puede tener en cuenta el acoplamiento entre los estados ligados aproximados y el continuo de estados mesón-mesón. Como resultado, los estados ligados aproximados adquieren una corrección de masa y una anchura de desintegración, convirtiéndose así en resonancias. Estas resonancias pueden entonces asociarse con mesones pesados por encima del umbral, que se desintegran a pares mesón-mesón a través del mecanismo de rotura de la cuerda.

Un tratamiento más completo de los mesones pesados por encima del umbral, que corrige las deficiencias la aproximación de estado ligado, se puede realizar a partir del estudio de la dispersión mesón-mesón. De hecho, el

comportamiento oscilante de las componentes de la función de onda asociadas a los umbrales mesón-mesón abiertos es bien conocido analíticamente. Estas funciones de onda, de hecho, representan la corriente libre de pares mesón-mesón que se dispersan a través de su mezcla con $Q\bar{Q}$. Su forma asintótica general viene dada por

$$u^k_{j,h}(r) \simeq \sqrt{\frac{2}{\pi}\frac{\mu_j}{p_j}} i^{l^k_j} a^k_{j,h} \sin\Big(p_j r - l^k_j \frac{\pi}{2} + \eta^k_{j,h}\Big)$$

donde j etiqueta los canales abiertos, k la onda parcial en cada canal, h las soluciones independientes con la misma energía, $a^k_{j,h}$ es un coeficiente, $\eta^k_{j,h}$ un desfasaje, l^k_j el momento angular orbital y $p_j = \sqrt{2\mu_j(E - T_j)}$ el momento del mesón-mesón siendo E la energía en el sistema centro de masas.

Estas soluciones asintóticas pueden transformarse en la representación habitual de los estados estacionarios de dispersión en términos de las amplitudes de dispersión. Esto permite expresar la matriz S en términos de los coeficientes $a^k_{j,h}$ y los desfasajes $\eta^k_{j,h}$ como

$$S = \mathscr{F}^+(\mathscr{F}^-)^{-1}$$

con $\mathscr{F}^\pm$ la matriz de Jost cuyos elementos están definidos por

$$\mathscr{F}^\pm_{\tilde{j}h} = a_{\tilde{j},h} e^{\pm i\eta_{\tilde{j},h}}$$

donde $\tilde{j}$ es una abreviatura de la doble etiqueta (j, k).

Este esquema completamente no perturbativo permite calcular la matriz S directamente a partir de la matriz de potencial diabático, que está relacionada con los niveles de energía estáticos en LQCD, sin ninguna aproximación adicional. Entonces, los mesones pesados por encima del umbral se identifican naturalmente con los picos en las secciones eficaces mesón-mesón calculadas.

Conclusiones

En esta tesis se ha realizado un estudio sistemático de los mesones pesados de sabor oculto, para energías por debajo y por encima de los umbrales mesón-mesón de sabor abierto, por medio de varios esquemas teóricos. En la primera parte de este estudio, se ha utilizado la aproximación BO con potenciales derivados de LQCD con sólo gluones como campos ligeros para analizar el quarkonio y el quarkonio híbrido. En la segunda parte, se ha adaptado el formalismo diabático de la física molecular a las interacciones fuertes, lo que ha permitido utilizar los estudios del fenómeno de rotura de la

cuerda, realizados en LQCD incluyendo gluones y quarks-antiquarks ligeros, para describir los mesones pesados compuestos de quark y antiquark pesados y de mesón-mesón. En concreto, las conclusiones de cada capítulo son las siguientes:

1. Se ha revisado la aproximación BO y se han parametrizado los potenciales para quarkonio y quarkonio híbrido obtenidos en LQCD con sólo gluones como campos ligeros. Se ha calculado el espectro de los estados de quarkonio con valores fenomenológicos de los parámetros, se han incluido algunas correcciones dependientes del espín, y se ha mostrado que el espectro experimental de baja excitación de los mesones pesados está bien descrito en términos de estados de quarkonio. También se han calculado las masas de los estados más bajos del bottomonio híbrido y del charmonio híbrido utilizando los mismos valores de los parámetros y sin añadir ningún parámetro libre nuevo.

2. Se ha revisado la derivación del operador de transición dipolar habitual para las transiciones radiativas del quarkonio, a partir del hamiltoniano de interacción en QED. Se han revisado brevemente las aproximaciones de longitud de onda larga y no relativista, así como sus condiciones de validez. Dado que estas condiciones pueden no cumplirse en algunas desintegraciones radiativas entre estados de quarkonio, se han deducido fórmulas más generales para el operador de transición electromagnético. Finalmente, se ha demostrado, a través de una breve revisión de las desintegraciones radiativas entre estados de charmonio, que los resultados obtenidos a partir de estas fórmulas generales son muy sensibles a los detalles de las funciones de onda del quarkonio y, por lo tanto, pueden servir, cuando se comparan con los datos experimentales, para testear diferentes modelos fenomenológicos.

3. Se han desarrollado modelos de creación de pares de quark-antiquark ligeros, para el estudio de las desintegraciones fuertes del quarkonio y del quarkonio híbrido a pares mesón-mesón de sabor abierto, respetando las simetrías de la aproximación BO. Se ha demostrado que los números cuánticos asociados a la configuración del medio hadrónico en la aproximación BO pueden utilizarse para determinar los números cuánticos del par creado. Específicamente, en el caso del quarkonio, el medio hadrónico se encuentra en su estado fundamental con números cuánticos similares a los del vacío, lo que corresponde al modelo habitual $^3P_0$ ampliamente utilizado en estudios fenomenológicos. En cuanto quarkonio híbrido de menor energía, cuyo medio hadrónico tiene los números cuánticos del estado fundamental del gluelump, el modelo de

creación de pares de quarks correspondiente tiene números cuánticos $^1P_1$. De esta manera, se ha revisado el modelo $^3P_0$ para el quarkonio y desarrollado el modelo $^1P_1$ para el quarkonio híbrido de menor energía.

4. Se ha utilizado la representación diabática, introducida por primera vez en la física molecular y atómica, para desarrollar un formalismo para la descripción de los mesones pesados formados por componentes quark-antiquark pesados y mesón-mesón de sabor abierto. Se ha mostrado que la dinámica está gobernada por una ecuación de Schrödinger multicanal que, particularizando a números cuánticos definidos J^{PC}, puede reducirse a una ecuación multicanal radial. Para la construcción de la matriz de potencial radial se han utilizado los resultados para energías estáticas calculadas con LQCD incluyendo gluones y quarks-antiquarks como campos ligeros ligeros. Estos resultados indican que el potencial radial asociado a la mezcla entre quark-antiquark pesados y mesón-mesón es significativo sólo para radios próximos a aquel para el cual el potencial del quarkonio coincide con la masa umbral del mesón-mesón.

5. Se ha examinado el espectro de estados ligados obtenidos con el formalismo diabático, con masas por debajo del umbral más bajo de mesón-mesón de sabor abierto. A continuación, se han discutido brevemente las dificultades en la resolución de la ecuación de Schrödinger diabática para energías por encima de dicho umbral, y se ha introducido una aproximación de estado ligado en la que el acoplamiento a umbrales abiertos se desprecia inicialmente. Se ha mostrado que la reintroducción del acoplamiento con los estados continuos de mesón-mesón transforma los estados ligados aproximados en resonancias de Fano, asociadas a mesones pesados que se desintegran a pares mesón-mesón de sabor abierto. Se ha obtenido un espectro de mesones pesados en los sectores del bottom y el charm y discutido las limitaciones de la aproximación de estados ligados utilizada.

6. Para superar las limitaciones de la aproximación de estados ligados se ha desarrollado un formalismo de dispersión no perturbativo para pares mesón-mesón de sabor abierto. Se ha demostrado que las soluciones de la ecuación diabática de Schrödinger para energías por encima del umbral se pueden interpretar de forma natural como estados estacionarios de dispersión. A continuación, se han conectado estas soluciones con la representación habitual de los estados de dispersión en términos de onda plana entrante más ondas esféricas salientes multiplicadas por la amplitud de dispersión. De este modo, se ha derivado un esquema no pertubativo para calcular la matriz de dispersión S sobre la capa másica

(*on-shell*) a partir de la matriz de potencial diabático. Finalmente, se ha hecho un análisis de las secciones eficaces elásticas mesón-mesón con sabor abierto y comparado con las resonancias de Fano previamente calculadas y con los datos experimentales. Este análisis indica que el espectro de mesones pesados consiste en un espectro de estados cuasiconvencionales (similares a estados del quarkonio) y otro de estados no convencionales, cuyas masas están próximas a algunos umbrales mesón-mesón. Cabe señalar que, en el caso de un estado no convencional con masa cercana por debajo de algún umbral, la sección eficaz en el canal correspondiente presenta un realce a bajos momentos que puede eclipsar a las resonancias cuasiconvencionales cercanas.

Desde un punto de vista fenomenológico, hay dos estados experimentales no convencionales que proporcionan casos de estudio ideales para, respectivamente, la aproximación BO y el formalismo diabático desarrollados en esta tesis. Por una parte, $\Upsilon(10860)$, cuya masa y propiedades de desintegración son compatibles con las de un estado mezcla de quarkonio y quarkonio híbrido, tal y como se ha propuesto a partir de un estudio dentro del marco de la aproximación de BO complementada con modelos consistentes de creación de pares de quark- antiquark ligeros. Por otra parte, $\chi_{c1}(3872)$, que puede interpretarse en el formalismo diabático como un estado $D^0\bar{D}^{*0}$ débilmente ligado con un núcleo $c\bar{c}$ compacto, tal como muestra un cálculo con un valor efectivo del parámetro de intensidad del potencial de mezcla.

Cabe señalar que el formalismo diabático es perfectamente general en el sentido de que también puede aplicarse para una descripción de sistemas de mesones pesados compuestos de quarkonio y de quarkonio híbrido, como $\Upsilon(10860)$. La limitación actual que impide esta aplicación es la falta de información a partir de LQCD acerca del potencial de mezcla en tales sistemas. Más aún, el formalismo diabático también es adecuado para el estudio de sistemas compuestos de quarkonio, quarkonio híbrido y mesón-mesón.

Por lo tanto, se puede concluir que un estudio completamente unificado de los mesones pesados de sabor oculto por debajo y por encima de los umbrales de sabor abierto es factible mediante el formalismo diabático. Es importante subrayar que la matriz de potencial diabático trata por igual los potenciales de los diferentes canales (quarkonio, mesón-mesón, quarkonio híbrido,...) así como los potenciales de mezcla entre ellos, de modo que las descripciones por debajo y por encima del umbral están conectadas de forma natural.

Appendices

Appendix A

Born-Oppenheimer Quantum Numbers

When spin degrees of freedom of the light fields are included, the stationary states of the light fields at some $Q\bar{Q}$ separation r are labeled, other than by their energy, by the conserved quantum numbers:

- λ: the projection of the total angular momentum of the light fields $\boldsymbol{J}_{\text{light}}$ on $\hat{\boldsymbol{r}}$, the $Q\bar{Q}$ separation direction;
- η: the parity of the state under CP transformations of the light fields;
- (only in the case $\lambda = 0$) ϵ: the parity of the state under reflection through a plane containing the $Q\bar{Q}$ pair.

It is also customary to introduce the shorthand $\Lambda = |\lambda|$. Notice that in general neither the other two orthogonal components of $\boldsymbol{J}_{\text{light}}$ nor J^2_{light} are conserved quantum numbers. This is a consequence of the static limit in which the light field states are calculated, which breaks the spherical symmetry down to a cylindrical symmetry around a line passing through $Q\bar{Q}$.

The BO potentials associated to each light field state are customarily labeled as $\Gamma^{(\epsilon)}_{\eta}$, where $\Gamma \equiv \Sigma, \Pi, \Delta, \ldots$ corresponds to $\Lambda = 0, 1, 2, \ldots$, the subscript $\eta = g, u$ corresponds to the quantum number $\eta = 1, -1$, and the superscript $\epsilon = \pm$ corresponds to the quantum number $\epsilon = \pm 1$ and is specified only in the case $\Gamma \equiv \Sigma$ (this is, $\Lambda = 0$).

So, for example, the ground state quenched potential, associated to the quarkonium potential, has quantum numbers $\lambda = 0$, $\eta = +1$, and $\epsilon = +1$, and is thus labeled Σ^+_g. Notice that the associated light field configuration has the same quantum numbers of the vacuum. The first excited quenched potential, associated to the lowest hybrid potential, has instead $\Lambda = 1$ and $\eta = -1$, and is labeled Π_u.

Beyond the static limit, the total angular momentum of the system $\boldsymbol{J}$ must be conserved, as a consequence of the spherical symmetry being restored with the reintroduction of the $Q\bar{Q}$ motion. It is given by the sum of $\boldsymbol{J}_{\text{light}}$ with the $Q\bar{Q}$ orbital angular momentum $\boldsymbol{L}$ and the total $Q\bar{Q}$ spin $\boldsymbol{S}$. It is more conveniently expressed as

$$\boldsymbol{J} = \boldsymbol{S} + \tilde{\boldsymbol{L}} \tag{A.1}$$

with the light field spin-orbit momentum defined as

$$\tilde{\boldsymbol{L}} = \boldsymbol{L} + \boldsymbol{J}_{\text{light}}.$$

In the infinite heavy quark mass limit, the spin of $Q\bar{Q}$ decouples from the system. In this limit, the total $Q\bar{Q}$ spin $\boldsymbol{S}$ becomes a conserved quantity and, by consequence of (A.1) and conservation of $\boldsymbol{J}$, so does $\tilde{\boldsymbol{L}}$. If the heavy quark mass is very big, even if not infinite, this so-called heavy-quark-spin symmetry may be a good approximation. Notice that the $Q\bar{Q}$ angular momentum $\boldsymbol{L}$ is not conserved in general, but only in the case $\boldsymbol{J}_{\text{light}} = 0$.

The derivation of the radial Schrödinger equation has been done elsewhere, see [53, 54] and references therein, and is reviewed here for the sake of completeness. In short, the adiabatic Schrödinger equation with the single channel approximation reads

$$\left[-\frac{1}{2\mu}\frac{\mathrm{d}^2}{\mathrm{d}r^2} + \frac{\langle L^2\rangle_{\Gamma,\boldsymbol{r}}}{2\mu r^2} + V(r)\right] r\psi(\boldsymbol{r}) = Er\psi(\boldsymbol{r}) \tag{A.2}$$

where the angular bracket $\langle \dots \rangle_{\Gamma,\boldsymbol{r}}$ stands for expectation value over the BO configuration Γ for $Q\bar{Q}$ relative position $\boldsymbol{r}$. Notice that this is equation differs from (1.9) in that in general $\langle L^2\rangle_{\Gamma,\boldsymbol{r}} \neq l(l+1)$. Instead, one has

$$\langle L^2\rangle_{\Gamma,\boldsymbol{r}} = \tilde{l}(\tilde{l}+1) - 2\Lambda^2 + \langle J^2_{\text{light}}\rangle_{\Gamma,\boldsymbol{r}}$$

where $\tilde{l}(\tilde{l}+1)$ is the eigenvalue of $\tilde{L}^2$. Since J^2_{light} is a scalar operator acting on the light fields only, the expectation value $\langle J^2_{\text{light}}\rangle_{\Gamma,\boldsymbol{r}}$ can be assumed to depend on the $Q\bar{Q}$ distance r only. Then, Equation (A.2) may be cast as a radial Schrödinger equation

$$\left[-\frac{1}{2\mu}\frac{\mathrm{d}^2}{\mathrm{d}r^2} + \frac{\tilde{l}(\tilde{l}+1) - 2\Lambda^2 + \langle J^2_{\text{light}}\rangle_{\Gamma,\boldsymbol{r}}}{2\mu r^2} + V_\Gamma(r)\right] u(r) = Eu(r). \tag{A.3}$$

Notice that, as a consequence of $\hat{\boldsymbol{r}} \cdot \boldsymbol{L} = 0$, one has $\hat{\boldsymbol{r}} \cdot \tilde{\boldsymbol{L}} = \hat{\boldsymbol{r}} \cdot \boldsymbol{J}_{\text{light}}$ and therefore $\tilde{l}$ has the lower bound $\tilde{l} \geq \Lambda$.

In general, the expectation value $\langle J^2_{\rm light}\rangle_{\Gamma,\boldsymbol{r}}$ might be some complicated function of the $Q\bar{Q}$ distance r, however, its value is only important for small r, where the centrifugal term is important. Then, one may approximate

$$\langle J^2_{\rm light}\rangle_{\Gamma,\boldsymbol{r}} \approx J_\Gamma(J_\Gamma+1)$$

with $J_\Gamma(J_\Gamma+1)$ the eigenvalue of $J^2_{\rm light}$ for the BO configuration Γ at small r (notice that $J^2_{\rm light}$ is conserved in the static limit with $r\to 0$), and (A.3) becomes

$$\left[-\frac{1}{2\mu}\frac{{\rm d}^2}{{\rm d}r^2}+\frac{\tilde{l}(\tilde{l}+1)-2\Lambda^2+J_\Gamma(J_\Gamma+1)}{2\mu r^2}+V_\Gamma(r)\right]u(r)=Eu(r).$$

To summarize, the effect of the spin-orbit momentum of the light fields may be included by modifying the centrifugal barrier term as

$$\frac{l(l+1)}{2\mu r^2}\to\frac{\tilde{l}(\tilde{l}+1)-2\Lambda^2+J_\Gamma(J_\Gamma+1)}{2\mu r^2}.$$

For the BO configuration Σ^+_g, one has $J_\Gamma=\Lambda=0$ and $\tilde{l}=l$, so that the centrifugal term is the same as in the spin-independent treatment of Section 1.1. For the lowest hybrid potential Π_u, one has $J_\Gamma=\Lambda=1$. Then, the centrifugal term becomes

$$\frac{\tilde{l}(\tilde{l}+1)}{2\mu r^2}.$$

with $\tilde{l}\geq 1$.

Appendix B

Effective Energy Gap

In this appendix, we briefly discuss the puzzling factor 3 difference between the phenomenological values of the energy gap, Equations (5.2) and (5.3), respectively, in the bottomoniumlike and charmoniumlike sectors. In Reference [82], this value of the ratio is explained by arguing the existence of a scaling law for Δ_Q on the heavy quark mass, which causes Δ_c/Δ_b to be approximately equal to m_b/m_c. This argument is reviewed here for the sake of completeness. Its incompatibility with lattice QCD calculations is briefly discussed, and an alternative explanation of the ratio is examined.

Let us analyze the relative importance of the various components of the radial potential matrix following an expansion in powers of $1/m_Q$. Equation (1.10) for the $Q\bar{Q}$ potential includes only terms up to order $1/m_Q$. It must be noted that, although we do not include them, spin-dependent and spin-independent terms up to order $1/m_Q^2$ have also been calculated [35, 52]. Concerning Equation (4.15), it can be expanded as

$$T_1 = 2m_Q + a + b/m_Q,$$

where a does not depend on m_Q and b may depend logarithmically on it [87]. Therefore, the threshold mass includes terms up to order $1/m_Q$.

As for the mixing potential (4.16), one should keep in mind that in the limit $m_Q \to \infty$ the single channel approximation should be recovered, and hence, the mixing potential should go to zero. This can be understood using the adiabatic-to-diabatic equivalence, and observing that in the adiabatic framework the NACTs breaking the single channel approximation are scaled by a factor $1/m_Q$, see Equation (1.7). The simplest way to incorporate this scaling in Equation (4.16) is to expand Δ in powers of m_Q as $\Delta \approx \alpha/m_Q + \mathcal{O}(1/m_Q^2)$, with α a constant with dimension of energy squared. One may further realize that the leading order coefficient α has the same dimensions of the string tension σ, and that the avoided crossing is possible only because the confining

interaction is in place (if σ were zero, the $Q\bar{Q}$ energy would never approach a meson-meson threshold). Then, α may be naturally expressed as the string tension σ times a dimensionless constant γ, so that

$$\Delta \simeq \frac{\sigma\gamma}{m_Q}$$

at leading order in $1/m_Q$. Then, plugging the values of m_b and Δ_b from Equations (1.12f) and (5.2), one obtains $\gamma = 1.03$.

The above argument provides a quite appealing explanation of the ratio Δ_b/Δ_c, especially so as $\gamma \approx 1$. However, this argument conflicts with the understanding of the lattice QCD energy levels being independent from the heavy quark mass m_Q apart from a constant shift to all levels.

Alternatively, the anomalous Δ_c/Δ_b ratio may have to do with a big degree of effectiveness in the value of Δ_c. Let us recall that Δ_c is fixed by requiring the appearance of a $D^0\bar{D}^{*0}$ state close to threshold, associated to $\chi_{c1}(3872)$. Let us also remind that in this study we have neglected any meson-meson interaction other than that mediated by string breaking. Then, if there were other meson-meson interactions playing a relevant role in the composition of $\chi_{c1}(3872)$, the effective energy gap Δ_c necessary to create the $D^0\bar{D}^{*0}$ state could be much greater than the lattice value, because it would have to compensate for the missing binding interactions.

In this case, the approximate phenomenological identities $\Delta_c/\Delta_b \approx m_b/m_c$ and $\Delta_Q m_Q \approx \sigma$ would be pure coincidences. Moreover, the good description of the width of $\psi(3770)$ would be quite surprising. In fact, such a big degree of effectiveness in Δ_c should result in anomalous values of the calculated widths to open-charm, since the same parameter is used for all mixing potentials which also mediate decays. Given that the decays to open-flavor are instead expected to occur mainly through string breaking, one could easily expect the widths calculated with an effective $\Delta_c \approx 3\Delta_{\text{Lattice}}$ to be around three times bigger than the physical ones. Instead, for the well-established $\psi(3770)$, the calculated total width to open-charm of 21.8 MeV is quite close to the measured total width of 27.2 ± 1.0 MeV.

Appendix C

Numerical Method

The numerical results presented in this thesis have been obtained using the *finite difference method*, adapted to the study of both bound and scattering states. In this appendix we review this numerical algorithm in a general setting.

Let us start by considering the simplest possible example, a single radial Schrödinger equation in the form

$$-\frac{1}{2\mu}u''(r)+\left(\frac{l(l+1)}{2\mu r^2}+V(r)-E\right)u(r)=0 \tag{C.1}$$

with $V(r)$ some general spherical potential, $u(r)$ the reduced wave function, μ the reduced mass, and l the orbital angular momentum.

In the finite difference method, one discretizes the continous coordinate r in a lattice of equally spaced points $r_{\rm n}={\rm n}d$ where d is the discretization step and ${\rm n}=0,1,\ldots,{\rm N}+1$, with N the total number of points in the interior of the lattice. The discretization procedure translates the Hamiltonian operator into a matrix, so that the differential Schrödinger equation is reduced to a linear system of equations whose solution yields the numerical reduced wave function $\{u_{\rm n}=u(r_{\rm n})\}_{\rm n=0}^{\rm N+1}$.

The discretization of the kinetic energy terms proceeds as follows. First, one approximates the second derivative as

$$u''_{\rm n}\approx\frac{u_{\rm n+1}-2u_{\rm n}+u_{\rm n-1}}{d^2} \tag{C.2}$$

which is accurate up to order $\mathcal{O}(d^2)$. This expression, however, cannot be applied at the origin and extreme of the lattice, r_0 and $r_{\rm N+1}$. For the wave function at these points it is thus necessary to impose Dirichlet boundary conditions $u_0=b^0$ and $u_{\rm N+1}=b^{\rm extr}$, respectively, with b^0 and $b^{\rm extr}$ some

complex parameters. Then, the second derivative at r_1 and at r_N reads

$$u_1'' \approx \frac{u_2 - 2u_1}{d^2} + \frac{b^0}{d^2},$$

and

$$u_N'' \approx \frac{u_{N-1} - 2u_N}{d^2} + \frac{b^{\text{extr}}}{d^2},$$

respectively, whereas at any other point in the lattice it is determined as in Equation (C.2). Then, the kinetic energy operator is discretized as

$$-\frac{1}{2\mu}u''(r) \to \mathrm{Ku} - \mathrm{b}$$

with K the tridiagonal kinetic energy matrix

$$\mathrm{K} = -\frac{1}{2\mu d^2}\begin{pmatrix} -2 & 1 & & & \\ 1 & -2 & 1 & & \\ & \ddots & \ddots & \ddots & \\ & & 1 & -2 & 1 \\ & & & 1 & -2 \end{pmatrix},$$

u the numerical reduced wave function without the boundary values

$$\mathrm{u} = \begin{pmatrix} u_1 \\ u_2 \\ \vdots \\ u_N \end{pmatrix}$$

and b a constant vector whose only nonzero components are the first and last one,

$$\mathrm{b} = \frac{1}{2\mu d^2}\begin{pmatrix} b^0 \\ \\ \\ b^{\text{extr}} \end{pmatrix},$$

corresponding to the boundary conditions.

Discretization of the centrifugal and potential energy terms in (C.1), on the other hand, is straightforward. It is customary to define an effective potential $V^{\text{eff}}(r)$ given by the sum of the radial potential and centrifugal barrier,

$$V^{\text{eff}}(r) = V(r) + \frac{l(l+1)}{2\mu r^2}.$$

whose discretization reads

$$V^{\text{eff}}(r)u(r) \to \mathrm{V}^{\text{eff}}\,\mathrm{u}$$

with V^{eff} the diagonal effective potential matrix

$$\mathrm{V}^{\text{eff}} = \begin{pmatrix} V^{\text{eff}}(r_1) & & & \\ & V^{\text{eff}}(r_2) & & \\ & & \ddots & \\ & & & V^{\text{eff}}(r_{\mathrm{N}}) \end{pmatrix}.$$

The discretized radial Schrödinger equation then reads

$$(\mathrm{H} - E)\mathrm{u} = \mathrm{b} \tag{C.3}$$

with H the Hamiltonian matrix

$$\mathrm{H} = \mathrm{K} + \mathrm{V}^{\text{eff}}.$$

The physical boundary conditions can be set requiring the numerical wave functions to follow the (known) asymptotic behavior of the analytical solutions.

If the potential $V(r)$ is regular or at most diverges as r^{-1} as r goes to zero, which is always the case for the diabatic potential studied in this thesis, then the analytical solution goes to zero as r^{l+1} for $r \to 0$. Hence, the corresponding physical boundary condition is $b^0 = 0$.

As for $r \to \infty$, there are different asymptotic behaviors depending on the position of the energy E with respect to the value of the potential $V(r)$ at infinity, $V^\infty = \lim_{r\to\infty} V(r)$. Specifically, let z and w be some constants, there are three possible cases:

- if $E < V^\infty$, then $u(r) \simeq ze^{-kr}$ with $k = \sqrt{2\mu(V^\infty - E)}$;
- if $E = V^\infty$, then $u(r) \simeq w$;
- if $E > V^\infty$, then $u(r) \simeq ze^{+ikr} + we^{-ikr}$ with $k = \sqrt{2\mu(E - V^\infty)}$.

The first case corresponds to $b^{\text{extr}} = 0$ as the physical boundary condition, whereas in the other two cases any finite value of b^{extr} yields a physical numerical wave function.

Therefore, if $E < V^\infty$, one has $\mathrm{b} = 0$ and Equation (C.3) reduces to an eigenvalue problem for the Hamiltonian matrix H. The solution of this numerical Schrödinger equation yields a discrete spectrum of bound states and the corresponding wave functions.

If otherwise $E \geq V^{\infty}$, then there is no criterion to fix a specific value of the boundary condition at the extreme, since the analytical solution either is a constant ($E = V^{\infty}$) or keeps oscillating indefinitely ($E > V^{\infty}$). However, the energy spectrum in this case is known *a priori*, this is, the continuum spectrum. Furthermore, one may exploit the fact that, having fixated one of the two boundary conditions, $b^0 = 0$, there is only one linearly independent solution for each energy E in the continuum. Then, it is sufficient to solve the nonhomogeneous linear Equation (C.3) with an arbitrary nonzero boundary condition, $b^{\text{extr}} \neq 0$, and any other possible solution can be obtained from multiplication by a global factor.[1]

The discretization procedure outlined above for a single Schrödinger equation can easily applied to a multichannel one such as the diabatic Schrödinger equation. In a problem with $\bar{N}$ channels, the same Equation (C.3) applies, but with some formal substitutions. Namely, the kinetic energy matrix becomes

$$\mathrm{K} = -\frac{1}{2d^2}\begin{pmatrix} -2\mu^{-1} & \mu^{-1} & & & \\ \mu^{-1} & -2\mu^{-1} & \mu^{-1} & & \\ & \ddots & \ddots & \ddots & \\ & & \mu^{-1} & -2\mu^{-1} & \mu^{-1} \\ & & & \mu^{-1} & -2\mu^{-1} \end{pmatrix},$$

with μ the diagonal reduced mass matrix

$$\mu = \begin{pmatrix} \mu_1 & & & \\ & \mu_2 & & \\ & & \ddots & \\ & & & \mu_{\bar{N}} \end{pmatrix}$$

and the effective potential matrix V^{eff} becomes

$$\begin{pmatrix} \mathrm{V}^{\text{eff}}(r_1) & & & \\ & \mathrm{V}^{\text{eff}}(r_2) & & \\ & & \ddots & \\ & & & \mathrm{V}^{\text{eff}}(r_{\mathrm{N}}) \end{pmatrix}$$

[1] Notice that this procedure fails if there is a nonzero solution compatible with the boundary condition $b^{\text{extr}} = 0$. This, however, happens only for a discrete subset of energies in the continuum, this is, the energy levels of a particle in a spherical well, which are not numerically accessible in general.

with

$$\mathrm{V}^{\mathrm{eff}}(r) = \mathrm{V}(r) + \frac{1}{r^2} \begin{pmatrix} \frac{l_1(l_1+1)}{2\mu_1} & & & \\ & \frac{l_2(l_2+1)}{2\mu_2} & & \\ & & \ddots & \\ & & & \frac{l_{\bar{N}}(l_{\bar{N}}+1)}{2\mu_{\bar{N}}} \end{pmatrix}$$

where $\mathrm{V}(r)$ is the multichannel potential matrix. Notice that we have allowed the different channels to have different values of the reduced mass and orbital angular momentum.

The numerical wave function becomes

$$\mathrm{u} = \begin{pmatrix} \mathrm{u}_1 \\ \mathrm{u}_2 \\ \vdots \\ \mathrm{u}_{\mathrm{N}} \end{pmatrix}$$

with

$$\mathrm{u}_{\mathrm{n}} = \begin{pmatrix} u_1(r_{\mathrm{n}}) \\ u_2(r_{\mathrm{n}}) \\ \vdots \\ u_{\bar{N}}(r_{\mathrm{n}}) \end{pmatrix}$$

the multichannel wave function at the lattice node r_{n}, and the constant vector becomes

$$\mathrm{b} = \frac{1}{2\mu d^2} \begin{pmatrix} \\ \\ \mathrm{b}^{\mathrm{extr}} \end{pmatrix},$$

where we have already assumed $\mathrm{b}_0 = 0$ and in general

$$\mathrm{b}^{\mathrm{extr}} = \begin{pmatrix} b_1^{\mathrm{extr}} \\ b_2^{\mathrm{extr}} \\ \vdots \\ b_{\bar{N}}^{\mathrm{extr}} \end{pmatrix}.$$

Notice that the boundary condition at the extreme has become a vector. The components of this vector, one for each channel, have different values depending on whether the associated channel is open or not. To be more precise, let us assume that in the limit $r \to \infty$ the potential matrix becomes

diagonal,

$$\mathrm{V}(r) \simeq \begin{pmatrix} V_1^\infty & & & \\ & V_2^\infty & & \\ & & \ddots & \\ & & & V_{\bar{N}}^\infty \end{pmatrix},$$

such as in the case of the diabatic potential matrix studied here. Then, for each channel i with $i = 1, 2, \ldots, \bar{N}$, the physical boundary conditions at the extreme are:

- $b_i^{\mathrm{extr}} = 0$, if $E < V_i^\infty$;
- b_i^{extr} arbitrary, if $E \geq V_i^\infty$.

The multichannel Equation (C.3) for an energy E can be solved by realizing that there are as many linearly independent solutions as there are unfixed boundary conditions. Then, it may be useful to think of the b_i^{extr} for the open channels $\{i \mid V_i^\infty \leq E\}$ as components of a numerical vector $\mathrm{b}_{\mathrm{open}}^{\mathrm{extr}} \in \mathbb{C}^{\bar{n}}$, with $\bar{n}$ the total number of open channels at the energy E. So, there is a $1:1$ correspondence between numerical boundary condition vectors $\mathrm{b}_{\mathrm{open}}^{\mathrm{extr}}$ and numerical solutions of the Schrödinger equation above threshold, and therefore a complete set of linearly independent solutions at energy E can be obtained by solving Equation (C.3) for a complete set of linearly independent $\mathrm{b}_{\mathrm{open}}^{\mathrm{extr}}$.

Let us note here that the results presented in this thesis have been obtained using a Python implementation of the algorithm described above. More specifically, the nonhomogeneous linear system (C.3) has been solved using the NumPy [88] and SciPy [89] libraries. In case of solutions above threshold, we have used the canonical basis of $\mathbb{C}^{\bar{n}}$ as the complete set of linearly independent $\mathrm{b}_{\mathrm{open}}^{\mathrm{extr}}$. As for the hyperparameters of the discretization scheme, we have used $d = 10^{-3}$ fm and $r^{\mathrm{extr}} = 200$ fm.

Acronyms

ADT adiabatic-to-diabatic transition

BO Born-Oppenheimer

BS Bethe-Salpeter

EFT effective field theory

EM electromagnetic

LWL long wavelength

NACT non-adiabatic coupling term

NR nonrelativistic

OZI Okubo-Zweig-Izuka

PDG Particle Data Group

QCD quantum chromodynamics

QED quantum electrodynamics

QPC quark pair creation

Bibliography

[1] H. Fritzsch, M. Gell-Mann, and H. Leutwyler, Advantages of the Color Octet Gluon Picture, Phys. Lett. B **47**, 365 (1973).

[2] D. J. Gross and F. Wilczek, Ultraviolet Behavior of Nonabelian Gauge Theories, Phys. Rev. Lett. **30**, 1343 (1973).

[3] H. D. Politzer, Reliable Perturbative Results for Strong Interactions?, Phys. Rev. Lett. **30**, 1346 (1973).

[4] N. Isgur and M. B. Wise, Spectroscopy with heavy-quark symmetry, Phys. Rev. Lett. **66**, 1130 (1991).

[5] E. Seiler, *Gauge Theories as a Problem of Constructive Quantum Field Theory and Statistical Mechanics*, Vol. 159 (Springer Verlag, Berlin, Heidelberg, New York, 1982).

[6] M. Creutz, *Quarks, Gluons and Lattices* (Cambridge University Press, Cambridge, 1985).

[7] C. Rebbi, ed., *Lattice Gauge Theories and Monte Carlo Simulations* (World Scientific Singapore, Singapore, 1984).

[8] C. Itzykson and J. M. Drouffe, *Statistical Field Theory. Vol. 1: From Brownian Motion to Renormalization and Lattice Gauge Theory* (Cambridge University Press, Cambridge, 1989).

[9] M. Creutz, ed., *Quantum Fields on the Computer* (World Scientific Singapore, Singapore, 1992).

[10] H. J. Rothe, *Lattice Gauge Theories: An Introduction*, Vol. 43 (World Scientific Singapore, Singapore, 1992).

[11] I. Montvay and G. Munster, *Quantum Fields on a Lattice* (Cambridge University Press, Cambridge, 1997).

[12] J. Smit, *Introduction to Quantum Fields on a Lattice: A Robust Mate* (Cambridge University Press, Cambridge, 2011).

[13] R. Gupta, Introduction to lattice QCD: Course, in *Proceedings, Les Houches Summer School in Theoretical Physics, Session 68: Probing the Standard Model of Particle Interactions* (1997), arXiv:hep-lat/9807028.

[14] C. McNeile, Heavy quarks on the lattice, Lect. Notes Phys. **647**, 100 (2004), arXiv:hep-lat/0210026; Meson and baryon spectroscopy on a lattice, Int. Rev. Nucl. Phys. **9**, 1 (2004), arXiv:hep-lat/0307027.

[15] G. S. Bali, H. Neff, T. Düssel, T. Lippert, and K. Schilling (SESAM Collaboration), Observation of string breaking in QCD, Phys. Rev. D **71**, 114513 (2005), arXiv:hep-lat/0505012.

[16] C. Davies, Lattice QCD 2007, in *Proceedings, 23rd International Symposium on Lepton-Photon Interactions at High Energy (LP07)* (2008), arXiv:0807.1402 [hep-ph].

[17] J. Bulava, B. Hörz, F. Knechtli, V. Koch, G. Moir, C. Morningstar, and M. Peardon, String breaking by light and strange quarks in QCD, Phys. Lett. B **793**, 493 (2019), arXiv:1902.04006 [hep-lat].

[18] M. Luscher, Advanced lattice QCD, in *Proceedings, Les Houches Summer School in Theoretical Physics, Session 68: Probing the Standard Model of Particle Interactions* (1998), arXiv:hep-lat/9802029; Lattice QCD: From quark confinement to asymptotic freedom, Annales Henri Poincare **4**, S197 (2003), arXiv:hep-ph/0211220.

[19] M. Di Pierro, From Monte Carlo integration to lattice quantum chromodynamics: An Introduction, in *Proceedings, GSA Summer School on Physics on the Frontier and in the Future* (2000), arXiv:hep-lat/0009001.

[20] G. Munster and M. Walzl, Lattice gauge theory: A Short primer, in *Proceedings, Zuoz Summer School on Phenomenology of Gauge Interactions* (2000), arXiv:hep-lat/0012005.

[21] R. Kenway, Lattice field theory, in *Proceedings, 30th International Conference on High-Energy Physics* (2000), arXiv:hep-ph/0010219; The Status of Lattice QCD, in *Proceedings, International School of Subnuclear Physics (ISSP 2006): 44th Course: Homage to Richard H. Dalitz: The Logic of Nature, Complexity and New Physics: From Quark-Gluon Plasma to Superstrings, Quantum Gravity and Beyond*, Subnucl. Ser. **44**, 137 (2008).

[22] G. S. Bali, QCD forces and heavy quark bound states, Phys. Rep. **343**, 1 (2001), arXiv:hep-ph/0001312.

[23] M. Creutz, Aspects of Chiral Symmetry and the Lattice, Rev. Mod. Phys. **73**, 119 (2001), arXiv:hep-lat/0007032; The Early days of lattice gauge theory, in *Proceedings, Monte Carlo method in the Physical Sciences: Celebrating the 50th Anniversary of the Metropolis Algorithm*, AIP Conf. Proc. **90**, 52 (2003), arXiv:hep-lat/0306024.

[24] A. S. Kronfeld, Uses of Effective Field Theory in Lattice QCD, in *At the Frontiers of Particle Physics, Handbook of QCD*, edited by N. Shifman (2002) Chapter 39, arXiv:hep-lat/0205021.

[25] T. A. DeGrand, Lattice QCD at the end of 2003, Int. J. Mod. Phys. A **19**, 1337 (2004), arXiv:hep-ph/0312241.

[26] S. Weinberg, Phenomenological Lagrangians, Physica A: Statistical Mechanics and its Applications **96**, 327 (1979).

[27] W. E. Caswell and G. P. Lepage, Effective Lagrangians for Bound State Problems in QED, QCD, and Other Field Theories, Phys. Lett. B **167**, 437 (1986).

[28] N. Brambilla, H. S. Chung, and A. Vairo, Inclusive production of heavy quarkonia in pNRQCD, JHEP **09**, 032 (2021), arXiv:2106.09417 [hep-ph].

[29] B. A. Thacker and G. P. Lepage, Heavy quark bound states in lattice QCD, Phys. Rev. D **43**, 196 (1991).

[30] G. T. Bodwin, E. Braaten, and G. P. Lepage, Rigorous QCD analysis of inclusive annihilation and production of heavy quarkonium, Phys. Rev. D **51**, 1125 (1995), arXiv:hep-ph/9407339; [Erratum: Phys. Rev. D **55**, 5853 (1997)].

[31] A. Pineda and J. Soto, Effective field theory for ultrasoft momenta in NRQCD and NRQED, in *Proceedings, High-Energy Physics International Euroconference on Quantum Chromodynamics (QCD 97): 25th Anniversary of QCD*, Nucl. Phys. B Proc. Suppl. **64**, 428 (1998), arXiv:hep-ph/9707481.

[32] N. Brambilla, A. Pineda, J. Soto, and A. Vairo, Potential NRQCD: An Effective theory for heavy quarkonium, Nucl. Phys. B **566**, 275 (2000), arXiv:hep-ph/9907240; The QCD potential at O(1/m), Phys. Rev. D **63**, 014023 (2001), arXiv:hep-ph/0002250.

[33] M. E. Luke, A. V. Manohar, and I. Z. Rothstein, Renormalization group scaling in nonrelativistic QCD, Phys. Rev. D **61**, 074025 (2000), arXiv:hep-ph/9910209.

[34] A. V. Manohar and I. W. Stewart, Renormalization group analysis of the QCD quark potential to order v^2, Phys. Rev. D **62**, 014033 (2000), arXiv:hep-ph/9912226.

[35] A. Pineda and A. Vairo, The QCD potential at O($1/m^2$): Complete spin dependent and spin independent result, Phys. Rev. D **63**, 054007 (2001), arXiv:hep-ph/0009145; [Erratum: Phys. Rev. D **64**, 039902 (2001)].

[36] A. H. Hoang and I. W. Stewart, Ultrasoft renormalization in nonrelativistic QCD, Phys. Rev. D **67**, 114020 (2003), arXiv:hep-ph/0209340.

[37] M. T. AlFiky, F. Gabbiani, and A. A. Petrov, X(3872): Hadronic molecules in effective field theory, Phys. Lett. B **640**, 238 (2006), arXiv:hep-ph/0506141.

[38] A. Hosaka, T. Iijima, K. Miyabayashi, Y. Sakai, and S. Yasui, Exotic hadrons with heavy flavors: X, Y, Z, and related states, Prog. Theor. Exp. Phys. **2016**, 062C01 (2016).

[39] Y. Dong, A. Faessler, and V. E. Lyubovitskij, Description of heavy exotic resonances as molecular states using phenomenological Lagrangians, Prog. Part. Nucl. Phys. **94**, 282 (2017).

[40] F.-K. Guo, C. Hanhart, U.-G. MeiSSner, Q. Wang, Q. Zhao, and B.-S. Zou, Hadronic molecules, Rev. Mod. Phys. **90**, 015004 (2018), arXiv:1705.00141 [hep-ph].

[41] J.-X. Lu, L.-S. Geng, and M. P. Valderrama, Heavy baryon-antibaryon molecules in effective field theory, Phys. Rev. D **99**, 074026 (2019), arXiv:1706.02588 [hep-ph].

[42] M. P. Valderrama, Heavy hadron molecules in effective field theory: the emergence of exotic nuclear landscapes, Eur. Phys. J. A **56**, 109 (2020), arXiv:1906.06491 [hep-ph].

[43] M. A. Shifman, A. I. Vainshtein, and V. I. Zakharov, QCD and Resonance Physics: Applications, Nucl. Phys. B **147**, 448 (1979).

[44] L. J. Reinders, H. Rubinstein, and S. Yazaki, Hadron Properties from QCD Sum Rules, Phys. Rept. **127**, 1 (1985).

[45] S. Narison, *QCD as a Theory of Hadrons: From Partons to Confinement*, Vol. 17 (Cambridge University Press, Cambridge, 2007), arXiv:hep-ph/0205006; Mini-review on QCD spectral sum rules, in *Proceedings, 17th International Conference on Quantum Chromodynamics (QCD14)*, Nucl. Part. Phys. Proc. **258**, 189 (2015), arXiv:1409.8148 [hep-ph]; Modern status of heavy quark sum rules in QCD, in *Proceedings, 23rd High-Energy Physics International Conference in Quantum Chromodynamics*

(QCD20), Nucl. Part. Phys. Proc. **312**, 15281 (2021), arXiv:2101.12579 [hep-ph].

[46] E. E. Salpeter and H. A. Bethe, A Relativistic equation for bound state problems, Phys. Rev. **84**, 1232 (1951).

[47] C. D. Roberts and A. G. Williams, Dyson-Schwinger equations and their application to hadronic physics, Prog. Part. Nucl. Phys. **33**, 477 (1994), arXiv:1601.04024 [hep-ph].

[48] E. Eichten, K. Gottfried, T. Kinoshita, K. D. Lane, and T.-M. Yan, Charmonium: The model, Phys. Rev. D **17**, 3090 (1978); [Erratum: Phys. Rev. D **21**, 313 (1980)].

[49] S. Godfrey and N. Isgur, Mesons in a relativized quark model with chromodynamics, Phys. Rev. D **32**, 189 (1985).

[50] W. Lucha, F. F. Schoberl, and D. Gromes, Bound states of quarks, Phys. Rept. **200**, 127 (1991).

[51] K. G. Wilson, Confinement of quarks, Phys. Rev. D **10**, 2445 (1974).

[52] E. Eichten and F. Feinberg, Spin-dependent forces in quantum chromodynamics, Phys. Rev. D **23**, 2724 (1981).

[53] K. J. Juge, J. Kuti, and C. J. Morningstar, Ab Initio Study of Hybrid $\bar{b}gb$ Mesons, Phys. Rev. Lett. **82**, 4400 (1999), arXiv:hep-ph/9902336.

[54] E. Braaten, C. Langmack, and D. H. Smith, Born-Oppenheimer approximation for the XYZ mesons, Phys. Rev. D **90**, 014044 (2014), arXiv:1402.0438 [hep-ph].

[55] R. Bruschini and P. González, Radiative decays in bottomonium beyond the long wavelength approximation, Phys. Rev. D **100**, 074001 (2019), arXiv:1906.09055 [hep-ph].

[56] R. Bruschini and P. González, Radiative decays in charmonium beyond the p/m approximation, Phys. Rev. D **101**, 014027 (2020), arXiv:1910.06773 [hep-ph].

[57] R. Bruschini and P. González, A plausible explanation of $\Upsilon(10860)$, Phys. Lett. B **791**, 409 (2019), arXiv:1811.08236 [hep-ph].

[58] R. Bruschini and P. González, Strong decays of the lowest bottomonium hybrid within an extended Born-Oppenheimer framework, Eur. Phys. J. C **81**, 74 (2021), arXiv:1912.07337 [hep-ph].

[59] R. Bruschini and P. González, Diabatic description of charmoniumlike mesons, Phys. Rev. D **102**, 074002 (2020), arXiv:2007.07693 [hep-ph].

[60] R. Bruschini and P. González, Diabatic description of charmoniumlike mesons. II. Mass corrections and strong decay widths, Phys. Rev. D **103**, 074009 (2021), arXiv:2101.04636 [hep-ph].

[61] R. Bruschini and P. González, Diabatic description of bottomoniumlike mesons, Phys. Rev. D **103**, 114016 (2021), arXiv:2105.04401 [hep-ph].

[62] R. Bruschini and P. González, Coupled-channel meson-meson scattering in the diabatic framework, Phys. Rev. D **104**, 074025 (2021), arXiv:2107.05459 [hep-ph].

[63] M. Born and R. Oppenheimer, Zur quantentheorie der molekeln, Ann. Phys. (Berlin) **389**, 457 (1927).

[64] N. Brambilla, G. Krein, J. Tarrús Castellà, and A. Vairo, Born-Oppenheimer approximation in an effective field theory language, Phys. Rev. D **97**, 016016 (2018), arXiv:1707.09647 [hep-ph].

[65] M. Baer, *Beyond Born-Oppenheimer: Electronic Nonadiabatic Coupling Terms and Conical Intersections* (John Wiley & Sons, New York, 2006).

[66] E. J. Eichten and C. Quigg, Mesons with beauty and charm: Spectroscopy, Phys. Rev. D **49**, 5845 (1994), arXiv:1902.09735 [hep-ph].

[67] K. J. Juge, J. Kuti, and C. J. Morningstar, Fine Structure of the QCD String Spectrum, Phys. Rev. Lett. **90**, 161601 (2003), arXiv:hep-lat/0207004.

[68] N. Isgur and J. E. Paton, A Flux Tube Model for Hadrons in QCD, Phys. Rev. D **31**, 2910 (1985).

[69] R. C. Giles and S.-H. H. Tye, Application of the quark-confining string to the ψ spectroscopy, Phys. Rev. D **16**, 1079 (1977).

[70] P. A. Zyla et al. (Particle Data Group), Review of particle physics, Prog. Theor. Exp. Phys. **2020**, 083C01 (2020).

[71] N. Brambilla, W. K. Lai, J. Segovia, J. Tarrús Castellà, and A. Vairo, Spin structure of heavy-quark hybrids, Phys. Rev. D **99**, 014017 (2019), arXiv:1805.07713 [hep-ph]; [Erratum: Phys. Rev. D **101**, 099902 (2020)].

[72] N. Brambilla, W. K. Lai, J. Segovia, and J. Tarrús Castellà, QCD spin effects in the heavy hybrid potentials and spectra, Phys. Rev. D **101**, 054040 (2020), arXiv:1908.11699 [hep-ph].

[73] E. J. Eichten, S. Godfrey, H. Mahlke, and J. L. Rosner, Quarkonia and their transitions, Rev. Mod. Phys. **80**, 1161 (2008), arXiv:hep-ph/0701208 [hep-ph].

[74] A. LeYaouanc, L. Oliver, O. Pene, and J. C. Raynal, *Hadron Transitions in the Quark Model* (Gordon and Breach Science Publishers, New York, 1988).

[75] C. Meyer and E. Swanson, Hybrid mesons, Prog. Part. Nucl. Phys. **82**, 21 (2015), arXiv:1502.07276 [hep-ph].

[76] C. Farina, H. G. Tecocoatzi, A. Giachino, E. Santopinto, and E. S. Swanson, Heavy hybrid decays in a constituent gluon model, Phys. Rev. D **102**, 014023 (2020), arXiv:2005.10850 [hep-ph].

[77] S.-K. Choi et al. (Belle Collaboration), Observation of a Narrow Charmoniumlike State in Exclusive $B^{\pm} \to K^{\pm}\pi^{+}\pi^{-}J/\psi$ Decays, Phys. Rev. Lett. **91**, 262001 (2003).

[78] P. del Amo Sanchez et al. (BaBar), Evidence for the decay $X(3872) \to J/\psi\omega$, Phys. Rev. D **82**, 011101 (2010), arXiv:1005.5190 [hep-ex].

[79] M. Ablikim et al. (BESIII Collaboration), Study of $e^{+}e^{-} \to \gamma\,\omega\,J/\psi$ and Observation of $X(3872) \to \omega\,J/\psi$, Phys. Rev. Lett. **122**, 232002 (2019).

[80] N. Brambilla, S. Eidelman, C. Hanhart, A. Nefediev, C.-P. Shen, C. E. Thomas, A. Vairo, and C.-Z. Yuan, The XYZ states: experimental and theoretical status and perspectives, Phys. Rep. **873**, 1 (2020).

[81] E. S. Swanson, The New heavy mesons: A Status report, Phys. Rept. **429**, 243 (2006), arXiv:hep-ph/0601110.

[82] R. Bruschini and P. González, Is $\chi_{c1}(3872)$ generated from string breaking?, Phys. Rev. D **105**, 054028 (2022), arXiv:2111.07653 [hep-ph].

[83] U. Fano, Effects of Configuration Interaction on Intensities and Phase Shifts, Phys. Rev. **124**, 1866 (1961).

[84] J. R. Taylor, *Scattering Theory: The Quantum Theory on Nonrelativistic Collisions* (John Wiley & Sons, New York, 1972).

[85] N. F. Mott and H. S. W. Massey, *The Theory of Atomic Collisions* (Clarendon Press, Oxford, 1933) Chapter X.

[86] R. G. Newton, *Scattering Theory of Waves and Particles* (Springer, New York, 1982).

[87] N. Brambilla, J. Komijani, A. S. Kronfeld, and A. Vairo (TUMQCD Collaboration), Relations between heavy-light meson and quark masses, Phys. Rev. D **97**, 034503 (2018), arXiv:1712.04983 [hep-ph].

[88] C. R. Harris et al., Array programming with NumPy, Nature **585**, 357 (2020).

[89] P. Virtanen et al., SciPy 1.0: Fundamental Algorithms for Scientific Computing in Python, Nature Methods **17**, 261 (2020).

Index